Title
Development and Applications of a Carbon-Weather Data Assimilation System

Author
Wuerth, Stephanie

Publication Date
2019

Peer reviewed|Thesis/dissertation

Development and Applications of a Carbon-Weather Data Assimilation System

By

Stephanie M. Wuerth

A dissertation submitted in partial satisfaction of the

requirements for the degree of

Doctor of Philosophy

in

Earth and Planetary Science

and the Designated Emphasis

in

Computational and Data Science and Engineering

in the

Graduate Division

of the

University of California, Berkeley

Committee in charge:

Professor Inez Y. Fung, Chair
Professor Ronald Cohen
Professor John Chiang
Dr. Jeffrey Anderson

Spring 2019

Development and Applications of a Carbon-Weather Data Assimilation System

Abstract

Development and Applications of a Carbon-Weather Data Assimilation System

by

Stephanie M. Wuerth

Doctor of Philosophy in Earth and Planetary Science

Designated Emphasis in Computational and Data Science and Engineering

University of California, Berkeley

Professor Inez Y. Fung, Chair

This dissertation explores the utility of high-resolution satellite carbon dioxide (CO_2) and water vapor measurements for advancing climate treaty verification, for improving numerical weather prediction (NWP), and for understanding natural carbon cycling in the terrestrial biosphere. We present a series of Observing System Simulation Experiments (OSSEs) using a carbon-weather data assimilation (DA) system, where the state vector comprises weather variables (wind, temperature, humidity and pressure) and atmospheric CO_2 mixing ratios. The system seeks the optimal fit between a suite of synthetic meteorological and satellite-based total column CO_2 (XCO_2) observations with forecasts from a global Earth system model. Given the incomplete observations and imperfect model, the simultaneous assimilation of weather and CO_2 observations into our system yields the best approximation of atmospheric transport as well as its uncertainty, something not captured by other community carbon data assimilation and surface flux inversion systems which use a single realization of atmospheric transport. Our assimilation window is six hours, meaning that we have a time-evolving estimate of the atmospheric state, and its uncertainty (represented by the spread in the ensemble) at the resolution of six hours.

In Chapter 2, we employ this machinery to assess the capability of our carbon-weather DA system, along with satellite-borne XCO_2 observations, to detect underreporting of CO_2 emissions at the scale of a large country. In a series of OSSEs, we assimilate synthetic observations of XCO_2 at the locations of (1) the Orbiting Carbon Observatory 2 (OCO-2) soundings and (2) a hypothetical observing system which observes globally at 1pm local time. Fossil fuel CO_2 emissions are modified to have a -50% bias over China, but the observations are pulled from a model run where this bias is not present. We test whether the data assimilation system can detect the imposed bias by examining the near-surface innovation in CO_2 mass in a method similar to the mass-balance inversion. We find that with the hypothetical observation strategy, we can recover half of the imposed bias, and

that the ensemble mean of the near-surface CO_2 tracks the truth during the daytime, but underestimates the truth during the unconstrained nighttime hours over the region of the imposed bias. For the OCO-2 strategy, we detect a signal at the location of the imposed bias that is obscured by problems such as observation coverage. We discuss potential additions to the observing system which could optimize the detection of biased emissions with our data assimilation machinery.

Chapter 3 presents results from OSSEs aimed at understanding the potential of OCO-2 total precipitable water (TPW) and XCO_2 to improve weather forecasting capabilities. The hypothesis is that the time- and space-varying correlation between the satellite observable and wind in the Earth System Model could be used to improve the weather forecast where wind observations are sparse. We find that the TPW observations impact all meteorological state variables in the experiment, and that the XCO_2 observations reduce weather forecast errors globally, and most significantly in the southern extratropics, in all meteorological fields except humidity. We conclude that both of these observation types from OCO-2 could serve as useful additions to the suite of observations assimilated by national weather forecasting centers.

In Chapter 4, we calculate global CO_2 surface fluxes as a residual in the vertically-integrated CO_2 tracer transport equation, using time-varying 3D-CO_2 and meteorology reanalysis fields from a carbon-weather DA system that assimilates weather and XCO_2 from the Atmospheric Infrared Sounder (AIRS). As AIRS XCO_2 is weighted in the mid-troposphere, we find that the most significant impact on the surface flux calculation is in the tropics, especially over the Amazon and in the tropical Pacific, where intense convection mixes CO_2 through the entire tropospheric column. We compare our posterior flux estimates to those made by CarbonTracker and find general sign agreement except in the Amazon region. Here we estimate a net annual sink of -0.26 PgC whereas CarbonTracker, which uses only surface observations, estimates a net annual source of about the same magnitude.

For my parents.

Contents

List of Figures

List of Tables

Acknowledgments

I express my deepest appreciation to Inez for guiding me through this arduous but rewarding journey, and my other committee members, Jeff, John, and Ron, for their constructive comments.

This work would not have been possible without the assistance of the DART team at NCAR (Kevin Raeder, Nancy Collins, Tim Hoar, and Jeff), who patiently taught me the ins and outs of the DART and CESM source code on my numerous visits to Boulder. Jérôme Barré was also of crucial help in providing his code for creating pseudorandom fields, which was used to create fossil fuel emission ensembles for Chapter 2.

I am also grateful to all of the OCO-2 Science Team members for inspiring me and enriching my graduate education with the research they presented at our numerous telecons and team meetings over the years. In particular, I owe special thanks to Junjie Liu for her helpful feedback on my work, and for providing her assimilation output which I analyze in Chapter 4 of this dissertation, and to David Baker for providing the aggregated OCO-2 dataset which I use in Chapter 2.

Many thanks to the graduate students and postdoctoral scholars who have shared 301 McCone Hall with me (Percy Link, Holly Maness, Ju-Mee Ryoo, Mark Yashar, Jesse Day, Octavia Crompton, Eren Bilir, Jiabin Liu, Alex Turner, and Hannah Bourne), for providing me with motivation, guidance, conversation, snacks, and the occasional corgi puppy.

Special thanks are owed to my running companions (Jake Edman, Clara Eng, Noah Randolph-Flagg, Jake Seeley, William Hawley, Chelsea Willett, and Justine Chia), for escaping with me into the forest for some much-needed non-screen time throughout the years.

Lastly, I thank my husband, Michael, my family and his, for their unwavering support over the years.

Chapter 1

Introduction

Carbon cycles naturally through several terrestrial reservoirs. On geologic time scales, airborne carbon dioxide (CO_2) becomes part of the chemical weathering cycle: it dissolves in rain water to form carbonic acid, erodes newly-formed mountains, is transported by rivers and deposited as limestone on the sea floor. On shorter timescales, it can be taken up by plants in the terrestrial biosphere as they photosynthesize, and emitted back to the atmosphere as heterotrophs metabolize organic material, or it can be exchanged with the ocean via both physical and biological processes.

Human activity has perturbed this natural carbon cycling, increasing the pre-industrial concentration of atmospheric CO_2 from $\sim$277 parts per million (ppm) (Joos and Spahni 2008) in 1750 to 405.0 ± 0.1 ppm in 2017 (Le Quéré et al. 2018). Until 1950, the increase was predominantly from land use change activity such as deforestation, but since then it has been dominated by fossil fuel emission (Stocker et al. 2013).

This increase in CO_2 in Earth's atmosphere from human activity has been observed continuously at the Mauna Loa Observatory (Keeling et al. 1976b) and the South Pole Observatory (Keeling et al. 1976a) since the late 1950s. Starting around the same time, measurements of the partial pressure of CO_2 at the ocean surface have been recorded (Takahashi et al. 1997). In 1967, collection of air samples from land and aboard ships began, for offsite processing to determine the CO_2 concentration at the sites (Tans and Conway 2005). In 1992, a network of tall towers, which observe CO_2 at three tropospheric heights, were added to the observation system (Bakwin et al. 1995).

The aforementioned components of the CO_2 observation network do not offer a comprehensive picture of the vertical or meridional distribution of CO_2 in the global atmosphere, but aircraft campaigns have been carried out to elucidate the structure of CO_2 abundance in these dimensions. For example, the HIAPER Pole-to-Pole Observation (HIPPO) program provides aircraft-based vertical profiles of CO_2 along transects from near the north pole to 67°S (Wofsy 2011). HIPPO observations provide detailed three-dimensional pictures of CO_2 in the global atmosphere for specific time periods in certain seasons. They can be used to validate transport models and satellite data for the particular time periods of the campaigns, but they do not provide continuous observation of atmospheric CO_2.

In the past ∼15 years, global observations of atmospheric CO_2 have become available from satellite-borne instruments. These space-based instruments measure radiances emitted from Earth (either thermal emission or solar backscatter) and derive either partial column or total column CO_2 abundances (i.e., XCO_2) from these radiances. Instruments measuring thermal emission include the Atmospheric Infrared Sounder (AIRS, Chahine et al. (2005)), the Thermal Emission Spectrometer (TES, Kulawik et al. (2010)), and the Infrared Atmospheric Sounder Interferometer (IASI, Liuzzi et al. (2016)), while instruments measuring solar backscatter include the SCanning Imaging Absorption SpectroMeter for Atmospheric CHartography (SCIAMACHY, Buchwitz et al. (2005)), the Greenhouse gases Observing SATellite (GOSAT, Kuze et al. (2016)), and the Orbiting Carbon Observatory 2 (OCO-2, Eldering et al. (2017a)).

Thermal emission instruments are sensitive to CO_2 in the middle-upper troposphere whereas solar backscatter instruments have nearly-uniform sensitivity to the full atmospheric column. All of these instruments are on satellites with a polar orbit, so they observe a given location at most once per day if they rely on solar backscatter, or once per day and once per night if they rely on thermal emission. To provide a more complete picture of CO_2 evolution throughout a given day, NASA has plans to deploy a carbon-observing instrument aboard a geosynchronous satellite (GeoCARB, Polonsky et al. (2014)), which would provide continuous observations of a fixed quadrant of the globe. Also proposed is the Active Sensing of CO_2 Emissions over Nights, Days and Seasons (ASCENDS) instrument, which would measure CO_2 in the same bands as the solar backscatter instruments, but by providing a light source, could do so during nighttime hours (Kawa et al. 2010).

This work studies the utility of observations from OCO-2, which was launched in July 2014 (Eldering et al. 2017a). This instrument is the first NASA mission with the primary objective of understanding the carbon cycle (Crisp et al. 2004). The high precision ($< 0.3\%$ of the measured XCO_2), small footprint (1.25 km x 2.4 km), and sheer number (43,000 to 79,000 high-quality, cloud-free soundings per day) of measurements from OCO-2 are unprecedented among the previous components of the CO_2 observing network.

Since its launch, OCO-2 has provided observations to inform several impactful studies. Chatterjee et al. (2017) found that the strong El Niño of 2015-16 contributed a net positive source of CO_2 to the atmosphere, through decreased carbon uptake in the pan-tropical terrestrial biosphere and increased biomass burning in Indonesia and Southwest Asia, but one that was reduced by a decreased tropical Pacific source in the early stages of the event. OCO-2 provided the dense observations of CO_2 required to observe in detail the timing and location of these carbon source anomalies.

Liu et al. (2017a) further probed the response of the terrestrial biosphere to the large El Niño event, focusing on the tropical land. The authors combined the newly available XCO_2 observations from OCO-2, more XCO_2 observations from GOSAT, carbon monoxide observations from Measurements of Pollution in the Troposphere (MOPITT), and solar-induced chlorophyll fluorescence (SIF) from GOSAT with physical models using the Carbon Monitoring System Flux inversion system, to understand how and why carbon uptake in the three tropical continents (Asia, Africa, and South America) changed during the El Niño.

They found that each tropical continent contributed to the anomalous carbon source, but for different reasons. In South America, forests were less productive, resulting in reduced carbon uptake. In Asia, large fires increased carbon release. In Africa, enhanced respiration increased carbon release.

In addition to providing insight into the natural processes controlling the global carbon cycle, OCO-2 data has been used to understand and constrain anthropogenic emissions. Hakkarainen et al. (2016) demonstrated the ability of anomalies in OCO-2 XCO_2 observations to reveal emission hot spots throughout the globe. Nassar et al. (2017) showed that emissions from individual power plants can be determined with 1%-17% uncertainty when fitting OCO-2 observations to plume model simulations. Schwandner et al. (2017) showed that, in addition to detecting CO_2 outgassing from multiple volcanoes, OCO-2 observes the urban enhancement of CO_2 over the Los Angeles basin.

In the Liu et al. (2017a) study, the authors used data assimilation, which is the mathematical practice that seeks to optimally combine a forecast model with incomplete observations. In the case of Liu et al. (2017a), the observations are satellite observations of trace gases and the model is an Earth System model with coupled ocean, land, and atmospheric components. Data assimilation is used routinely for example in weather forecasting, to determine the best initial conditions for the forecasting model, or in creating an atmospheric reanalysis, where an optimal state estimate is the end goal. In the carbon cycle community, data assimilation which aims to estimate time-evolving three-dimensional atmospheric CO_2 fields is usually referred to as a state estimation, whereas when data assimilation is used to estimate the CO_2 surface flux forcing, it is called a surface flux inversion.

In weather forecasting and carbon cycle science (especially when assimilating satellite observations), the size of the problem and number of observations to assimilate are large, so the dominant techniques are sequential ensemble methods such as the ensemble Kalman filter (EnKF, Evensen (2003)), and variational methods such as 4D-Var (Courtier et al. 1992). A comparison between an ensemble Kalman filter and 4D-Var for CO_2 data assimilation shows that the two methods yield consistent fluxes across broad regions (Liu et al. 2016). The EnKF provides a measure of uncertainty (the spread in the ensemble) which variational methods do not easily provide. The EnKF is more easily parallelizable and computationally efficient than 4D-Var, which requires an adjoint model.

In Chapters 2 and 3 of this dissertation, we perform ensemble data assimilation using the ensemble adjustment Kalman filter (EAKF, Anderson (2001)) algorithm from the Data Assimilation Research Testbed (DART) toolbox (Anderson et al. 2009). DART has been tested for a variety of applications including model bias detection, chemical data assimilation, and production of a decades-long climate reanalysis (Raeder et al. 2012). DART's modular interface allows its users to easily add new observation types, test various filter, inflation, and localization choices, and its diagnostic tools allow for streamlined analysis. DART's ensemble filters are "upwardly mobile": the forecast model can be easily replaced with a later version or a different numerical model, since they do not require the derivation of the adjoint of the forecast model. Additionally, DART algorithms scale well on parallel computers (Anderson et al. 2009, 2013), which is of crucial importance when applied to global-scale, large state vector problems. The particular filter we employ in Chapters 2 and 3, the EAKF, is shown to outperform the traditional EnKF in certain applications and most notably for small ensembles (Anderson 2001).

CO_2 surface flux inversions aim to estimate CO_2 uptake and emission patterns by combining prior knowledge of these patterns with observed CO_2 atmospheric abundance and tracer transport models. These inversions are analogous to data assimilation as described above, except that they estimate the surface flux forcing instead of (or in addition to) estimating the concentration of CO_2 in the atmosphere. An early example of a surface flux inversion is Tans et al. (1990), where *in situ* CO_2 observations from several stations and partial pressure observations of CO_2 at the ocean surface are compared to modeled CO_2 fields from a general circulation model to identify a northern hemispheric land sink. A modern example of a surface flux inversion is CarbonTracker (CT) (Peters et al. 2005, 2007). CT takes advantage of a greatly expanded observation network compared to Tans et al. (1990). It uses an EnKF to optimize a set a multipliers corresponding to 135 regions of the globe. These multipliers adjust prior fluxes to match CO_2 observations from the global surface *in situ* CO_2 network over a 12-week observation window. Several other recent inversions have been performed using 4D-Var (e.g. Deng et al. (2014)).

Since satellite observations of CO_2 have become available, surface flux inversions have also been performed using this data. For example, global surface fluxes have been estimated using data from TES (Nassar et al. (2011)) and GOSAT (Basu et al. (2013); Houweling et al. (2015)) data. These satellite products suffer from biases (e.g., Chevallier (2015); Eldering et al. (2017b)) which propagate into flux estimates. In an attempt to quantify and understand biases in satellite data, the Total Carbon Column Observation Network (TCCON, Wunch et al. (2011)) was created. TCCON instruments are well-calibrated terrestrially-based analogs to instruments like OCO-2. Data from TCCON instruments has also been used in surface flux inversions (Chevallier et al. 2011).

The works that this dissertation most directly builds upon are those which use the Local Ensemble Transform Kalman Filter (LETKF) for simultaneous assimilation of weather and CO_2 observations (Liu et al. 2011, 2012). In these studies, the online assimilation of meteorological observations into the atmospheric ensemble provides a better representation of mixing than other studies which use a single representation of meteorology from a reanalysis product or from a transport model, as demonstrated in Liu et al. (2011). Liu et al. (2012) showed that in their data assimilation system, assimilating AIRS XCO_2 in addition to weather observations significantly improved the accuracy of CO_2 reanalysis fields when compared with non-assimilated CO_2 vertical profiles from aircraft. Kang et al. (2011) and Kang et al. (2012) extended the data assimilation system to include CO_2 surface flux in the state vector, thus performing a CO_2 surface flux inversion in addition to an estimation of the atmospheric state. Kang et al. (2012) demonstrated that estimating the surface flux in this way is possible under idealized conditions, and Kang et al. (2011) outlined which observations should impact the CO_2 state in order to best estimate the surface fluxes in the idealized system.

In Chapter 2 of this dissertation, we present a compromise between the state estimation in Liu et al. (2012) and the surface flux inversion in Kang et al. (2011, 2012) in that surface fluxes are not included in the state vector, but information about the surface fluxes is derived from diagnostics provided by the assimilation system and the adjustments it makes to the CO_2 mixing ratio and other meteorological state variables. In Chapter 3, we examine how we can use our carbon-weather data assimilation system to understand how CO_2 observations could potentially improve weather forecasts. In Chapter 4, we use the CO_2-weather reanalysis created by Liu et al. (2012) to derive global monthly CO_2 surface flux estimates in an offline manner.

Chapter 2

A carbon-weather data assimilation system for CO_2 emissions verification at the national scale

Abstract. We present a series of Observing System Simulation Experiments (OSSEs) assessing the ability of a carbon-weather data assimilation system to detect underreporting of CO_2 emissions at the scale of a large country. We use the ensemble adjustment Kalman filter (EAKF) from the Data Assimilation Research Testbed (DART) to assimilate synthetic observations of total-column CO_2 at the locations of (1) the Orbiting Carbon Observatory 2 (OCO-2) soundings and (2) a hypothetical observing system which observes globally at 1pm local time each day. This data is assimilated into the Community Atmosphere Model (CAM 5.0 FV), with a prognostic carbon cycle forced by CarbonTracker CO_2 surface fluxes for land, ocean, and fossil fuel sources. The fossil fuel CO_2 emissions are modified to have a -50% bias over China, but the OCO-2 observations are pulled from a model run where this bias is not present. We test whether the data assimilation system can detect the imposed bias by examining the near-surface innovation in CO_2 mass in a method similar to the mass-balance inversion. We find that with the hypothetical observation strategy, we can recover half of the imposed bias, and that the ensemble mean of the near-surface CO_2 tracks the truth during the daytime, but underestimates the truth during the unconstrained nighttime hours over the region of the imposed bias. For the OCO-2 strategy, we detect a signal at the location of the imposed bias that is obscured by problems such as observation coverage, which we discuss in detail. We discuss potential additions to the observing system which could optimize the detection of biased emissions with our data assimilation system.

2.1 Introduction

In the global carbon budget, the annual increase in atmospheric CO_2 and global annual emission from fossil fuel (FF) combustion are the two most robust terms. Together, they bracket estimates of the net land and ocean sinks. National CO_2 emissions from fossil fuel combustion are estimated from self-reported inventories of fossil fuel production or consumption, to which fuel-specific or activity-specific emission coefficients have been applied. Andres et al. (2014) put an uncertainty of 8.4% (2-σ) on global total FF emissions. In the US, estimates by the Energy Information Administration (EIA) (http://eia.gov) and EPA (https://www.epa.gov/ghgemissions/inventory-us-greenhouse-gas-emissions-and-sinks-1990-2013) differ by ∼2%.

Regional and local emissions have greater uncertainties than the global estimates, as self-reporting is not comprehensive. Furthermore, downscaling emission statistics for geo-political units to create gridded datasets necessarily involves proxies, assumptions, and models. The widely-used Carbon Dioxide Information Analysis Center (CDIAC) database apportions national, state, and provincial emissions according to population density (Andres et al. 2014). The Open-Data Inventory of Anthropogenic CO_2 (ODIAC) emission database includes point sources, and information from the Defense Meteorological Satellite Program observations of nightlights (Oda and Maksyutov 2011), while the Emission Database for Global Atmospheric Research (EDGAR, Olivier et al. (1996)) and the Fossil Fuel Data Assimilation System version 2 (FFDAScv) utilize updated data on population density, point sources and nightlights (Olivier et al. 2005; Asefi-Najafabady et al. 2014). Large differences exist between the ODIAC and "Miller" FF emission data sets used in CarbonTracker (Peters et al. 2007). The "Miller" dataset apportions global total emissions from CDIAC according to EDGAR's gridding (CT2015, https://www.esrl.noaa.gov/gmd/ccgg/carbontracker/CT2015/). Both have national emissions scaled to the same CDIAC values. A difference of 100 gC/m^2/yr in a single gridbox translates into >20 ppm column-averaged CO_2 (XCO_2) before advection.

The uncertainties in the national FF CO_2 emission estimates are illustrated by three recent studies of China. Guan et al. (2012) found that China's annual FF emission estimated by totaling provincial inventories is higher than that from national reports by as much as 0.38 PgC (1.4 gigatonnes CO_2) for 2010. They aver that the "bottom-up" national statistics capture mainly large-scale power production and consumption, but miss local and regional emissions. Figure 2.1 shows China's fossil fuel emissions as estimated by different organizations. The difference between the provincial total and the widely-used CDIAC estimates amounts to 0.3 PgC/yr for 2010. In contrast, a follow-on study Liu et al. (2015) obtains much lower emissions, ∼14% (0.35 PgC) lower than EDGAR estimates for 2013. They re-examined the carbon content, heat content, and oxidation states of the different fuels, and found that the emission coefficients of Chinese coal are ∼40% lower than the values recommended by the IPCC. 0.35 PgC/yr is approximately double the estimated carbon sink in forests in China (Pan et al. 2011). If 0.3 PgC were evenly distributed in the atmosphere over China (area = 9.4x10^6 km^2), that translates to a column-average difference of 5 ppm. For 2014, IEA estimated a 1.5% reduction in China's FF emissions while BP estimates a 0.9% increase over the previous year (Korsbakken et al. 2016).

"Top-down" approaches for inferring CO_2 sources and sinks from the spatial and temporal variations in the abundance of CO_2 in the atmosphere are useful for cross-checking "bottom-up" estimates such as described above. The realism of surface fluxes inferred from

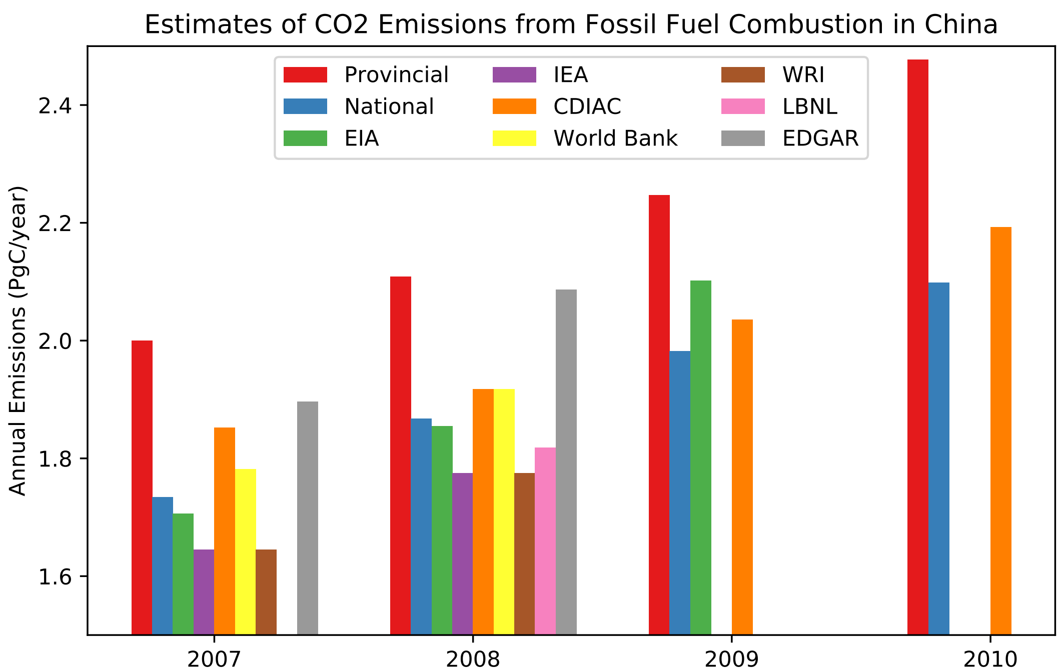

Figure 2.1: Estimates of fossil fuel CO_2 emissions from China by different approaches or organizations (adapted from Table 2 of Guan et al. (2012))

atmospheric CO_2 observations is thus contingent on the realism of atmospheric transport and mixing. Most inversion or data assimilation studies utilize atmospheric circulation statistics from a general circulation model or from a meteorological reanalysis product. While reanalysis represents the optimal estimation of the atmospheric circulation based on the available observations and the weather forecast or atmospheric circulation model, the verisimilitude of the product depends on the observations used and the model itself. For example, Trenberth and Fasullo (2013) show that globally-averaged net radiation at the top of the atmosphere estimated by several reanalysis products can differ from actual values by as much as 10 W/m^2 and fail to capture the signatures of a quiet sun or the eruption of Mount Pinatubo. This has consequences for transport and CO_2 fluxes.

Indeed, disparate surface CO_2 fluxes are inferred from different transport models with different meteorology, or from different meteorology in a single transport model (Gurney et al. 2003; Baker et al. 2004; Chevallier et al. 2010; Houweling et al. 2010). Underestimation of inter-hemispheric transport (e.g. Denning et al. (1999)) and/or underestimation of vertical mixing in northern mid-latitudes (e.g. Stephens et al. (2007)) in an atmospheric circulation model would lead to an overestimate of the northern hemisphere CO_2 sink. Furthermore, not often considered are inherent uncertainties in the reanalysis product, such as large spread in meteorological fields in stormy regions (e.g. Kalnay (2003)) where intense turbulence and mixing deliver surface CO_2 aloft to the regions of fast winds, leading to large spreads in CO_2 fields, especially aloft.

The Orbiting Carbon Observatory 2 (OCO-2), launched into orbit in July of 2014, provides unprecedented observations of the column mixing ratio of CO_2 (XCO_2) in the atmosphere (Eldering et al. 2017a). One stated goal of satellite CO_2 observations is climate treaty verification (National Research Council 2010). This study is a first attempt to assess the feasibility of satellite CO_2 observations to detect biases in national-scale CO_2 emissions when realistic transport uncertainties are included. We present a series of observation system simulation experiments (OSSEs) as a proof of concept for a carbon-weather data assimilation (DA) system to be used to detect biases in national-scale CO_2 emissions reports. Uncertainties in land fluxes, which are much greater than those of fossil fuel emissions, are beyond the scope of this first study that includes transport uncertainties.

A central aspect of the DA system in this study is the simultaneous assimilation of weather and CO_2 observations into a single global carbon-climate model. The state vector thus includes meteorologic variables in addition to CO_2 at each model gridbox. The observation operator, or forward operator ($\mathcal{H}$), that transforms the background state variables to observation space is generally simple selection and interpolation of model forecasts to the location and time of the observations. The assimilation window is six hours, meaning that every six hours, the Ensemble Adjustment Kalman Filter (EAKF) seeks the “analysis”, or optimal fit between the observations and the transformed (by $\mathcal{H}$) model forecasts. The dynamic model $\mathcal{M}$, the carbon-weather model CAM5, then uses the meteorological and CO_2 analyses as its initial condition, and forecasts the ensemble of the state vector for the next six hours using the prior prescribed surface fluxes. The outcome is a reanalysis product of the atmospheric state, including CO_2. From the ensemble of 4D states of the atmosphere, potential corrections to the prior surface fluxes are estimated *a posteriori* via mass balance. Uncertainties in these surface flux corrections can then be assessed against contemporaneous uncertainties in the meteorology.

The carbon-weather DA system in this study follows from Liu et al. (2012) and Kang et al. (2011), which have meteorology and CO_2 in the state vector. Liu et al. (2012) first demonstrated a similar DA system's ability to simultaneously assimilate raw weather observations and upper-tropospheric CO_2 from the Atmospheric Infrared Sounder (AIRS). In doing so, the authors found that assimilating AIRS CO_2 in addition to weather observations markedly improved the accuracy of CO_2 reanalysis fields when compared with aircraft profiles which were not assimilated. Kang et al. (2011) and Kang et al. (2012) extended the DA system to include CO_2 surface flux in the state vector, and as such performed a flux inversion in addition to a state estimation. Kang et al. (2012) demonstrated that estimating the surface flux in this way is possible under idealized conditions, and Kang et al. (2011) outlined the "variable localization" schemes which are best able to estimate the surface flux in the system. This current study serves as a compromise between a state estimation and a full surface flux inversion in that the surface fluxes are not included in the state vector, but information about the surface fluxes is derived from diagnostics provided by the assimilation system and the adjustments it makes to the CO_2 mixing ratio and other meteorological state variables.

The DA system presented here is different from the CarbonTracker (CT) family of CO_2 DA systems (Peters et al. 2005, 2007; Feng et al. 2009), even though they are also focused on flux inference. The state variables in CarbonTracker are λ_i, multipliers associated with N weekly surface fluxes for each of 135 regions spanning the globe. The forward operator ($\mathcal{H}$) is the tracer transport model TM5 which ties atmospheric CO_2 to the N weeks of CO_2 surface flux analysis. CO_2 transport in TM5 uses a single realization of ECMWF (ERA-interim) winds and, starting with the CT2013 product, applies a "convective flux fix" by using convective fluxes directly from the ERA-interim parent model. The Square Root Ensemble Kalman Filter then compares the CO_2 forecast and the observations for the last of the N weeks and updates the N weekly surface fluxes for the regions. Lacking a dynamical model $\mathcal{M}$ to advance the state vector λ_i by a week, Peters et al. (2005, 2007) assumed persistence, or $\mathcal{M} = \mathcal{I}$. In the 2017 version of CarbonTracker, N is 12, and $\mathcal{M}$ averages λ_i over three time steps to advance the state vector by two weeks.

The simultaneous assimilation of weather observations into the same global atmospheric model yields the best approximation to the true atmospheric circulation that is consistent with the CO_2 observations, within the construct of the atmospheric model. The ensemble approach provides not only estimates of the uncertainties in the meteorological and CO_2 fields, but also maintains the nonlinearities contained in the climate model, especially those associated with convection (Liu et al. 2011). It also avoids the incompatibility between the mean reanalysis fields and the mixing representation.

The paper is organized as follows. Section 2.2 describes in detail the model, observations, data assimilation, and inversion methods used for this study. Section 2.3 presents results from the OSSEs. Final conclusions and some discussion on optimizing our carbon observing system can be found in Section 2.4.

2.2 Methods

Here we present the formulation of the global carbon-climate model (Section 2.2.1) into which standard weather and satellite CO_2 observations are assimilated using DART (Section 2.2.2). We also describe our mass-balance method for detecting emissions bias in Section 2.2.3.

In each OSSE, "truth" is represented by a single integration of the carbon-climate model that uses fossil fuel, land, and ocean CO_2 fluxes from CarbonTracker (version 2015). To produce the "analysis", i.e. the ensemble of optimized atmospheric states, an ensemble of 30 model forecasts of weather and CO_2 are merged, every six hours, with the observations using DART. The spread among the ensemble members captures the uncertainties in meteorology and CO_2.

Three experiments are carried out, each with the FF emissions from China biased low by 50%. All three experiments sample weather observations from the "truth" run according to times and locations of the observations (Section 2.2.4). They also sample column-averaged CO_2 (XCO_2) from the "truth" run in a manner that reflects one of two satellite observation strategies. Experiment *Ideal* uses simulated XCO_2 observations from a hypothetical satellite which observes globally each day at 1pm local time. This is similar, for example, to the observation strategy used by the TROPOspheric Monitoring Instrument (TROPOMI) (Borsdorff et al. 2018), which measures a number of trace gases but not CO_2. Similar global daily coverage could also be achieved with a constellation ∼8 of OCO-2-like instruments. Experiments *October* and *November* sample XCO_2 observations according to the OCO-2 orbit, which has an equatorial overpass time of 1:30pm local time. Experiments *October* and *November* differ in the time of year they simulate and hence the northernmost extent of XCO_2 observation availability. Prior to imposing the emission bias, each experiment requires an ensemble spin-up, during which time the spread among the ensemble of atmospheric states is developed. This is described in section 2.2.7 and section 2.2.8. Following the ensemble spin-ups, the emission biases are imposed, and the experiments are integrated for two (*October*, *November* experiments), or four (*Ideal* experiment) weeks.

2.2.1 The Dynamic Model $\mathcal{M}$: CESM-CAM with CO_2 cycle

Our carbon-weather data assimilation system has two central components: the carbon-climate model and the data assimilation (DA) system. The carbon-climate model is the Community Earth System Model (CESM 1.2.1) from the National Center for Atmospheric Research (NCAR). This model couples many Earth system components including atmosphere, land, ocean, ice, and biogeochemistry. For this work, we use the component set AMIP_CAM5_CLM40% CN_CICE% PRES_DOCN% DOM_RTM_SGLC_SWAV. This is essentially the same setup as in Raeder et al. (2012) except that we have allowed the carbon cycle to be prognostic.

The atmospheric model used is the Community Atmosphere Model (CAM) 5.0FV (Neale et al. 2012) with a prognostic carbon cycle, a horizontal resolution of 2.5° longitude x 1.9° latitude, and 30 levels in the vertical. Although our CESM component set calculates land and ocean carbon fluxes interactively (as a function of the model's climate), we prescribe the surface CO_2 fluxes in the OSSEs to be the monthly fluxes from CarbonTracker 2015 (Peters et al. 2007). These CO_2 fluxes from the terrestrial biosphere (including fire), from the ocean, and from fossil fuel emissions together satisfy the global carbon budget for 2015, and are used separately as forcing for their respective tracers (C_{land}, C_{ocean}, and C_{fossil}) in the atmosphere. In addition to these three tracers, CAM5.0FV transports a fourth tracer, C_{total}, forced by the sum of the fluxes. The fluxes are linearly interpolated from their monthly values to the model time resolution of six hours, so no diurnal cycle is included in our CO_2 surface flux model.

2.2.2 Data Assimilation Research Testbed (DART)

Ensemble data assimilation is used to best estimate the atmospheric state given our observations, model forecasts, and their relative uncertainties. For this study we use the ensemble adjustment Kalman filter (EAKF) in NCAR's Data Assimilation Research Testbed (DART) (Anderson et al. 2009). DART is a robust platform that has been used with CAM for creation of a reanalysis product of atmospheric circulation (Raeder et al. 2012), and with CAM-Chem for numerous trace gas studies (e.g. Barré et al. (2015); Liu et al. (2017b)).

We will first describe the mathematical procedure followed by this algorithm ("Filter Description" section) before providing the particular implementation choices for the filter ("Filter Implementation" section) that were used in this work.

Filter Description

The EAKF adjusts model forecasts to account for observations, taking into account uncertainties in both observations and forecasts. This section follows notation similar to that of Barré et al. (2015) to describe the mathematical functioning of the EAKF. A particular ensemble member is denoted with subscript k, model space variables are represented by x (where x is one of the variables in the model state vector $\vec{x} = [u, v, T, P, q, tracers]$), and observation space variables are represented by y. For y, subscript o refers to observations and subscript m refers to model forecast quantities that have been transformed to observation space for comparison.

An assimilation cycle starts with a six-hour model (CAM) advance of each of our K ensemble members. This produces an ensemble forecast of the model state, which can be thought of as the prior or background forecast to be updated by the filter. We denote this background ensemble with superscript f, so the background forecast of ensemble member k is x_k^f.

Prior to transforming these forecasts to observation space, we perform adaptive inflation as in Raeder et al. (2012) and Barré et al. (2015). An inflation factor λ, which varies in space, time, and variable, is applied to the model forecasts according to the equation:

$$x_k^f = \sqrt{\lambda}(x_k^f - \overline{x}^f) + \overline{x}^f \tag{2.1}$$

This step helps prevent filter divergence by increasing the spread (σ_m^f) among the forecast ensemble members. For a detailed description of the adaptive inflation employed here, we refer the reader to Anderson (2009).

Each forecast x_k^f is then transformed from model space to observation space using a forward operator $\mathcal{H}$ (the observation operator), yielding $y_{m,k}^f$ – our expected observations given the model forecasts:

$$y_{m,k}^f = \mathcal{H}(x_k^f) \tag{2.2}$$

Here the subscript m denotes that these are observation-like quantities calculated from the forecast model. Each observation type has its own forward operator. In the simplest case, a near-surface temperature "observation" is calculated from the model state by interpolating surrounding grid box temperature values to the location of the observation. For more information on our XCO_2 forward operators, see section 2.2.5.

Using all $y_{m,k}^f$ we can calculate the ensemble mean ($\overline{y}_m^f$) and "spread" (σ_m^f), i.e. the standard deviation, among ensemble members of the forecast in observation space.

Following the inflation step, DART's EAKF calculates the analysis $y_{m,k}^a$ by adjusting each background forecast $y_{m,k}^f$ as described in Anderson (2003). The analysis is given by :

$$y_{m,k}^a = \sqrt{\frac{\sigma_o^2}{\sigma_o^2 + (\sigma_m^f)^2}}(y_{m,k}^f - \overline{y}_m^f) + \frac{\frac{\overline{y}_m^f}{(\sigma_m^f)^2} + \frac{y_0}{\sigma_o^2}}{\frac{1}{(\sigma_m^f)^2} + \frac{1}{\sigma_o^2}} \tag{2.3}$$

This procedure results in an ensemble mean, $\overline{y}_m^a$, which is closer to the observation y_o and a reduced ensemble spread (σ_m^a). The observation space increment is then given by:

$$\Delta y_{m,k} = y_{m,k}^a - y_{m,k}^f \tag{2.4}$$

This increment in model space is then calculated as:

$$\Delta x_k = \alpha \frac{cov(x^f, y_m^f)}{(\sigma_m^f)^2} \Delta y_{m,k} \tag{2.5}$$

Here the increment Δx_k is proportional to the observation increment ($\Delta y_{m,k}$) times the covariance of x^f and y_m^f across the ensemble ($cov(x^f, y_m^f)$) divided by the variance across model forecasts ($(\sigma_m^f)^2$). The factor α is applied to localize the covariance in space. This factor allows us to minimize sampling error by allowing observations to update the model state (via increments Δx_k) less and less as the distance between the model state location and the observation location increases.

Our chosen α is the fifth-order polynomial Gaspari-Cohn (GC) correlation function (Gaspari and Cohn 1999), which limits the impact of an observation to a volume centered on the observation. The GC function is a compactly-supported approximation of a Gaussian with a maximum value of 1 at the location of the observation. The rate at which the function falls off in distance is set by a half-width parameter, which is half the distance at which the GC value goes to 0. For all meteorological observations used in these experiments, we choose a horizontal half-width of 0.2 radians (∼1200 km) and a vertical half-width of 400 hPa, following examples of successful assimilations of Raeder et al. (2012) and Barré et al. (2015). For the total column CO_2 observations (XCO_2), we also use a 0.2 radian half-width for the horizontal correlation function, but we do not localize in the vertical as some do when assimilating total-column trace gas observations (e.g. as Barré et al. (2015) do with CO). Barré et al. (2015) chose to perform vertical localization of MOPPITT and IASI CO observations by maximizing the impact of observations on the state at the averaging kernel's peak value. For OCO-2 soundings, the averaging kernel is much flatter than the CO observations used in this study, so a similar approach to vertical localization in our case is less straightforward.

The model space increments (Eq. 2.5, also called the innovation) are added to the model forecasts to give analyses $x^a_{m,k}$ (also called posterior states):

$$x^a_{m,k} = x^f_{m,k} + \Delta x_{m,k} \tag{2.6}$$

The analyses $x^a_{m,k}$ then become the initial conditions for the next assimilation window.

Filter implementation

We emphasize that we assimilate meteorological observations simultaneously with CO_2 observations, and that these meteorological observations impact the CO_2 tracers in our state vector. This is unique to our system, compared to other carbon data assimilation and inversion systems. The assimilation of weather observations yields the best approximation to the true atmospheric circulation that is contemporaneous with the CO_2 observations.

Our state vector is $\vec{x} = [u,\, v,\, P,\, T,\, q,\, C_{fossil},\, C_{total}]$, where u and v are horizontal wind fields, P is surface pressure, T is temperature, q is specific humidity, C_{fossil} is the mixing ratio for the fossil fuel CO_2 tracer, and C_{total} is the mixing ratio for the combined CO_2 tracers ($C_{land} + C_{ocean} + C_{fossil}$). The assimilation window is six hours for all state variables.

We use a small ensemble size of 30. This choice was made considering the tradeoff between optimal filter behavior and computational cost. We also note that Anderson (2001) shows that the EAKF outperforms the traditional ensemble Kalman filter for small ensembles, and that other trace gas assimilation experiments have yielded good results using an ensemble size of 20 or 30 (e.g. Barré et al. (2015); Liu et al. (2017b)).

Our choice of an ensemble method allows us to retain nonlinearities contained in the climate model, especially convection, as demonstrated by Liu et al. (2011). It also avoids the incompatibility between the mean reanalysis fields and the mixing representation. The ensemble grants us a measure of uncertainty in our weather fields for every six-hour forecast. In Figure 2.2 we show the spread (σ^f_m) among forecasted meteorological state variables for the assimilation window at the beginning of the *October* experiment.

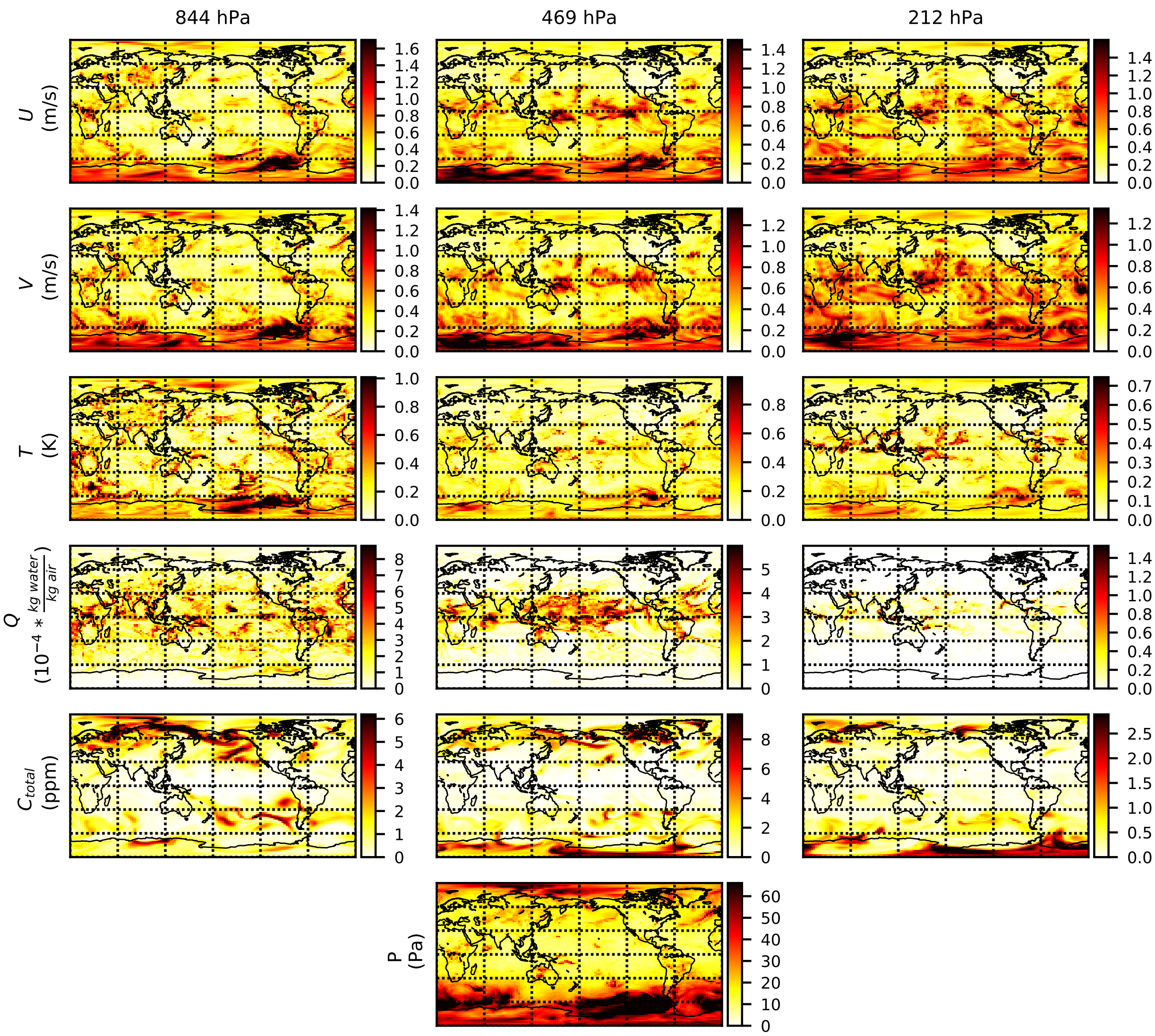

Figure 2.2: Snapshots of the spreads (σ_m^f) among our ensemble of forecasts for state variables at the start of the *October* experiment (after spinning up the ensemble). From top to bottom, we show spreads in: winds u and v (in meters per second), temperature T (in °C), specific humidity q (in 10^{-4} x kg H_2O/kg total air), and the concentration of CO_2 C_{total} (in ppm), all at 3 different model levels (844 hPa, 469 hPa, and 212 hPa). The bottom panel shows the spread in surface pressure P (in Pascals).

2.2.3 Innovation approach for emissions bias detection

To estimate any bias in emissions, we examine the innovation in CO_2 mass for the lower portion of the atmospheric column that is sensitive to the surface flux forcing. This calculation comes after the experiments are run. In other words, rather than update the flux iteratively online, by including it in the state vector, we examine how the CO_2 mass was updated by the observations, and see whether this update (i.e., the innovation), when summed in time over the duration of each experiment, resembles our imposed bias over the same period. If we were to add back this innovation to our surface flux forcing, re-run the assimilation, and repeat this process iteratively until the innovation stabilizes at a small value, this approach would be analogous to the mass-balance inversion / data assimilation approach employed by Dargaville and Simmonds (2013).

We first note that equation 2.6 can be rearranged such that we can calculate the innovation Δx_k from the model forecast and analysis:

$$\Delta x_k = x_k^a - x_k^f \tag{2.7}$$

Here, and in the following derivations, we drop the m subscripts for brevity since we only work in model space in this section.

For a given state variable x, the corresponding ensemble mean innovation ($\Delta\overline{x}$) and spread in innovation ($\sigma_{\Delta x}$) are then:

$$\Delta\overline{x} = \overline{x}^a - \overline{x}^f \tag{2.8}$$

$$\sigma_{\Delta x} = \sqrt{(\sigma_x^a)^2 + (\sigma_x^f)^2} \tag{2.9}$$

Here, and throughout this section, we combine spreads from the analysis and forecast variables assuming they are uncorrelated, random errors. Of interest for the calculation of CO_2 mass innovation are the state variables C_{fossil}, P, and q, each of which has its own ensemble mean ($\overline{C_{fossil}}$, $\overline{P}$, $\overline{q}$) and spread ($\sigma_{C_{fossil}}$, σ_P, σ_q). For brevity, in the remainder of this section we drop the $fossil$ subscript from C_{fossil}.

We aim to convert $\Delta\overline{C}$ in each grid box and each vertical level from its model mass fraction units (kgCO_2/kg dry air) to mass flux units (kgCO_2/m^2/s), then integrate in the vertical the layers that are sensitive to surface fluxes. We call the resulting derived quantity the mean flux innovation ($\Delta\overline{\Phi}$):

$$\Delta\overline{\Phi} = \overline{\Phi}^a - \overline{\Phi}^f \tag{2.10}$$

We define an intermediate quantity A as the mass of total air per area in each atmospheric level (with units kg air/m^2). A is derived from P and the parameters ($hyai$, $hybi$, and P_0) that define CAM5's hybrid sigma coordinates. The ensemble mean ($\overline{A}$) and spread (σ_A) are given in equations 2.11 and 2.12, respectively. At this point, we drop superscripts a and f and note that each derived quantity leading up to $\overline{\Phi}^a$ and $\overline{\Phi}^f$ is calculated separately using the ensemble mean and/or spread of either the analysis or forecast state variables. For clarity, we also include the indices for the various dimensions (longitudinal i, latitudinal j, vertical l, and time n) in parentheses following nonscalar quantities.

$$\overline{A}(i,j,l,n) = \frac{1}{g}[hyai(l+1) - hyai(l)] * P_0 + \frac{1}{g}[hybi(l+1) - hybi(l)] * \overline{P}(i,j,n) \tag{2.11}$$

$$\sigma_A(i,j,l,n) = \frac{1}{g}[hybi(l+1) - hybi(l)] * \sigma_P(i,j,n) \tag{2.12}$$

Here g is the gravitational constant (9.8 m/s^2) and P_0 is the reference pressure in Pascals.

$\overline{C}$ (units kgCO_2/kg dry air) is then converted to $\overline{c}$ (units kgCO_2/m^2) using $\overline{q}$ (kgH_2O /kg air), and $\overline{A}$ (kg air /m^2) in equation 2.13.

$$\overline{c}(i,j,l,n) = \overline{C}(i,j,l,n) * (1 - \overline{q}(i,j,l,n)) * \overline{A}(i,j,l,n) \tag{2.13}$$

The spread about $\overline{c}$ is calculated using the ensemble mean quantity $\overline{c}$ and ensemble spreads σ_C, σ_q, and σ_A in the following manner:

$$\sigma_c(i,j,l,n) = \overline{c}(i,j,l,n)\sqrt{\left(\frac{\sigma_C(i,j,l,n)}{\overline{C}(i,j,l,n)}\right)^2 + \left(\frac{\sigma_q(i,j,l,n)}{\overline{q}(i,j,l,n)}\right)^2 + \left(\frac{\sigma_A(i,j,l,n)}{\overline{A}(i,j,l,n)}\right)^2} \tag{2.14}$$

We sum over CAM5's bottom 12 layers, from the surface to about 525 hPa, to get $\overline{\Phi}^a$ and $\overline{\Phi}^f$, and their corresponding spreads:

$$\overline{\Phi}(i,j,n) = \frac{1}{\Delta t}\sum_{l=1}^{12}\overline{c}(i,j,l,n) \tag{2.15}$$

$$\sigma_\Phi(i,j,n) = \frac{1}{\Delta t}\sqrt{\sum_{l=1}^{12}\sigma_c(i,j,l,n)^2} \tag{2.16}$$

Here Δt is six hours, expressed in seconds, so that units for $\overline{\Phi}$ and σ_Φ are kgCO_2/m^2/s (the same units as the surface flux forcing). The choice of including up to 525 hPa is discussed further in the results section (section 2.3). Combining equations 2.10 and 2.13 gives us a mean flux innovation ($\Delta\overline{\Phi}$) for each six-hour assimilation window and each grid box. The spread ($\Delta\sigma_\Phi$) about the mean innovation is then calculated as:

$$\sigma_{\Delta\Phi}(i,j,n) = \sqrt{(\sigma_\Phi(i,j,n)^a)^2 + (\sigma_\Phi(i,j,n)^f)^2} \tag{2.17}$$

We integrate $\Delta\overline{\Phi}$ over the multi-week time period of the experiments, to get a cumulative mean flux innovation, $\Sigma_{\Delta\overline{\Phi}}$:

$$\Sigma_{\Delta\overline{\Phi}} = \int_{t_0}^{t_{final}} \Delta\overline{\Phi}dt \tag{2.18}$$

$\Sigma_{\Delta\overline{\Phi}}$ is then the quantity that is compared to the imposed bias summed over the experimental period. Its spread, $\sigma_{\Sigma\Delta\Phi}$, is calculated by summing $\sigma_{\Delta\Phi}$ in quadrature, from the start of the experiment to the final time step of the experiment (T_{final}):

$$\sigma_{\Sigma\Delta\Phi}(i,j) = \sqrt{\sum_{n=1}^{T_{final}} \left(\sigma_{\Delta\Phi}(i,j,n)\right)^2} \tag{2.19}$$

This spread in the cumulative mean flux innovation can be used to determine the significance of the $\Sigma_{\Delta\overline{\Phi}}$ signals.

2.2.4 The Observations

XCO_2 : Realistic OCO-2 super-obs

We sample total column CO_2 from the "true" atmosphere at the locations of OCO-2 10-second (∼67.5 km along-track) grouped observations or "super-obs." These grouped observations were developed by David Baker for an OCO-2 flux intercomparison project among inverse modeling groups. The intent behind this data product is to transform the OCO-2 XCO_2 observations from their dense coverage and small footprints to a scale that is closer to that of the transport models employed by the various flux inversion teams. These transport models, like our atmospheric model, use grid boxes more than 100 km in the horizontal, such that dozens of CO_2 soundings are retrieved in each box.

These super-obs use only "good" quality observations, as determined by both the *xco2 quality flag* provided with the OCO-2 Level 2 data and the *xco2 warn level*. They exclude observations with an *xco2 quality flag* value of 1, and *xco2 warn level* value of more than 18. They also exclude data with *land water indicator* = 2 ("inland water") and *land water indicator* = 3 ("mixed land/ water scenes"). The observation coverage for the two experiments that use this data (*October* and *November*) can be seen in Figure 2.3.

Here we give a step-by-step guide on how the super-obs were computed, since this computation was used to calculate the uncertainties we use in our experiments, as well as the averaging kernels and pressure levels used in our OCO-2 XCO_2 forward operator. In this section we use the following notation: X_{CO_2} is the pressure-weighted dry air CO_2 mixing ratio column average. $\sigma_{X_{CO_2}}$ is the uncertainty in X_{CO_2}. $\mathbf{a}$ is the averaging kernel vector associated with the retrieval of X_{CO_2}. v is any of the parameters associated with the X_{CO_2} retrieval, such as surface albedo or aerosol optical depth. J is the number of X_{CO_2} retrievals that go into the 1-second averages. K is the number of X_{CO_2} retrievals that go into the 10-second averages.

The super-obs are developed in two steps. They are first grouped across 1-second spans, then these grouped observations are grouped across 10-second spans. In this way, if many observations are located close to one another (e.g. within 1 second of one another), they will not disproportionately impact the 10-second super-ob or the model state upon assimilation.

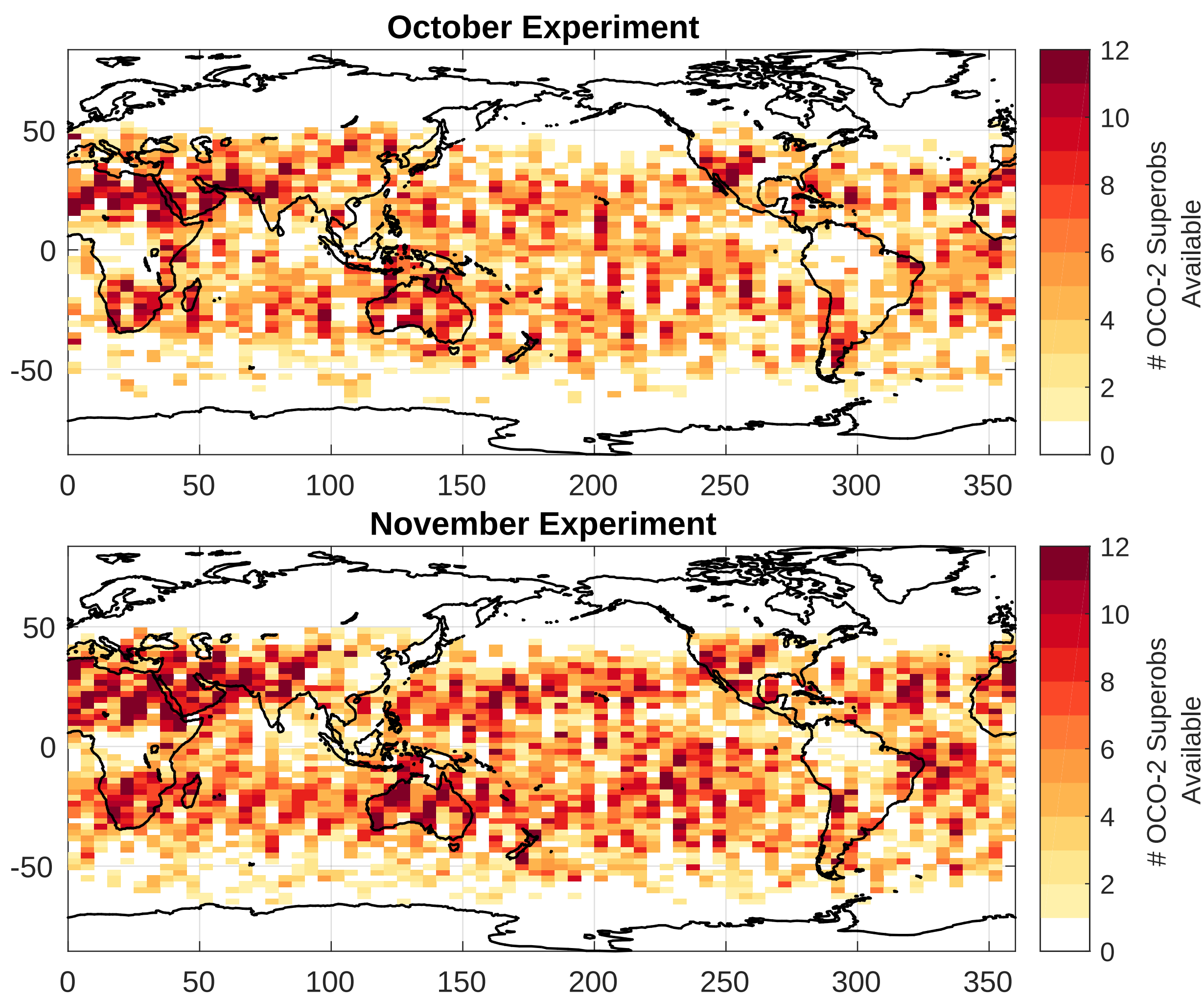

Figure 2.3: OCO-2 super-ob counts falling during the *October* (upper panel) and *November* (lower panel) experiments.

The observations themselves, and their uncertainties, are averaged across these scales. In the first step, up to 24 measurements j in each 1-second span k are averaged, assuming their errors are completely correlated:

$$v_k = \sigma_{\Sigma_{1s}}^{+2} \sum_{j=1}^{J} \sigma_j^{-2} v_j \tag{2.20}$$

$$X'_{CO_{2k}} = \sigma_{\Sigma_{1s}}^{+2} \sum_{j=1}^{J} \sigma_j^{-2} X'_{CO_{2j}} \tag{2.21}$$

$$\mathbf{a}_k = \sigma_{\Sigma_{1s}}^{+2} \sum_{j=1}^{J} \sigma_j^{-2} \mathbf{a}_j \tag{2.22}$$

$$\sigma_{\Sigma_{1s}}^{-2} = \sum_{j=1}^{J} \sigma_j^{-2} \tag{2.23}$$

Here σ_j is the uncertainty in XCO_2 as calculated by the retrieval algorithm and given in the daily OCO-2 Lite files.

The 1-second measurement's uncertainty σ_k is then calculated as follows:

$$\sigma_k^{-2} = \frac{1}{J}\sigma_{\Sigma_{1s}}^{-2} = \frac{1}{J}\sum_{j=1}^{J} \sigma_j^{-2} \tag{2.24}$$

In this way, the uncertainty is an average of the uncertainties in the group rather than one that decreases by a factor of $1/\sqrt{J}$.

There is then also a spread for the parameters v in this group, which can be calculated with:

$$\sigma_v^2 = (\sum_{j=1}^{J} v_j^2 - \frac{1}{J}[\sum_{j=1}^{J} v_j]^2)/(J-1) \tag{2.25}$$

Similarly, the spread among XCO_2 retrievals in the 1-second span is:

$$\sigma_s^2 = (\sum_{j=1}^{J} {X_{CO_2j}}^2 - \frac{1}{J}[\sum_{j=1}^{J} X_{CO_{2j}}]^2)/(J-1) \tag{2.26}$$

Next, the 1-second span quantities are grouped along 10-second spans. Here K, the number of 1-second values going into the 10-second super-ob, will be ≤ 10. In this procedure, the 1-second scale quantities are weighted by the inverse of their uncertainty, squared. This uncertainty is either σ_k (the average reported uncertainty) or, if this value is smaller than σ_{spread} (the spread in the XCO_2 retrievals that comprise the 1-second observation), σ_{spread} is used in the weighting. This rule is expressed as:

$$\sigma_{\Sigma_k}^2 = max(\sigma_k^2, \sigma_{spread}^2) \tag{2.27}$$

Here σ_{spread} is a version of σ_s that takes into account the case where only one observation goes into the 1-second super-ob in the following way:

$$\sigma^2_{spread} = max(\sigma^2_s, \epsilon^2_{base}/N) \tag{2.28}$$

Here N is the number of retrievals that went into the 1-second super-ob and the base errors (ϵ_{base}) are:

$$\begin{aligned} \epsilon_{base} &= 0.8 \text{ ppm over land} && (2.29)\\ &= 0.5 \text{ ppm over ocean} && (2.30) \end{aligned}$$

The 10-second super-obs are then calculated across the K 1-second super-obs in the following way, with these $\sigma^2_{\Sigma_k}$ quantities as weights.

$$v_{10s} = \sigma^{+2}_{\Sigma_{10s}} \sum_{k=1}^{K} \sigma^{-2}_{\Sigma_k} v_k \tag{2.31}$$

$$X'_{CO_2 10s} = \sigma^{+2}_{\Sigma_{10s}} \sum_{k=1}^{K} \sigma^{-2}_{\Sigma_k} X'_{CO_2 k} \tag{2.32}$$

$$\mathbf{a}_{10s} = \sigma^{+2}_{\Sigma_{10s}} \sum_{k=1}^{K} \sigma^{-2}_{\Sigma_k} \mathbf{a}_k \tag{2.33}$$

$$\sigma^{-2}_{\Sigma_{10s}} = \sum_{k=1}^{K} \sigma^{-2}_{\Sigma_k} \tag{2.34}$$

$\sigma_{\Sigma_{10s}}$ is then used to calculate σ_{meas}, the average 10-second measurement uncertainty:

$$\sigma^{-2}_{meas} = \frac{1}{K}\sigma^{-2}_{\Sigma_{10s}} = \frac{1}{K}\sum_{k=1}^{K} \sigma^{-2}_{\Sigma_k} \tag{2.35}$$

We note again that this is an average of the uncertainties, rather than an uncertainty calculated by summing information, so σ is not reduced by a factor of $\frac{1}{K}$.

The groups who are involved in the inversion intercomparison project additionally add a model error σ_{model} to σ_{meas} to get an increased XCO_2 error for their experiments:

$$\sigma^2_{10s} = \sigma^2_{meas} + \sigma^2_{model} \tag{2.36}$$

In our experiments, we do not include this model error term and instead specify the measurement error variance for XCO_2 as σ^2_{meas} from equation 2.35. These numbers likely underestimate the true error of the observations, but they are used as a conservative lower limit on our confidence in the measurements.

Our forward operator uses several quantities in addition to the XCO_2 values and XCO_2 error variances. These include the averaging kernels (10-second version calculated by equation 2.33), the pressure levels, *a priori* CO_2 profile, and the *a priori* XCO_2 used by the retrieval algorithm (all represented by equation 2.31).

XCO_2 : Idealized observations

In addition to the realistic OCO-2-like sampling strategy, we employ a more idealized strategy where XCO_2 is sampled daily at every grid box in our model at 1pm local time. For these observations, we uniformly set the observation error variance to 1 ppm. The nominal goal for the OCO-2 mission was for the uncertainty in the observations to be less than ~0.3% (1 ppm) on regional scales (Crisp et al. 2004). Thus, estimating error variances as 1 ppm for our hypothetical instrument is a simplistic but not unrealistic choice.

Meteorological observations

To best constrain the CO_2 transport, we assimilate standard weather observations alongside XCO_2. Previous work has shown that simultaneously assimilating weather observations and CO_2 observations yields more realistic convective transport than when reanalysis winds are employed (Liu et al. 2011).

Like the OCO-2 observations, the meteorological "observations" are sampled from the "truth" run at the times and locations of real observations. The observations used for this sampling include a suite of wind, temperature, and humidity observations from aircraft, radiosonde, and satellite instruments. The full types of observations are enumerated in Table 2.1, along with their uncertainties. Example observation coverage for some of these types is shown in Figure 2.4.

2.2.5 Forward operator $\mathcal{H}$

For each observation type that we assimilate, a unique forward operator is used to translate state variables into observation space. The forward operators for the meteorological observations for the most part involve interpolating model state variables to the location of the observations, so here we focus on the XCO_2 operators, which differ between the *Ideal* experiment and the *October/November* experiments.

For the "idealized" XCO_2 observations, we use a simplified forward operator that assumes a flat averaging kernel (i.e. that the instrument is equally sensitive to changes in CO_2 at any pressure level). Hence y_{model} is a pressure-weighted sum of the model CO_2:

$$y_{model} = 10^6 \cdot \frac{\mu_{dryair}}{\mu_{CO_2}} \cdot \frac{\int c_{model} dp_{dry}}{\int (1 - q_{model}) dp} \tag{2.37}$$

Here μ_{dryair} and μ_{CO_2} are the molar masses of dry air and CO_2, p_{dry} is the partial pressure of dry air, and q_{model} is the model's specific humidity. The observation error variance for these idealized observations is set to 1 ppm for each of the observations.

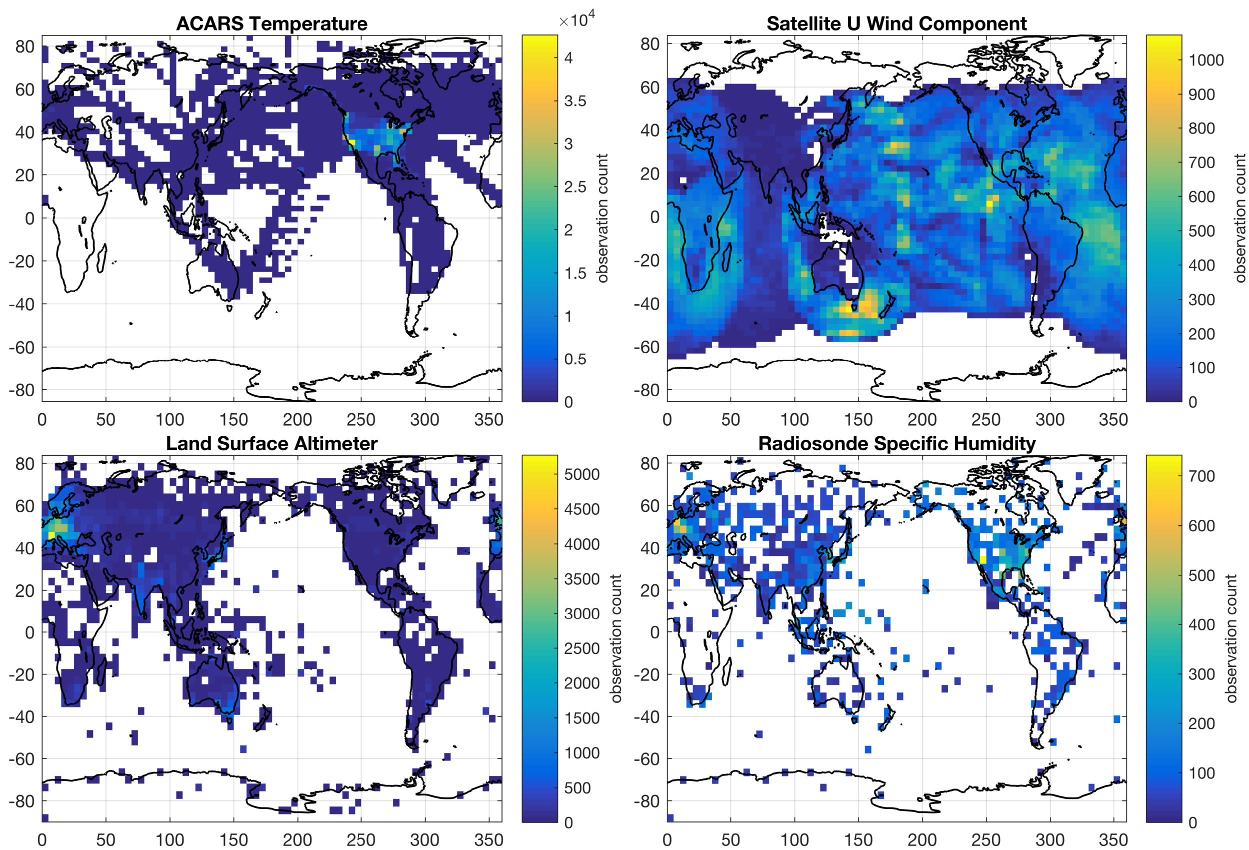

Figure 2.4: Counts of available observations for some representative observation types during a 2-day period at the start of the *October* experiment (10/22 through 10/24). ACARS temperature (upper left), Satellite U wind (upper right), land surface altimeter (lower left), and radiosonde specific humidity (lower right) are shown. Wind, temperature, and humidity observation counts include available observations at several atmospheric levels.

Table 2.1: Observation types with average counts and errors for each (in a 28-day period)

Type	# available (28-day period)	Average σ_o [a]
Idealized Total Column CO_2	232110	1.00 ppm
OCO-2 Total Column CO_2	11016	0.66 ppm
ACARS Horizontal Wind	7364982	3.54 ms^{-1}
ACARS Temperature	7362018	1.00 °C
ACARS U Wind Component	7492721	2.50 ms^{-1}
ACARS V Wind Component	7527163	2.50 ms^{-1}
Aircraft Horizontal Wind	1485596	4.37 ms^{-1}
Aircraft Temperature	1566633	1.12 °C
Aircraft U Wind Component	1543762	3.09 ms^{-1}
Aircraft V Wind Component	1556722	3.09 ms^{-1}
GPSRO Refractivity	1711165	0.95 [b]
Radiosonde Specific Humidity	519558	1.39 g kg^{-1}
Radiosonde Temperature	822747	0.95 °C
Radiosonde U Wind Component	830221	2.21 ms^{-1}
Radiosonde V Wind Component	835455	2.21 ms^{-1}
Satellite U Wind Component	2309786	4.66 ms^{-1}
Satellite V Wind Component	2336576	4.66 ms^{-1}

[a] i.e., the square root of the observation error variance, averaged globally.
[b] GPSRO (fractional refractivity) is unitless.

The realistic super-obs use the averaging kernel ($\mathbf{a}$), and auxiliary variables such as c_{prior} from the actual OCO-2 observations, summarized over 10-second periods as described in 2.2.4. The modeled XCO_2 (y_{model}) is calculated as:

$$y_{model} = y_{prior} + \mathbf{a}(10^6 \cdot \frac{\mu_{dryair}}{\mu_{CO_2}} \cdot c_{model} - c_{prior}) \tag{2.38}$$

Here, c_{prior} is the prior CO_2 profile used by the OCO-2 retrieval algorithm. This profile is on a different vertical grid than CAM's CO_2 profile, c_{model}. So, in addition to being interpolated in the horizontal to the location of the OCO-2 sounding, the model's CO_2 is interpolated from the model vertical grid to that of the OCO-2 profile. Oftentimes, the lowest level or two in the OCO-2 profile is lower than the bottom level of the CAM profile. In this case, c_{model} at that level is set to be equal to c_{prior} of that level. y_{prior} is the prior XCO_2 used by the retrieval algorithm. $\mathbf{a}$ is the averaging kernel for the particular super-ob.

2.2.6 CO_2 surface flux forcing

The model CESM-CAM5.0FV is forced at the surface by the fluxes calculated by the CarbonTracker 2015 (CT2015, https://www.esrl.noaa.gov/gmd/ccgg/carbontracker/CT2015/) system (Peters et al. 2007), regridded from CarbonTracker's 1° x 1° grid to CESM's 1.9° x 2.5° grid. The forcing for the natural land carbon flux ("SFCO2_LND" in CESM) is the sum of CarbonTracker's "bio" (terrestrial biosphere) and "fire" (fire emissions) fluxes.

The fossil fuel surface forcing differs between the "true" and "false" model runs in our OSSEs. The true run's fossil fuel CO_2 tracer is forced with the fossil fuel emissions used by CT2015. The "false" run is forced with these emissions to which a bias of -50% is imposed over China. The imposed bias is shown in Figure 2.5.

In each OSSE, the C_{fossil} tracer is forced with an ensemble of emissions whose mean is centered around the CT2015 FF emissions, and whose spread, representing a realistic uncertainty in those forcings, is created using Evensen's method for creating pseudorandom fields (Evensen (2003), Appendix E). In creating these fields, we use a decorrelation length scale of 400 km, a value similar to others used in the literature for the fossil fuel emission field (e.g. Basu et al. (2013)). The method creates fields with zero mean and unitary variance. We scale the fields so that their global standard deviation is close to the error reported by the Global Carbon Project for the fossil fuel fraction (Le Quéré et al. 2016). The spread in the emissions field of the 30 ensemble members is shown in Figure 2.5 alongside the ensemble mean.

This OSSE is our first attempt to assess the ability this DA system, along with satellite CO_2 observations, to detect bias in reported FF emissions, given uncertainties in the observations and in atmospheric advection and mixing. To set up the "best case" scenario, we do not include any uncertainties to the CT2015 land and ocean fluxes, even as we recognize that uncertainties in the land fluxes especially are greater than those in the FF fluxes.

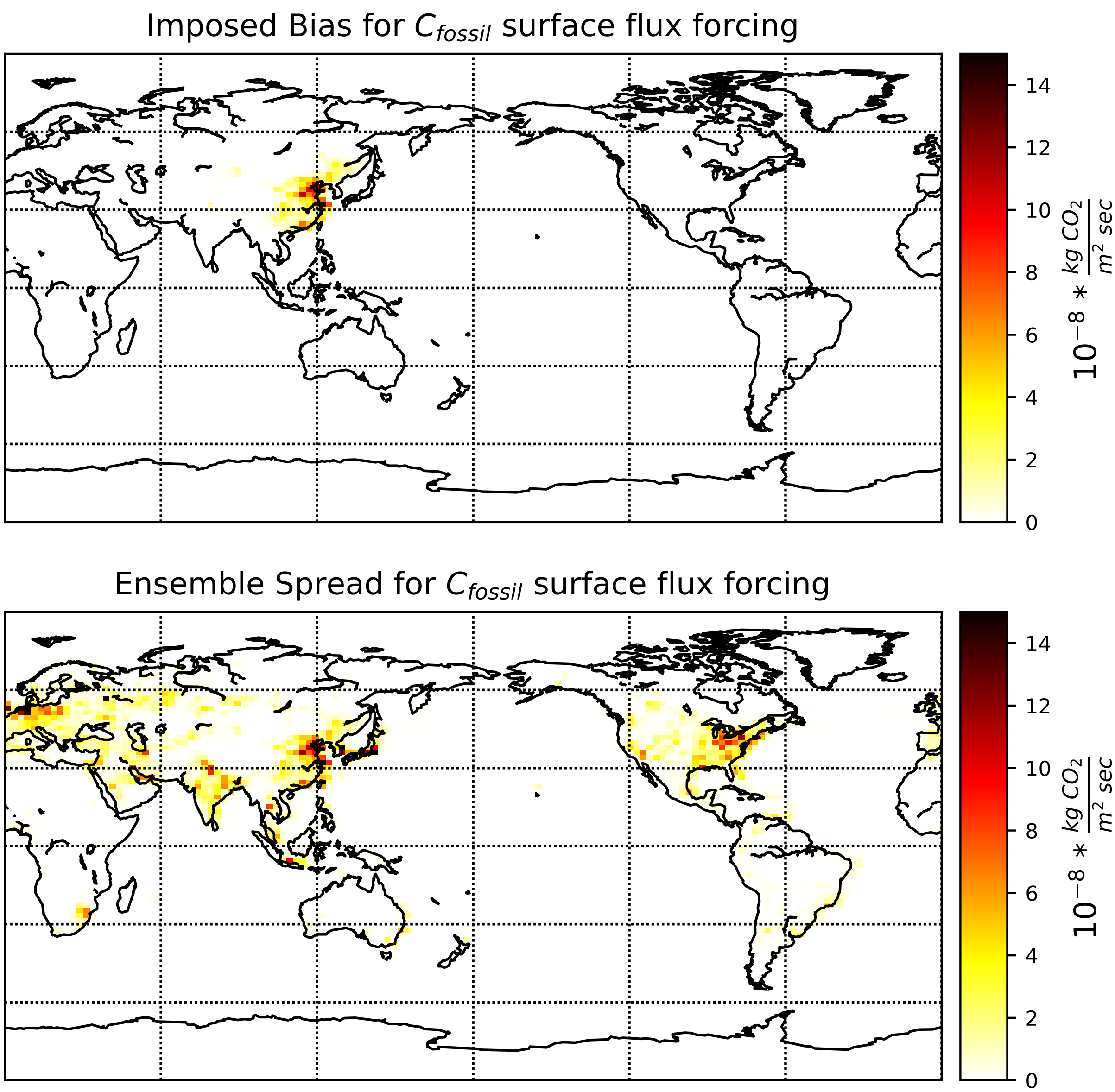

Figure 2.5: Imposed bias in fossil fuel CO_2 emissions for the false ensemble mean, in 10^{-8} x $kgCO_2/m^2/sec$ (upper panel). Ensemble spread in the fossil emissions, also in 10^{-8} x $kgCO_2/m^2/sec$ (lower panel).

2.2.7 Initial Conditions and Initial Ensembles

The single realization of the "truth" run provides the fields from which observations are sampled, and against which the analysis results are compared. The "truth" run starts from a single initial CO_2 and meteorological state for a 3-year integration of CAM5. The meteorological initial conditions are the mean fields from January 2010 of the 2000-2010 DART/CAM reanalysis described in Raeder et al. (2012). For CO_2, the 3D fields used as initial conditions in Liu et al. (2012) (i.e., from 0000 UT on 1 January 2003) are interpolated from the CAM3.5 3D grid onto the CAM5 3D grid. The CO_2 fields in this integration of CAM5 are forced at the surface with emissions from CT2015 (with emissions from land, fires, ocean, and fossil fuels). At the end of three years, the interhemispheric CO_2 gradient is stable from month to month.

In addition to the initial condition for the three year spin-up, there are two steps in the DA experiments and hence two more sets of conditions which could be referred to as "initial conditions" in these experiments. First, there is the single initial state which is perturbed to start the spin-up integration, thus generating a "spun-up" ensemble of states. The spun-up ensemble of states are then initial conditions for the experiment, when the bias in fossil fuel emissions is imposed. We will refer to the single initial state as the initial conditions, and the spun-up initial ensemble for the various experiments as the initial ensembles.

The spin-up period for our experiments starts on October 8 2015. To create the initial conditions for the spin-up, we start with the atmospheric state on October 14 of the final year of the "truth" run, so that the initial conditions are slightly different from the data to be assimilated. This atmospheric state is replicated to create an ensemble with 30 members. To each ensemble member a different random perturbation (sampled from a normal distribution with a standard deviation of 0.1°C) is added to the temperature field, just for the first six-hour model integration of the 30 ensemble members. This perturbation propagates to the other state vector fields as observations are assimilated and as the integration moves forward in time. The ensemble is forced with the same land and ocean CO_2 fluxes used in the "truth" run, and its fossil fuel CO_2 uses an ensemble of forcings whose mean is the same as the fossil fuel forcing from the "truth" run. The formation of this FF flux ensemble is described in more detail in section 2.2.6.

During the spin-up, we start to assimilate XCO_2 and meteorological observations from the "truth" run into the ensemble. Figure 2.6 shows the behavior of the ensemble for a few observation types for the OCO-2 sampling strategy and *Ideal* observational strategy. After ∼six days for meteorological observations (and slightly longer for XCO_2 in the *Ideal* case), we have an ensemble of atmospheric states with enough spread to ingest most of the observations fed to it. We note that the spread in the C_{fossil} and C_{total} tracer distributions are influenced both by the spread in CO_2 FF surface flux forcing and by the propagation of the initial temperature perturbations. The behavior of the system in observations space is further discussed in section 2.2.8.

2.2.8 Observation space diagnostics of the spin-up

To gauge the health of the spin-up, we examine three diagnostic quantities in observation space: the "total spread," the root-mean-square error (RMSE), and the number of observations assimilated.

The total spread is the square root of the sum of the ensemble variance (either $(\sigma_m^f)^2$ or $(\sigma_m^a)^2$) and the observation error variance (σ_o^2), for the available observations in a given region and assimilation window. The ensemble variance provides an estimate of (prior or posterior) model uncertainty, while the observation error variance is the uncertainty in the observation.

RMSE is the root-mean-squared difference between observed values y_o (from the truth run) and the ensemble mean model-derived observation (y_m), again for the available observations in a given region and assimilation window. It can be calculated using y_m from the forecasts or the analyses. A healthy assimilation will give RMSE values that are similar to the total spread. The number of available observations which are actually assimilated into the system increases when the magnitude of the ensemble variance relative to the observation error variance increases. A smoothly operating assimilation will ingest most of the available observations, but may reject a few that exceed the outlier threshold.

Each of these diagnostic quantities is visualized in Figure 2.6 for the duration of our two distinct ensemble spin-ups (for the *October/November* experiments and for the *Ideal* experiment), for both weather and XCO_2 observation types, using the simulated observations available in the Northern Hemisphere. The weather observation types shown correspond to locations of radiosonde measurements of westerly wind at 850 hPa, and aircraft-based measurements of temperature at 700 hPa, while the XCO_2 observation types correspond to either OCO-2 super-obs (*October/November* spin-up) or idealized, global daily coverage XCO_2 (*Ideal* spin-up).

The RMSE and total spread for the simulated weather observations show similar behavior throughout the two spin-ups, which is expected since the same weather observations are assimilated in the two experiments. For both the temperature and wind observation types, the RMSE is initially much larger than the total spread, as the initial conditions for the ensemble spin-up is deliberately chosen to be different from the observed state from the "truth" run on that day. As more observations are assimilated, the modeled values approach the true observed values, decreasing the RMSE to a value that is close to the total spread.

The rightmost bottom panel of Figure 2.6 shows the metrics for OCO-2 XCO_2 during the spin-up for the *October/November* experiments. This is a less canonical story, as immediately most of the available observations are assimilated rather than the ramping-up as is seen for the wind observations. This indicates that the available ensemble mean XCO_2 and the true XCO_2 are initially similar enough that most of the available observations are not rejected by the outlier threshold filter. The RMSE for the OCO-2 XCO_2 becomes unstable a few days into the spin-up, indicating that the spread in C_{total} has increased, with contributions from both the spread in the ensemble surface flux forcing and the spread in transport.

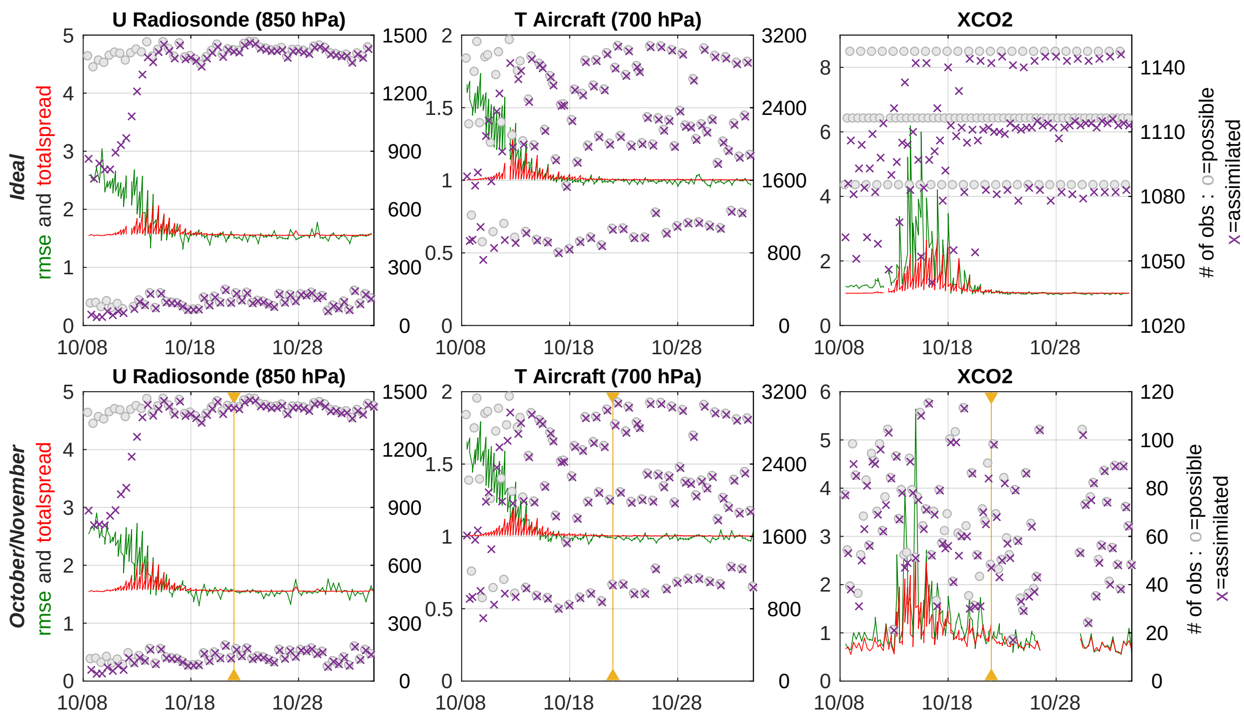

Figure 2.6: Observation space diagnostics for the ensemble spin-up period for the *Ideal* experiment (top row) and for the *October/November* experiment (bottom row), corresponding to observation types radiosonde horizontal wind at 850 hPa (left column), aircraft temperature at 700 hPa (middle column), and XCO_2 (right column). Observation statistics are aggregated across the Northern Hemisphere for each six-hour assimilation window. The diagnostics are: the total spread (red), the RMSE (green), the number of observations assimilated (purple x), and the number of possible observations (gray circles). In the bottom row, a gold vertical line indicates the end of the spin-up for the *October* experiment, while the *November* spin-up continues after this line and ends at the edge of the graphs. RMSE and spread units are ms^{-1}, °C, and ppm for wind, temperature, and XCO_2, respectively. The RMSE and total spread time series includes alternating forecast- and analysis-based values.

By 10/22, when the *October* experiment begins, the assimilation is stable compared to the earlier unstable period, but we see that it settles further as we reach the *November* experiment's start date (11/04). We note that between October 27, 2015 and October 29, 2015, the software which operates the OCO-2 instrument and spacecraft were being updated and tested, so no OCO-2 observations are available during this time. The instability at the 10/22 start of the *October* experiment is demonstrated more clearly by the snapshots of the state-space bias that are displayed in Figure 2.12 and discussed in section 2.3.3. Starting the *October* experiment before the total spread and RMSE of XCO_2 have stabilized has some consequences which we discuss in section 2.3.3.

The upper right panel of Figure 2.6 shows the metrics for the XCO_2 observations in the *Ideal* case. With much greater observational coverage, the ramping-up of the number of available observations assimilated is similar to that in the weather observation metric time series. Additionally, the RMSE for the idealized XCO_2 follows the total spread closely, as soon as 10/23, just shortly after the weather metrics have stabilized.

2.3 OSSE Results

Here we present the results from the three OSSEs. Table 2.3 summarizes the differences among the three experiments. In the *Ideal* experiment, we assimilate simulated XCO_2 from every 2.5° x 1.9° model grid box at 1pm local time each day, whereas in the *October* and *November* experiments, we assimilate simulated XCO_2 that assumes realistic OCO-2 coverage and observation strategy. All three experiments assimilate the same simulated weather observations. We reiterate that "simulated" here indicates that the observations are pulled from the truth integration's atmospheric state, at the time and location of real (or hypothetical, in the case of the *Ideal* experiment's XCO_2 only) observations. We define the start of each experiment as the time after the ensemble is spun-up, when we impose the biased FF emissions.

2.3.1 State Space Diagnostics

To test the effectiveness of our DA system, we examine whether the ensemble members bracket the true state, both in places with unbiased emissions (e.g. Los Angles, Figure 2.7) and in the region of imposed bias (e.g. Beijing, Figure 2.8).

For Los Angeles, a city removed but downwind of our imposed bias, the ensemble of near-surface CO_2 tracks the truth well in all 3 experiments (Figure 2.7). In the middle panel of this figure, we see that in the *October* experiment, the ensemble mean CO_2 starts out at a significantly lower concentration than the true concentration. This is another indication that the ensemble needed to spin-up for a few more days.

Figure 2.8 shows the time series of near-surface CO_2 for the grid box that contains Beijing. We find that here, where biased emissions are imposed, the ensemble mean in all three experiments generally underestimates the true atmospheric state. This underestimation is

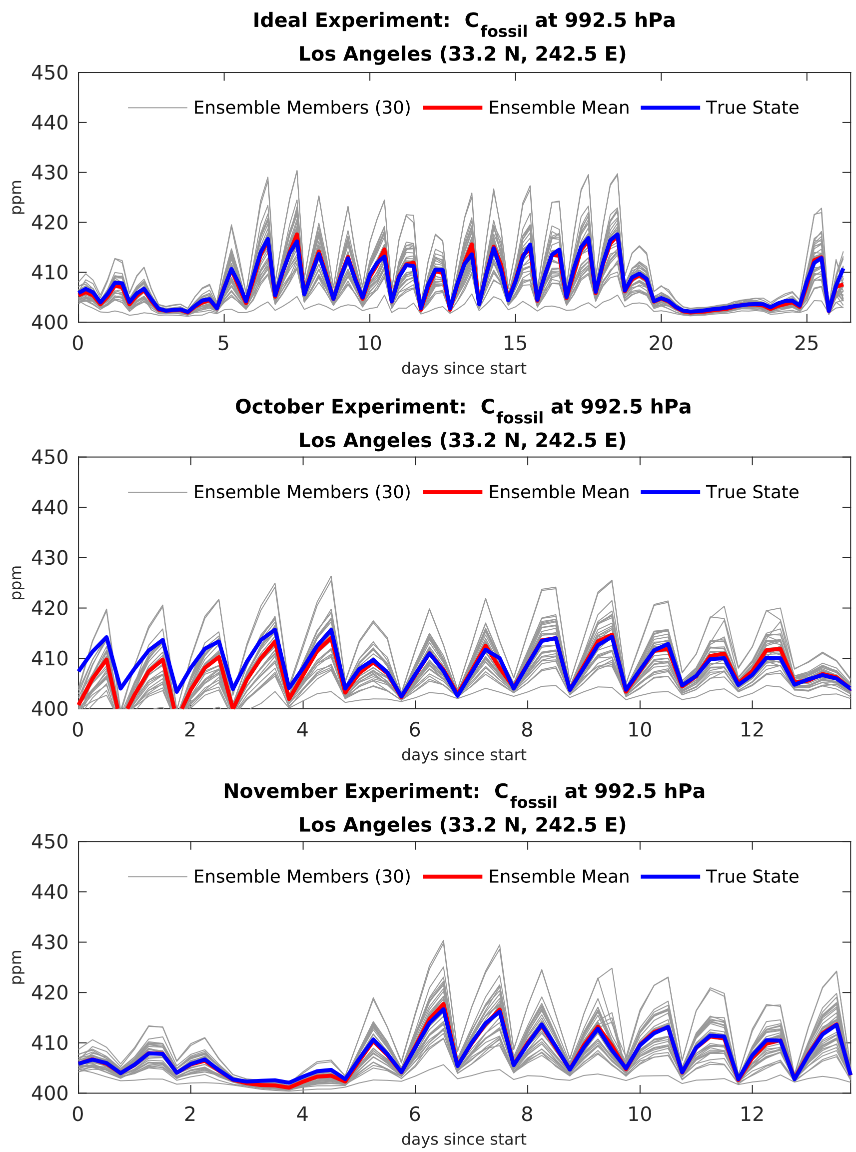

Figure 2.7: Time evolution of C_{fossil} in the bottom model level (∼992 hPa) for the grid box containing Los Angeles. Ensemble members (gray), ensemble mean (red), and true state (blue) are shown for the *Ideal* (top panel), *October* (middle panel), and *November* (bottom panel) experiments, starting at the time at which low-biased fossil fuel emissions are imposed over China.

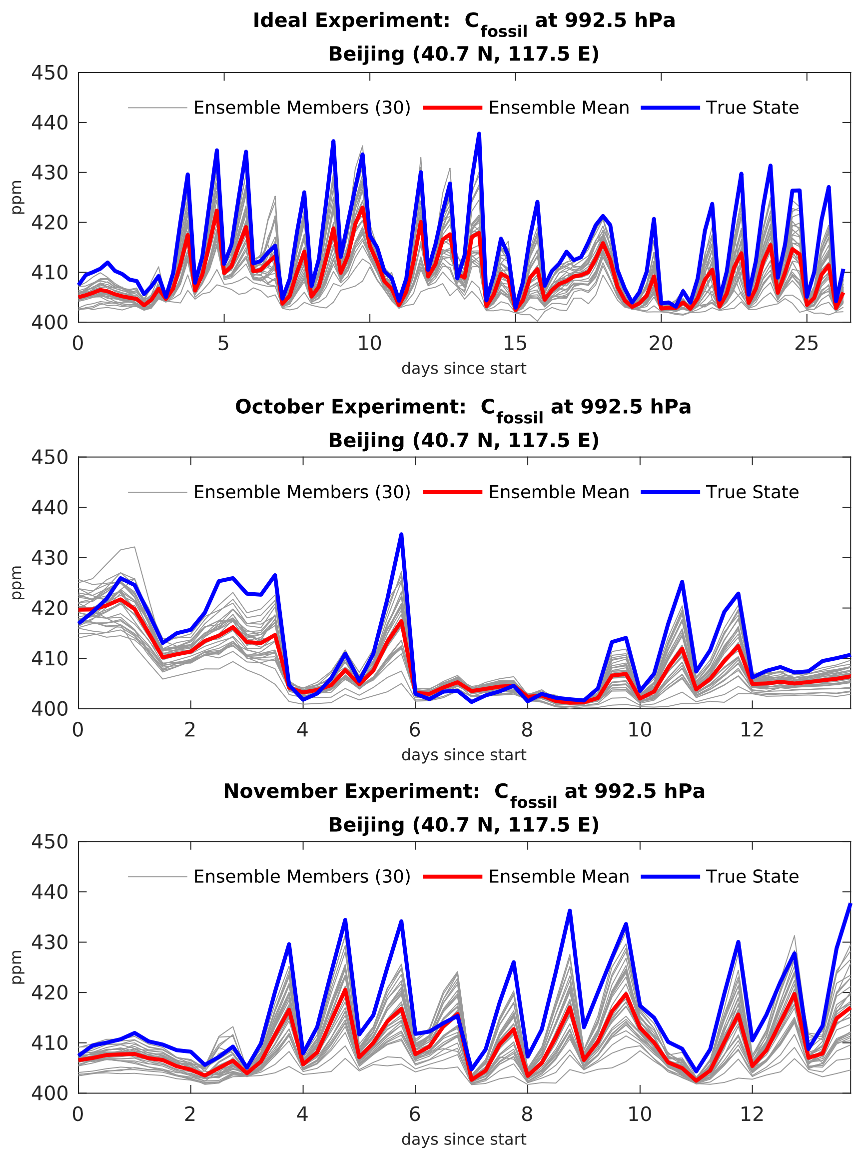

Figure 2.8: Time evolution of C_{fossil} in the bottom model level (~992 hPa) for the grid box containing Beijing. Ensemble members (gray), ensemble mean (red), and true state (blue) are shown for the *Ideal* (top panel), *October* (middle panel), and *November* (bottom panel) experiments, starting at the time at which low-biased fossil fuel emissions are imposed over China.

Table 2.2: Description of Data Assimilation experiments.

Run Name	Spin-up[a] Duration	Start[b]	End	Averaging Kernel	XCO_2 Coverage
October	14 days	10-22	11-07	OCO-2-like	Realistic[c]
November	28 days	11-04	11-18	OCO-2-like	Realistic
Ideal	28 days	11-04	11-30	Pure Pressure Weighted	Idealized[d]

Note. — [a]The spin-ups are initialized with the same ensemble of atmospheric states of October 8. During the spin-up, "true" FF fluxes are used as forcing and the full suite of simulated observations, including XCO_2 and weather observations, are assimilated. [b]The start and end date listed here denote the boundaries of the period during which false FF fluxes are used as forcing. In the text, this period when false emissions are imposed is referred to as the "experiment" period. [c]"Realistic" XCO_2 coverage here indicates that observations are sampled according to the locations of actual good quality OCO-2 soundings, aggregated to 10-second super-observations. [d]"Idealized" XCO_2 coverage indicates that XCO_2 is sampled at every 1.9° x 2.5° model grid box at 13:00 local time every day.

especially pronounced when the near-surface CO_2 is at its maximum: at nighttime when the boundary layer is shallow and when there are no XCO_2 observations. These factors combine to give the poor nighttime estimation of near-surface CO_2 concentrations over the biased region.

Of the three experiments, the *Ideal* experiment performs best in terms of the ensemble mean and spread approaching the true atmospheric state. In this case, when we have the most observations, around midday when the boundary layer is at its maximum extent, the ensemble mean tracks the truth almost perfectly.

2.3.2 Cumulative Innovation in CO_2 Mass

In all three experiments, we find positive $\Sigma_{\Delta\overline{\Phi}}$ (cumulative innovation in CO_2 mass, *cf* Equation 2.18), over the region of imposed bias. The *Ideal* experiment gives the clearest, strongest signal in innovation, indicating that observation coverage is key to detecting the biased emission signal.

There is an optimal amount of the atmosphere that should be included when calculating $\Sigma_{\Delta\overline{\Phi}}$, as is indicated by Figure 2.9, which shows the percent bias retrieved as a function of the amount of atmosphere included in the calculation. The percent of the bias detected increases rapidly as we add more of the atmosphere up to ~900 hPa. The percent then flattens out after about 650 hPa. At 525 hPa, the experiment recovers 54.6 +/- 3.8 % of the imposed bias. After 525 hPa, including more levels does not add more than 0.1% to the percent retrieved, but the uncertainty in the percent retrieved continues to increase. Thus,

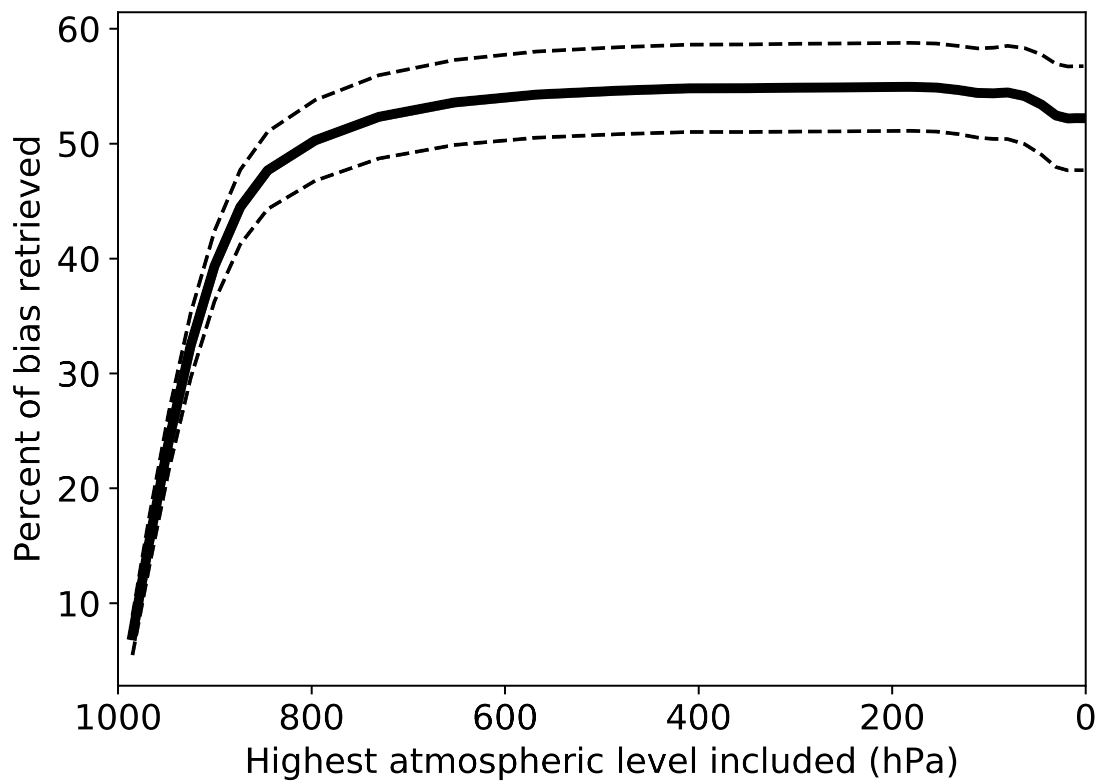

Figure 2.9: For the *Ideal* experiment, the percent of the time-summed imposed bias detected by the observing system, as a function of the amount of the atmospheric column included in calculating the cumulative innovation in C_{fossil} mass ($\Sigma_{\Delta\overline{\Phi}}$). The solid line is the percent retrieved and the dashed lines are the spread in that percent.

Figure 2.10 shows the innovation up to 525 hPa rather than for the full column or for the near-surface atmosphere alone. We suspect that we detect only about half of the imposed bias because of the lack of nighttime observations to update the CO_2 state throughout the night.

The cumulative flux innovation, $\Sigma_{\Delta\overline{\Phi}}$, for the *Ideal* experiment (up to 525 hPa), along with its spread, is shown in Figure 2.10 in the middle panels. Here $\Sigma_{\Delta\overline{\Phi}}$ is time-averaged for a quantitative comparison with the imposed bias in surface flux forcing, which is shown in the top panel. We see that the grid boxes where we find large positive $\Sigma_{\Delta\overline{\Phi}}$ correspond overwhelmingly with the grid boxes with large imposed emissions biases. In the bottom panel of this figure, we show $\Sigma_{\Delta\overline{\Phi}}$ aggregated over six regions. The regions correspond in latitudinal extent to the latitudinal boundaries of China (18°N to 53°N), and in longitude they constitute 60-degree bands, with the 75°E-135°E closely approximating the width of

China.

The cumulative flux innovation results for the *October* and *November* experiments are shown in Figure 2.11. The third row in this figure shows that, when aggregated to 60-degree longitude bins, positive innovation is present over the region that includes China (75°E-135°E) in both experiments.

As is expected from the relative sparsity of observations, the innovation in the *October* experiment is smaller than the innovation in the *Ideal* experiment (by a factor of 3). Additionally, there are false signals in several regions where the innovation is of comparable magnitude to the China signal. Most notably, off the east coast of the United States there is a significant positive innovation signal, and in the mid-Pacific between 25°N and 55°N there is positive innovation surrounded by some negative innovation patches. Both of these overlap with regions of large atmospheric instability (storminess), as indicated by their corresponding spreads in surface pressure (bottom row of Figure 2.11). In the *October* case, they also correspond to the imperfect/unstable conditions at the end of the spin-up before the imposition of the biased emissions, as we discuss further in section 2.3.3. As seen in the state space diagnostics and observation space diagnostics, the ensemble spread was still large and the ensemble mean CO_2 differed significantly from the true state in many areas at the start of the *October* experiment.

In the *November* experiment, the ensemble spread at the end of the longer spin-up period is smaller than that in the *October* experiment. The most dominant signal in CO_2 innovation is over the biased region, without significant false positive innovations over the Pacific and Atlantic oceans or elsewhere. However, this signal is even weaker compared to the *October* experiment and to the imposed bias. We hypothesize that this is due to the sparser observation coverage in November as compared to October, in the Northern Hemisphere winter and especially over China (Figure 2.3).

2.3.3 Contributions to weak innovation signals in October and November experiments

Observation Coverage

Dense observation coverage of CO_2 is clearly key to the ability to detect and estimate biased fossil fuel emissions in our DA system. Our most successful experiment also has the densest and most comprehensive observation coverage of the three experiments. We detect a much weaker signal related to the biased emissions in the *November* experiment as compared to the *October* experiment, which we hypothesize is mostly due to sparser observation coverage, especially over China, in the *November* experiment. Maps of the respective observation counts are seen in Figure 2.3. Since OCO-2 measures reflected sunlight, its coverage suffers in high northern latitudes in boreal winter.

In the *Ideal* experiment with daily global coverage (at 1PM local time), there is still no nighttime coverage, and thus no updating of the CO_2 fields overnight. Hence, in this current setup, it is unavoidable that emission bias is underestimated in the OSSE.

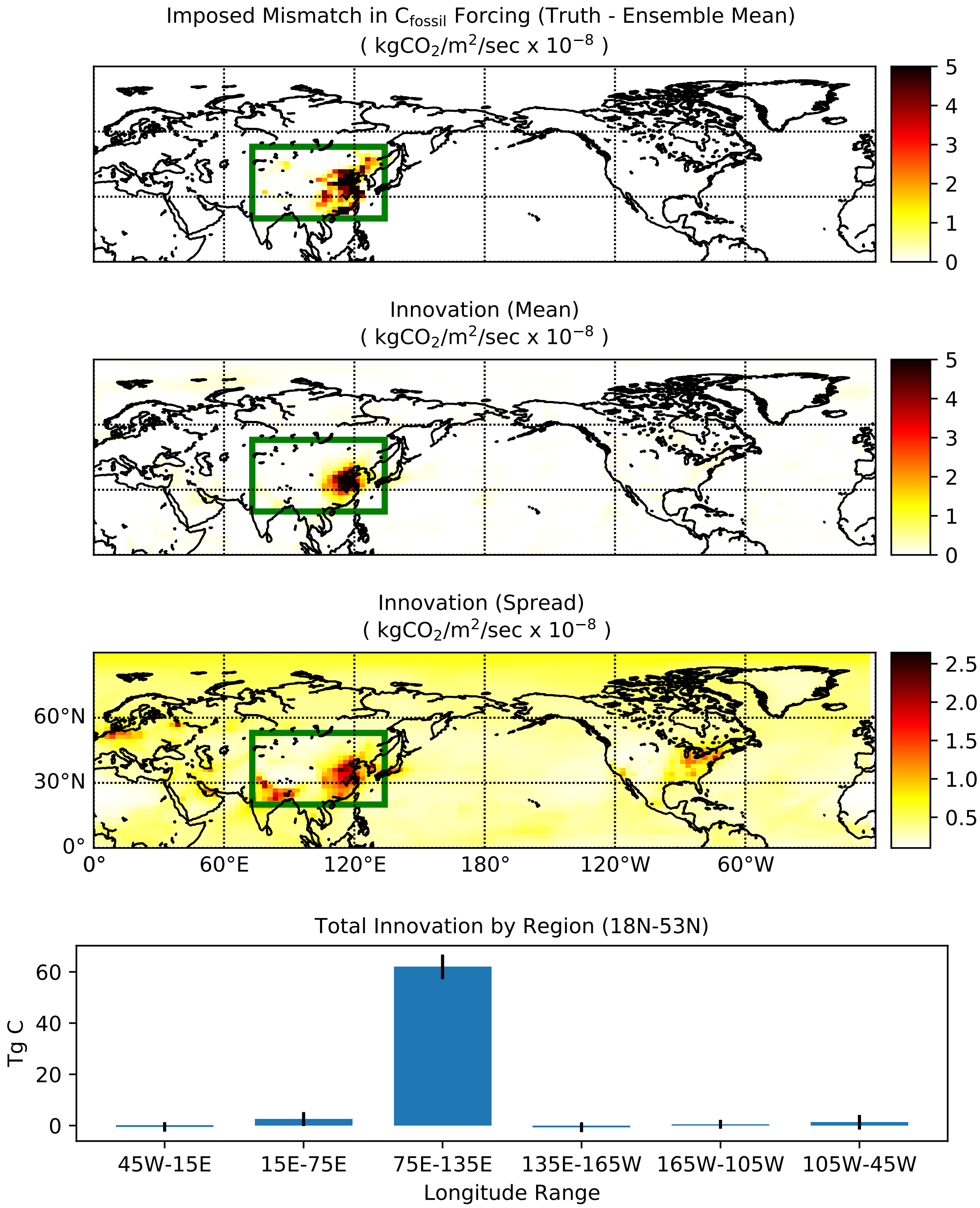

Figure 2.10: The average imposed bias [Truth - Ensemble Mean] in C_{fossil} forcing (topmost panel) for the time period spanning the *Ideal* experiment. The mean (second panel) and spread (third panel) in the cumulative flux innovation ($\Sigma_{\Delta\overline{\Phi}}$) up to 525 hPa in the *Ideal* experiment, time-averaged for an equal comparison with the imposed bias. $\Sigma_{\Delta\overline{\Phi}}$ aggregated across 60° longitude groups (lower panel). Each group includes latitudinal range 18°N-53°N, the range of China.

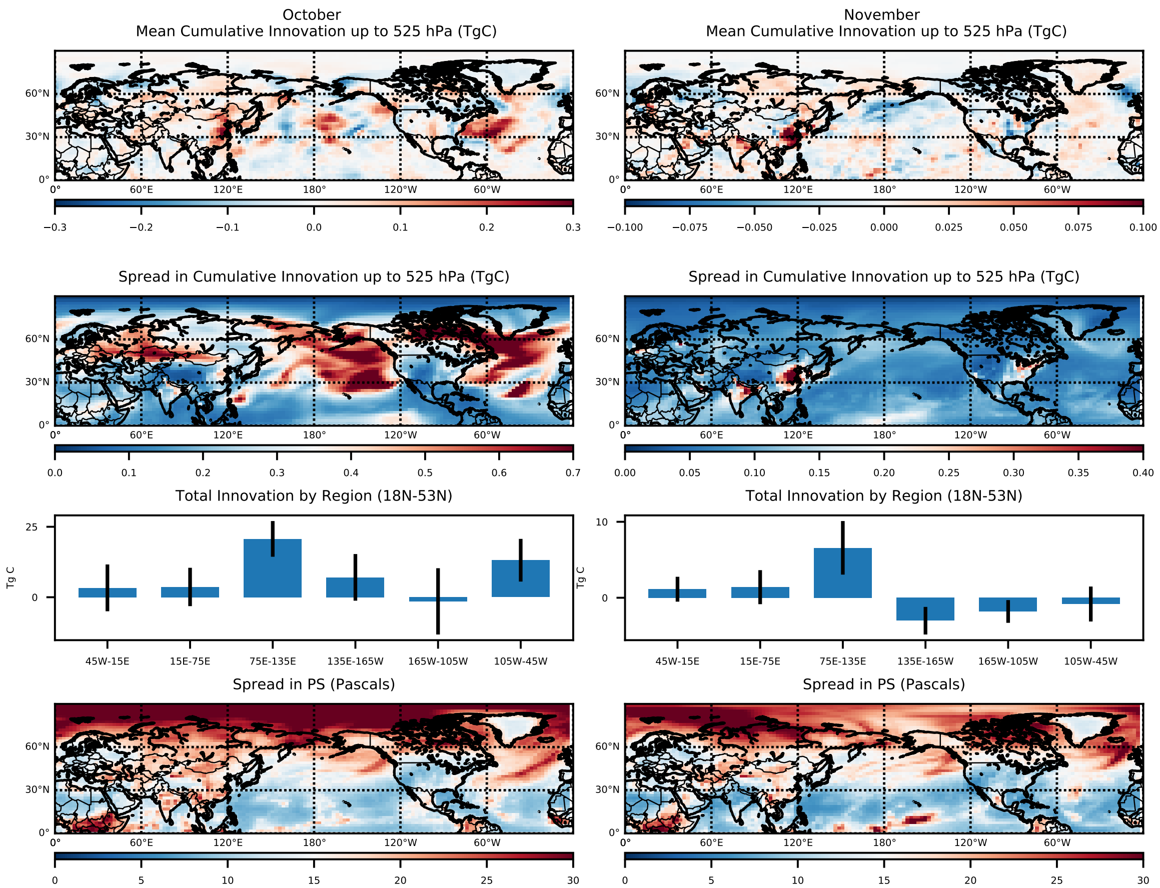

Figure 2.11: For the *October* (left column) and *November* (right column) experiments, Mean (top row) and Spread (second row) in the cumulative flux innovation ($\Sigma_{\Delta\overline{\Phi}}$) up to 525 hPa, in Tg C. $\Sigma_{\Delta\overline{\Phi}}$ aggregated across 60° longitude groups, in Tg C (third row), with 1-σ error bars. Average ensemble spread in the surface pressure for the same time period (bottom row), in Pascals. The six regions in the bar graphs in the third row are limited in their latitude by the northern and southern boundaries of China (18°N-53°N) in addition to being limited in their longitude by the indicated boundaries. In the top two rows, $\Sigma_{\Delta\overline{\Phi}}$ has been multiplied by the area of each grid box.

Initial Ensembles

An initial ensemble which was not fully spun-up at the time of the imposition of the false emissions likely contributed to the false positives in innovation seen in the *October* experiment. The spin-up periods for the *October* and *November* experiments began from the same initial state (October 8), but differ in the length of the spin-up period.

Figure 2.12 shows the difference between the true CO_2 and the ensemble mean CO_2 at the end of the spin-up and the start of each DA experiment. At the start of the *October* experiment, there are regions where the ensemble mean state is very different from the true state. It is clear in Figure 2.12 that false positive signals in the *October* experiment in the Gulf Stream region and in the Pacific coincide with places where the initial ensemble is biased low compared to the true state (especially in the 993 hPa and 860 hPa levels). With a longer ensemble spin-up for the *November* case, these large biases are removed as the ensemble has further equilibrated around the true state.

Correlations with meteorological variables

Some of the false signals in our experiments could also be due to our variable localization scheme. In Liu et al. (2011), weather observations did not directly impact CO_2 fields, but they indirectly updated CO_2 through transport (i.e., wind fields u and v are updated via weather observations and these updates propagate through transport as expressed by the continuity equation). In this work, the CO_2 fields are impacted in this way, but they are additionally directly impacted by the weather observations. Kang et al. (2011) found that, in terms of constraining surface fluxes, having u and v observations directly influence CO_2 concentrations in the model state slightly outperformed the case where CO_2 was only impacted indirectly as in Liu et al. (2011).

In our setup however, we employ a variable localization scheme like the “L-mult” scheme in Kang et al. (2011), where all meteorological state variables can statistically impact the CO_2 tracers and vice versa. In Kang et al. (2011), the “L-mult” scheme performed more poorly than those where only winds (u and v) impacted CO_2 but temperature, specific humidity and surface pressure did not. The investigation of a variable localization scheme where only some of the meteorological observations impact CO_2 is beyond the scope of this study. We hypothesize that the effect of different variable localization schemes would be more pronounced in the *October* and *November* experiments, since weather observations have greater impact on the CO_2 analyses when there are more abundant lapses in XCO_2 coverage.

2.4 Discussion and Conclusions

This study presents an OSSE that assesses the feasibility of a mass-balance approach for anthropogenic trace-gas emissions validation and bias detection in the presence of meteorological uncertainties. The carbon-weather data assimilation system forecasts CO_2 and

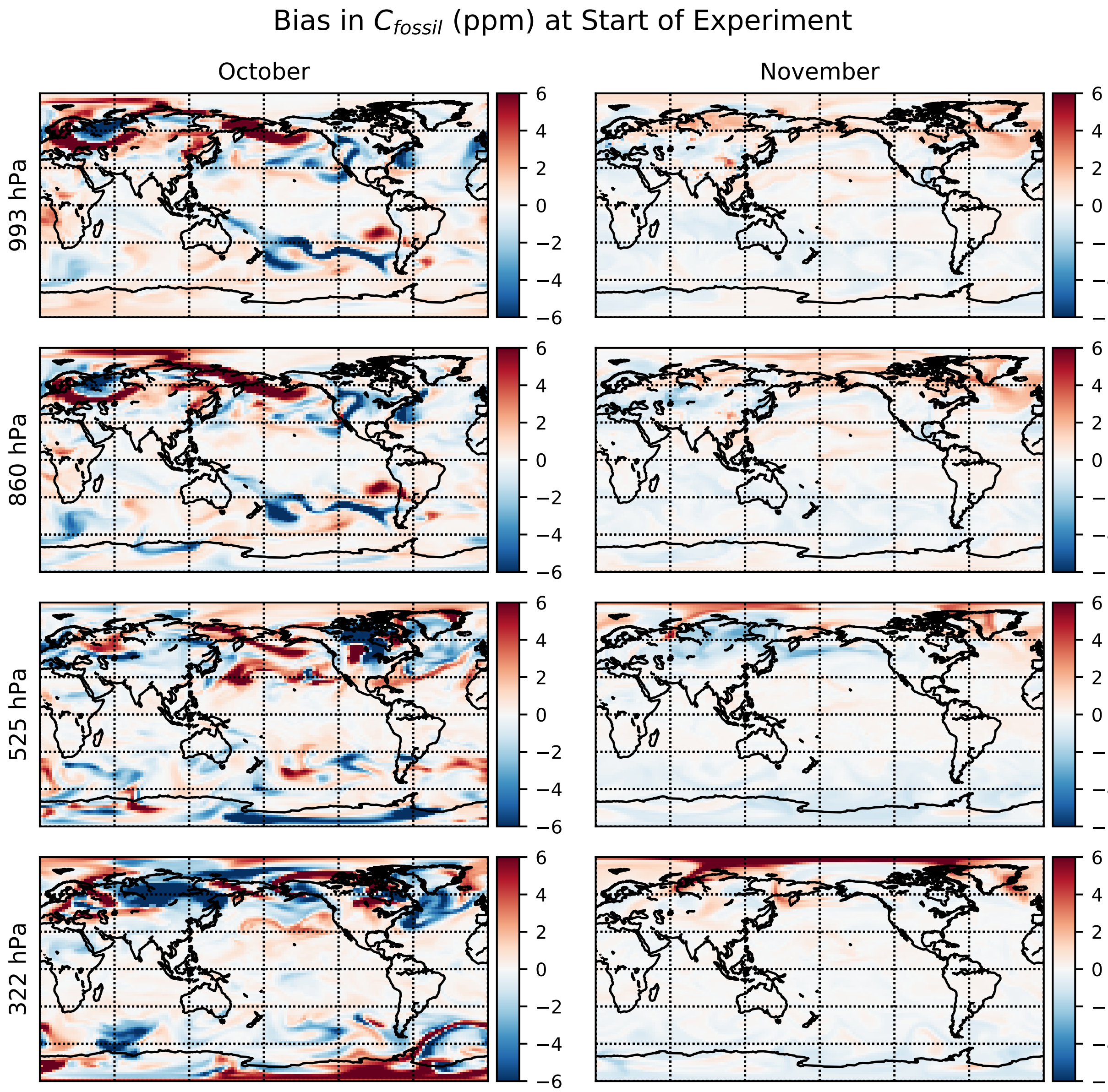

Figure 2.12: [Ensemble Mean C_{fossil} - True C_{fossil}] in the initial condition for the *October* (left panel) and *November* (right panel) DA experiments, for 4 different pressure levels. Units are ppm.

weather using the NCAR carbon-climate model CAM5.0 every six hours, and the EAKF in DART determines the "analysis", i.e. optimal fit between the forecast and the CO_2 and meteorological observations within the six-hour assimilation window. The observations are taken from a "truth" run, with CAM5.0 forced by surface CO_2 fluxes from CarbonTracker. The DA system generates both the mean and spread in CO_2 and meteorological analyses.

In three experiments, fossil fuel emissions from China were biased low by 50%. The cumulative CO_2 flux mismatch is approximated by the innovation in the CO_2 mass, i.e. the additional CO_2 required to match the XCO_2 observations. In this prototype study of a "best case scenario", we have assumed known land and ocean sinks. China was chosen as the focus study area because of its large size and because uncertainties in its emissions have been the subject of multiple studies. The 50% bias is unrealistically large, and was chosen in this first study to explore the DA methodology and the observing strategy necessary to detect such a large signal given the noise from inherent meteorological uncertainties.

The results demonstrate the potential of the DA system, with column CO_2 mixing ratios, such as from OCO-2, to qualitatively detect and attribute the imposed bias in the experiment. However, OCO-2 overpass provides daytime observations at any location only every 16 days, and it takes 8 days for the majority of 2° x 2° model grid boxes to be observed. OCO-2 also lacks observations during low sun conditions. As a result, estimates of flux biases are about 1/6 the imposed bias in the *October* experiment, with uncertainties that are comparable to the retrieved signal. The estimates are even lower in the $November$ experiment because of less dense observation coverage over the biased region.

Results from the $Ideal$ experiment show that a CO_2 observing strategy that samples globally on a daily basis, for example in a similar way to the TROPOMI instrument or with a constellation of several OCO-2-like instruments, and that provides high-latitude observations during boreal autumn and winter, would improve retrieval of the flux bias. Nonetheless, the flux bias retrieval in this idealized case is only half (55 ± 4 %) of the imposed emission bias.

Figure 2.13 shows that the low bias in the near-surface C_{fossil} analysis field in Beijing in the $Ideal$ experiment is minimized in the early afternoon, when there are observations of XCO_2, but it increases throughout the late afternoon and evening. Observations throughout all of the daylight hours, such as would be available from a carbon observatory aboard a geostationary satellite (e.g. GEOCARB), would help to constrain the CO_2 during the morning and evening. Such a satellite, combined with an observing system like our idealized system, and an active lidar instrument that observes column or near-surface CO_2 at night, could provide the critical data to constrain the magnitudes of CO_2 emissions with much greater accuracy in the particular DA system and setup described here. If we were to use a fixed lag smoother which allows our daytime observations to impact the state of the previous night, we could potentially detect more of the nighttime bias without introducing nighttime observations. However, this approach would require us to rely more heavily on models for diurnal variations in CO_2. Ideally, we would have enough observations to directly constrain CO_2 during both the day and night, and we could retain the current approach.

Improvements in emission detection also require advances in the DA methodology. This OSSE assumes a perfect model. In the spin-up period when the weather pseudo-observations

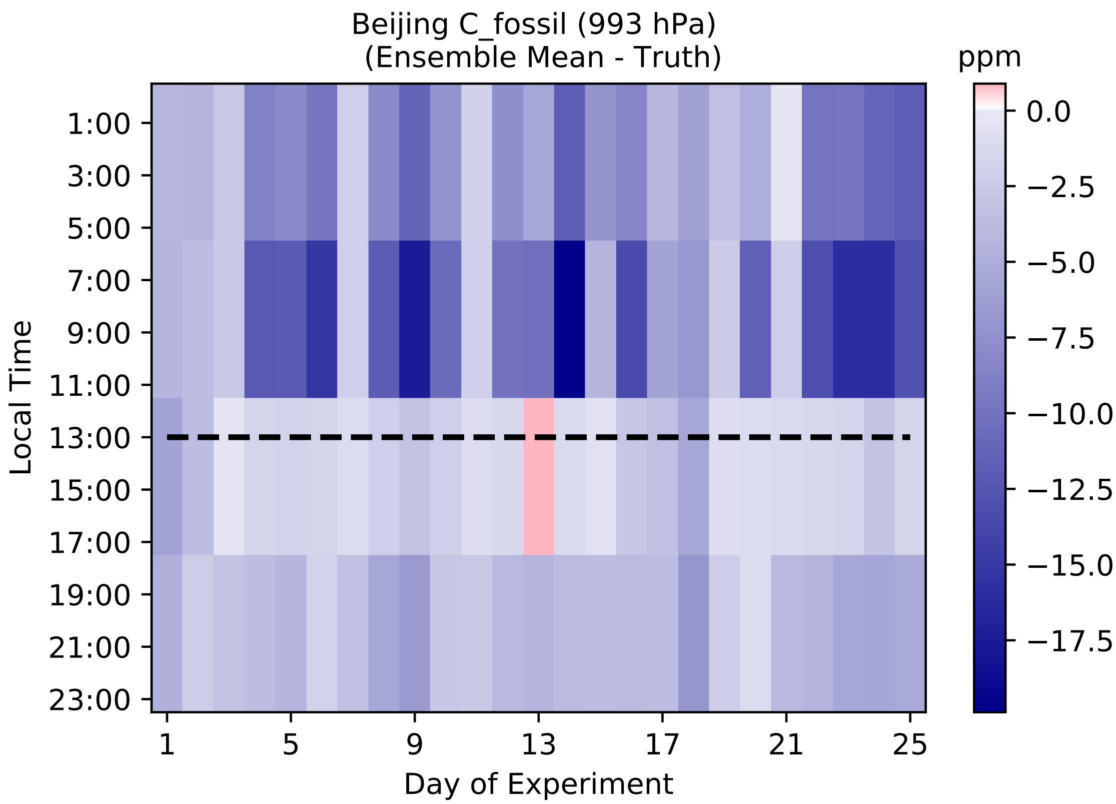

Figure 2.13: Bias in C_{fossil} (analysis) at 993 hPa (i.e. Ensemble Mean C_{fossil} - True C_{fossil}) for the grid box containing Beijing, for the *Ideal* experiment. The horizontal axis shows each day of the experiment, starting at the point at which we introduce low-biased emissions over China. The vertical axis represents the local time of day (for Beijing, UTC - 8 hours) for each of the days. Color is the bias in ppm.

are sampled from the "truth" run, there are still discrepancies between the mean analyzed circulation fields and the "true" atmospheric state. These discrepancies stem from uncertainties assigned to the pseudo-observations, incomplete observational coverage, and inherent nonlinearities in the circulation, especially those associated with convective mixing and transport. In turn, they contribute to errors in the spin-up CO_2 fields even when the ensemble mean of the CO_2 forcings is prescribed to be true. Hence these errors in both CO_2 and circulation fields at the end of the spin-ups, such as for the *October* experiment, propagate onto the ensuing data assimilation integration and result in emission innovations that are artifacts of the spun-up state.

Here, we are able to assess the error in circulation and CO_2 fields at the end of the spin-up because "truth" is generated from a single integration of the carbon-weather model forced by "known" surface CO_2 fluxes. In a real application, we do not know the true state of the atmosphere. However, as emission detection would not likely be done in real time, the success of the daily weather forecast during spin-up could be ascertained and the DA experiments could be started when RMSEs of the meteorological forecasts are at a minimum. Also, new research could explore a long observation window that includes "future" observations in the estimation of the current state as proposed by Liu et al. (2017c) (which would require an ensemble smoother).

The ability to quantify meteorological uncertainties in flux estimation is a major advantage of the CAM-DART system which assimilates simultaneously weather observations together with the CO_2 observations. As winds, specific humidity, and surface pressure directly impact the advection and mixing of CO_2 as well as the estimation of column-integrated CO_2 mass, the simultaneous assimilation propagates unavoidable uncertainties in the weather variables to the CO_2 field, thus permitting the attribution of uncertainties in CO_2 analysis and inferred fluxes to transport uncertainties. As would be expected from numerical weather prediction, convective storms are associated with large spreads in surface pressure. Our results show that when storm tracks traverse high emission areas, large spreads in atmospheric CO_2 follow.

Emission detection in our DA system could be improved if we were to include additional tracer variables, such as C-13, C-14, carbon monoxide and solar-induced fluorescence, which would add constraints on terrestrial sources and sinks at continental and global scales (e.g. van der Velde et al. (2018)). Additionally, the emission hotspots derived from OCO-2 observations by Hakkarainen et al. (2016) could potentially be used in high-resolution regional carbon-weather data assimilation models to infer FF emission magnitudes.

Chapter 3

Can OCO-2 observations improve weather forecasts?

Abstract. In this chapter we explore whether observations from the Orbiting Carbon Observatory 2 (OCO-2) can improve the forecasting capabilities of numerical weather prediction (NWP) models. We present results from two different observing system simulation experiments (OSSEs): the TPW experiment and the XCO_2/Met experiment. In both experiments, the "observations" are simulated observations which are pulled from a free-running integration of the Community Atmospheric Model (CAM5 FV), i.e. the "truth" run, and we use the Ensemble Adjustment Kalman Filter (EAKF) from the Data Assimilation Research Testbed (DART) to optimally fuse these observations with an ensemble of model forecasts from CAM5. In the TPW experiment, we examine the potential utility of OCO-2's ancillary data product, the total precipitable water (TPW), which is estimated alongside XCO_2 by OCO-2's retrieval algorithm. We assimilate OCO-2 TPW observations and find that these observations impact all meteorological state variables, indicating that they could be useful additions to NWP machinery. In the XCO_2/Met experiment, the "Met" run serves as a control run, in which we assimilate a suite of meteorological observations into CAM5 with a prognostic carbon cycle. Then the "XCO_2" run is identical to the Met run except that in addition to weather observations we assimilate OCO-2 XCO_2 soundings. We test whether the addition of the OCO-2 XCO_2 observations improves forecasting of meteorological state variables in a significant way. To do this, we compare the root meet square error of the state variables between the two assimilation runs. We examine forecast errors at global and regional scales, and find forecast improvement especially in the southern extratropics, in all meteorological fields except humidity.

3.1 Introduction

Accurate weather forecasts are vital to society: by alerting communities of imminent severe weather, they save lives. They also provide crucial information for individuals, communities, and industries such as the agricultural and recreational industries, to plan their time and prepare for the elements. In surveying Americans regarding their perception and use of weather forecasts, Lazo et al. (2009) found that the typical adult in America checks weather forecasts 115 times per month. The authors of that study determined that the monetary benefit of weather forecasts in the United States is 31.5 billion USD annually, a return on investment of over 500% compared to the annual cost of U.S. public and private meteorology centers. Any methodological or observational improvement in forecast accuracy is hence of undeniable societal benefit.

One element which has led to significant forecast improvement since 1999 is the assimilation of satellite-based observations (Simmons and Hollingsworth 2002). Starting in 1999, raw microwave radiances from the TIROS Operational Vertical Sounder (TOVS and ATOVS), humidity retrievals from the Special Sensor Microwave Imager (SSM/I), and marine surface wind information from scatterometers on the Earth Resources Satellites (ERS), began to be assimilated by weather centers (ECMWF, the Met Office, and NCEP). These observations, and others that followed, have the most impact in the Southern Hemisphere, which is largely unconstrained by terrestrially-based observation types, and is largely covered in ocean (where, for example, ATOVS and SSM/I provide their best information).

It should be noted however that none of the satellite-based wind retrievals are direct measurements of wind speed. One method for deriving wind speed is to track clouds in successive images from a geostationary satellite such as one of the Geostationary Operational Environmental Satellite (GOES) instruments, assuming each cloud is a passive tracer (e.g. as described in Tomassini et al. (1999)). The height of the cloud motion vector is calculated by combining the infrared brightness temperature with a model forecast temperature profile. Cloud tracking is typically done in infrared images, but images in the visible spectrum can be used to track low-level cumulus clouds over oceans and water vapor bands can be used to track upper-level moisture patterns in clear sky conditions. Another method is to estimate ocean surface winds with a scatterometer. For example, the Advanced Scatterometer (ASCAT) wind product uses radar to measure backscatter to determine wind speed and direction over the ocean surface, employing the scatterometer aboard the EUMETSAT satellites. Taken together, these observations of wind provide some information but by no means provide a perfect picture of winds over the ocean. Thus, the Southern Hemisphere oceans remain an area where more observation availability could improve weather forecasts.

There is some evidence that assimilating remotely-sensed trace gas abundance observations could improve weather forecasts. Semane et al. (2009) show that assimilating ozone in a global model can improve wind forecasts via correlation between ozone and transport. In addition to constraining wind fields, assimilating ozone has been found to improve other meteorological fields. Coopmann et al. (2018) demonstrate that assimilating ozone-sensitive channels from the Infrared Atmospheric Sounding Interferometer (IASI) into a chemical transport model can simultaneously improve temperature, humidity, and ozone analyses.

The Orbiting Carbon Observatory 2 (OCO-2) is a relatively new instrument, launched in July 2014, which provides 43,000 to 79,000 high-quality, cloud-free measurements of total column CO_2 (XCO_2) each day (Eldering et al. (2017a)), many of which are over regions with otherwise sparse observational constraints such as the Southern Hemisphere oceans. Assimilating column abundances of CO_2 into a model which includes CO_2 composition in addition to standard meteorological variables could lead to weather forecast improvement, providing an added value from a satellite whose primary mission is to constrain CO_2 sources and sinks at regional scales.

In addition to providing observations of XCO_2, the OCO-2 retrieval algorithm provides an ancillary data product which estimates the total-column water vapor, i.e. the total precipitable water (TPW) in the atmospheric column (O'Dell et al. 2012). Nelson et al. (2016) found that OCO-2's reported TPW measurements compare favorably to highly accurate validation data from microwave radiometers and ground-based Global Positioning System (GPS) stations. The authors concluded that the accuracy of these OCO-2 TPW measurements was high enough that they could be a useful addition to the suite of observations ingested by NWP centers.

To probe the potential utility of OCO-2 TPW for NWP improvement beyond the findings of Nelson et al. (2016), we perform an observing system simulation experiment (OSSE), the "TPW experiment," which explores how meteorological state variables are impacted when the atmospheric state is constrained solely by OCO-2 TPW pseudo-observations. Here "pseudo-observation" indicates that the TPW observations we assimilate are derived from a free-running integration of our dynamic model which represents the "true" atmospheric state. For this experiment, we analyze how the TPW observations impact our various meteorological state variables. Methods specific to the TPW experiment are presented in section 3.2.1, with results in section 3.3.1.

In addition to the TPW experiment, we perform another OSSE which examines the potential utility of OCO-2 XCO_2 in informing NWP. This "XCO_2/Met" experiment is a twin experiment comparing two model runs. The first run is the "Met" run, which assimilates a suite of weather observations from radiosonde, surface, aircraft, and satellite instruments. The second run, the "XCO_2" run, assimilates OCO-2 XCO_2 observations in addition to these weather observations. In this experiment, our dynamic model also includes a prognostic carbon cycle so that CO_2 abundance can be part of the state vector. Again, both the meteorological and XCO_2 observations are harvested from a "truth" integration of our dynamic model. Knowing the true atmospheric state allows us to diagnose forecast errors in state space at every model grid box throughout the globe. The XCO_2/Met experiment is more complex than the TPW experiment in that its control run includes assimilation of many weather pseudo-observations so that we can test how forecast accuracy is impacted when adding a new observation type to a set of observations that is close to the typical set of observations used by NWP centers. We present methods specific to the XCO_2/Met experiment in section 3.2.2 and results in section 3.3.2.

Table 3.1: Description of model runs used for the TPW experiment and the XCO_2/Met experiment.

Run Name	Dates	OCO-2 XCO_2?	Weather?	OCO-2 TPW?	State Vector	Model Resolution
TPW	12/01–12/05	no	no	yes	$[u, v, T, Q, Ps]$	1° x 1°
XCO_2	10/22–11/07	yes	yes	no	$[u, v, T, Q, Ps, C_{total}, C_{fossil}]$	1.9° x 2.5°
Met	10/22–11/07	no	yes	no	$[u, v, T, Q, Ps, C_{total}, C_{fossil}]$	1.9° x 2.5°

Note. — The XCO_2 and Met runs are used for the XCO_2/Met twin experiment whereas the TPW run is used for the TPW experiment. Columns with headers like "OCO-2 XCO_2?" indicate whether that particular observation type is assimilated.

3.2 Methods

Several of the methods in this chapter are analogous to those outlined in Chapter 2 of this dissertation, but we will rehash them briefly here. The atmospheric model employed for all experiments in this chapter is the Community Atmospheric Model 5.0 with a finite volume dynamical core (CAM5 FV, Neale et al. (2012)) and standard climate forcings. Observations are harvested from a "truth" integration of CAM5 corresponding to the observation locations and errors of real weather observations (and, in the XCO_2 run or the TPW run, OCO-2 super-observations or thinned observations). An ensemble adjustment Kalman filter (EAKF) from the Data Assimilation Research Testbed (DART, Anderson et al. (2009)) is used to find an optimal fit between the observations and CAM5's atmospheric state.

Both experiments in this chapter use DART/CAM as described above, and they employ 30 ensemble members and an assimilation window of 6 hours. Additionally, they use the same localization function and parameters. To restrict the impact of observations in space, we apply the Gaspari-Cohn localization function to the model space increments, as described in Chapter 2. For the half-width parameter, we select 0.2 radians (∼1200 km) in the horizontal and 400 hPa in the vertical (for all observation types except for XCO_2). In addition to spatial localization, the model runs employ the same variable localization, in which all state vector components are allowed to be impacted by observations of any type.

The model run associated with the impact of OCO-2 TPW observations on weather forecasting ability is called the "TPW" run, and particulars for the corresponding experiment are described in section 3.2.1. The two runs which are performed for the XCO_2/Met experiment, which tests the impact of OCO-2 XCO_2 on weather forecast accuracy, are called "XCO_2" and "Met." The methods associated with this experiment are given in section 3.2.2.

The differences among the three runs are highlighted in Table 3.2. The three runs differ in that the TPW run only assimilates OCO-2 TPW (no other weather observations, and no XCO_2 observations), and the TPW experiment's atmospheric model is run at a higher spatial resolution than the XCO_2/Met experiment runs. Additionally, the TPW experiment does not include CO_2 tracers C_{fossil} and C_{total} in its state vector.

3.2.1 Methods Specific to the TPW Experiment

In this experiment, we use CAM5 FV with a 1° x 1° resolution. We include 30 ensemble members, and integrate the experiment for 18 6-hour time steps. Perfect TPW observations are harvested from a free-running CAM integration at the observation locations of OCO-2 corresponding to December 1-5, 2014. Observations are thinned to just one observation per model grid box, chosen randomly from the observations falling within these grid boxes.

The TPW forward operator is used to derive pseudo-observations from state variables Q and Ps. This operator integrates the mass of water in the atmospheric column and converts to units of centimeters H_2O as follows:

$$TPW = 100 * \frac{1}{g \cdot \rho_{H_2O}} \int Qdp \tag{3.1}$$

where Q is specific humidity (with units kgH_2O/kg air), p is the partial pressure of air (derived from Ps), g is the gravitational constant (9.8 m/s^2), and ρ_{H_2O} is the density of water vapor in air (1000 kg/m^3).

Observation error for the TPW pseudo-observations is derived from real uncertainties from the OCO-2 product. In the OCO-2 Level 2 standard files, TPW (in centimeters H_2O) can be calculated with:

$$TPW_{OCO} = \frac{1}{10} * \frac{\mu_{H_2O}}{\rho_{H_2O} \cdot a} * TC_{H_2O} \tag{3.2}$$

where μ_{H_2O} is the molar mass of water (18.016 g/mol), a is Avogadro's number (6.0221413 x 10^{23} molecules/mole), and TC_{H_2O} is the value called *retrieved h2o column* in the OCO-2 Level 2 standard files' *RetrievalResults* group, in units molecules H_2O/m^2. Then, the uncertainty in that field is calculated by multiplying it by a scale factor:

$$\epsilon_{TPW} = S * TPW_{OCO} \tag{3.3}$$

Here S is the field called *h2o scale factor uncert* in the OCO-2 Level 2 Standard product. In this study, we derive ϵ_{TPW} from an early version of the OCO-2 data, version 6r. In later versions of the data, analogous fields are directly provided in the daily "Lite" files (with field names *tcwv* and *tcwv uncertainty*, in units kgH_2O/m^2.)

3.2.2 Methods Specific to the XCO_2/Met Experiment

In this experiment, we test whether the addition of OCO-2 XCO_2 to a traditional suite of NWP observations has any significant effect on weather forecast accuracy. The "XCO_2" run here is identical to the "October" experiment from Chapter 2 of this dissertation. The "Met" run is identical to the XCO_2 run, except that no XCO_2 observations are assimilated. The full period of comparison between the Met and XCO_2 runs spans from October 22 2015 to November 8 2015. However, as discussed in Chapter 2, the XCO_2 run's ensemble was not fully spun up by October 22. Thus for most comparisons in this chapter, we examine the weeklong period starting November 1 2015.

In both experiments, a full suite of meteorological observations is assimilated. In addition to measurements of winds, humidity, and temperature from radiosonde, from aircraft, and from the Aircraft Communications Addressing and Reporting System (ACARS), we assimilate satellite-based drift wind measurements and land- and marine-based altimetry measurements. As in Raeder et al. (2012), we assimilate COSMIC GPS Radio Occultation (GPS RO, Anthes et al. (2008)) refractivity measurements. Raeder et al. (2012) showed that these GPS RO measurements, when added to NCEP-NCAR reanalysis observations, reduce the error of temperature forecasts compared to radiosonde temperature observations in both hemispheres, and most significantly in the Southern Hemisphere extratropics. These observations should also impact pressure and humidity, since they measure refractivity, which is a function of pressure and water vapor pressure in addition to temperature. From Anthes et al. (2008), the equation governing refractivity (N) is:

$$N = 77.6\frac{P}{T} + 3.73 \times 10^5 \frac{e}{T^2} - 4.03 \times 10^7 \frac{n_e}{f^2} \tag{3.4}$$

where P is pressure in hPa, e is water vapor pressure in hPa, T is temperature in K, n_e is electron density in number of electrons per cubic meter, and f is the frequency of the GPS carrier signal in Hz.

Observation counts for these various observation types, for a 48-hour period in the XCO_2 run can be seen in Figure 3.1. For brevity, this figure shows the global coverage for a representative observation for ACARS, aircraft, radiosonde, and satellite winds, but we should note that in each of these cases more than just the observation depicted is assimilated. Assimilated ACARS observations and aircraft observations include u and v wind in addition to temperature. Assimilated radiosonde observations include winds and temperature in addition to specific humidity, and assimilated satellite winds included both u and v components. Seven of the eight panels in this figure (all except the final panel, OCO-2 XCO_2) give counts of observations assimilated that apply to both the Met and XCO_2 runs.

We note here that the observation counts for the OCO-2 XCO_2 are fewer than the expected raw counts from the instrument for two reasons. First, they are so-called "super-observations" – observations which have been scaled up from OCO-2's footprint (1.29 km x 2.25 km at nadir, Crisp et al. (2004)) to a scale more congruous with typical global circulation model resolution. The strategy for creating these super-observations can be found in Chapter 2 of this dissertation. Secondly, the observations that enter the bins for the super-observations are screened for quality: only those soundings marked "good" quality in the OCO-2 Lite data product are included, and only those with 'warn level" less than 19 are included.

The state vectors in these model runs include winds (u and v), surface pressure (Ps), humidity (Q), and CO_2 tracers C_{fossil} and C_{total}. These tracers are informed by prescribed surface fluxes of CO_2 corresponding to CarbonTracker's 2015 product (Peters et al. (2007), https://www.esrl.noaa.gov/gmd/ccgg/carbontracker/CT2015/), interpolated from monthly

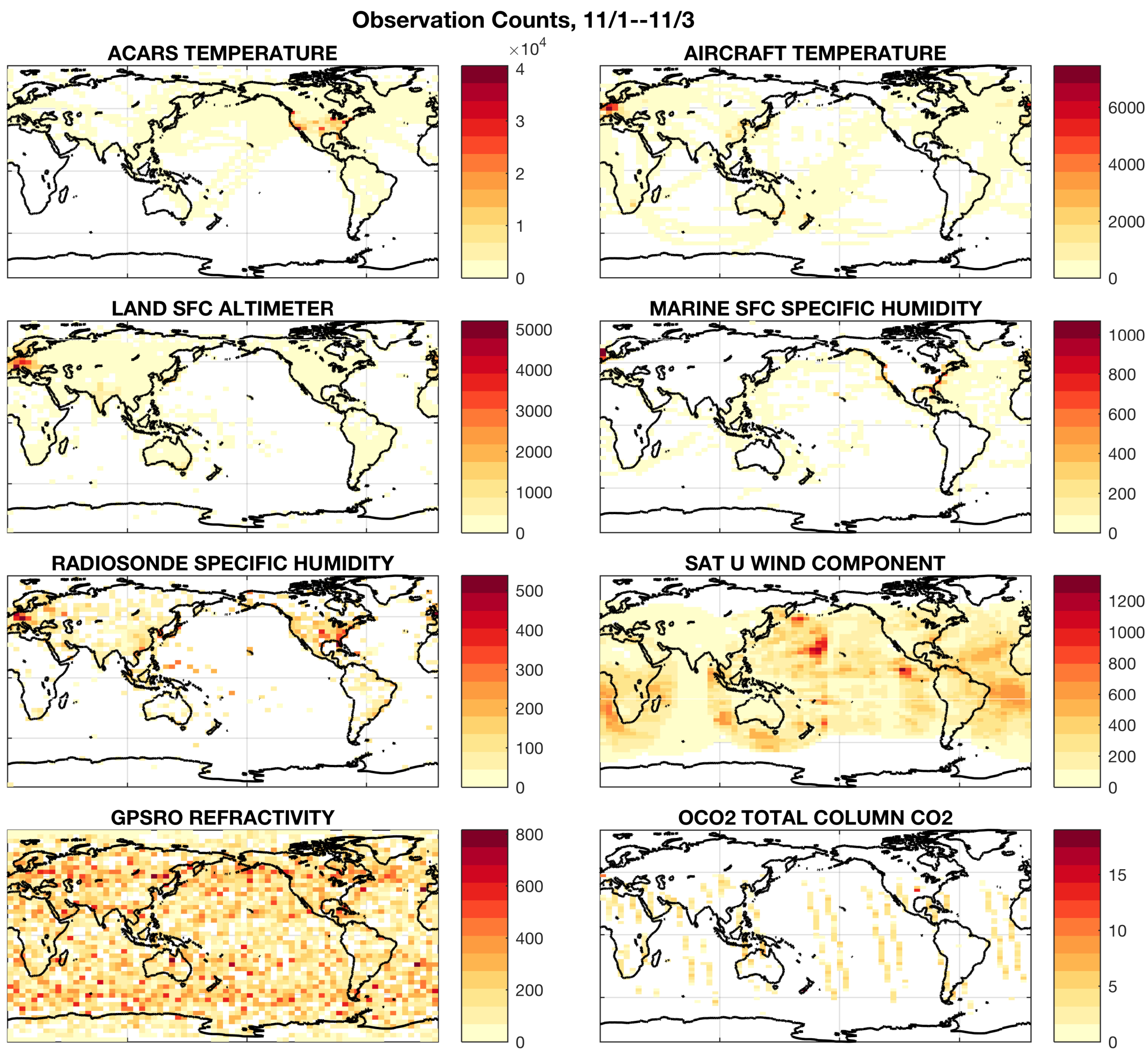

Figure 3.1: Observation counts for eight observation types, for a 48-hour period (0300UTC November 1 through 0300UTC November 3) in the XCO_2 run. From upper left to lower right, observation counts for: ACARS temperature, Aircraft temperature, land surface altimeter, marine surface specific humidity, radiosonde specific humidity, satellite horizontal (u) wind, GPS RO refractivity, and OCO-2 total column CO_2. Note that in the Met run, all observation types except OCO-2 XCO_2 are assimilated, and have identical coverage to those reported here.

to 6-hourly fluxes. C_{total} in this case is the sum of CO_2 tracers from fossil fuel emissions, natural terrestrial land processes (including forest fires), and natural ocean processes. C_{fossil} is then the tracer forced by fossil fuel emission alone.

3.3 Results

3.3.1 Results from the TPW experiment

In a data assimilation experiment, one way to test whether the experiment is working properly is to examine the innovation for a single time step. The innovation of a given state variable is the difference between the posterior and prior values for that variable. If the innovation is non-zero, that means the observations are having some influence on the forecasts.

Maps of the innovation for each state variable demonstrate where adjustments were made to the state to bring it closer to the observed variable. In Figure 3.2, we see that the OCO-2 TPW observations adjusted the forecast for all state vector fields (u, v, Q, T, Ps). This indicates that the OCO-2 TPW observations could be useful in informing not only the humidity field, but also in informing the wind, temperature, and surface pressure fields, thus likely improving weather forecasts for multiple fields. The signs of these innovations follow what is expected from atmospheric physics. Where the innovation in humidity is negative, surface pressure is also adjusted to be lower, since there is less mass in the overlying column. Examining the gradient in surface pressure innovation in the middle right panel of Figure 3.2, we see that where the innovation in the zonal component of the surface pressure gradient is positive, the innovation in meridional wind (v, in the upper right panel) is also positive, which follows our expectation for geostrophic wind:

$$f v_g = -\frac{1}{\rho}\frac{\partial p}{\partial x} \tag{3.5}$$

where f is the Coriolis parameter, v_g is the meridional component of geostrophic wind, ρ is the density of air, and $\frac{\partial p}{\partial x}$ is the zonal pressure gradient.

We see that the innovation's footprint for all fields is clearly related to the quadrant of the globe that is observed by OCO-2 during the 6-hour assimilation window, as innovation is non-zero in this quadrant but essentially zero elsewhere. The largest innovation is in the Southern Ocean, which has unstable weather (storms) and strong winds.

We can also examine how closely the ensemble forecasts track the true atmospheric state when they are constrained by the OCO-2 TPW observations alone. In Figure 3.3, we see the time evolution of the ensemble forecasts and true state at 70°W, 29.7°S at (the west coast of Chile), at the 525 hPa level. For the duration of this experiment, the ensemble forecasts bracket the truth for all state variables.

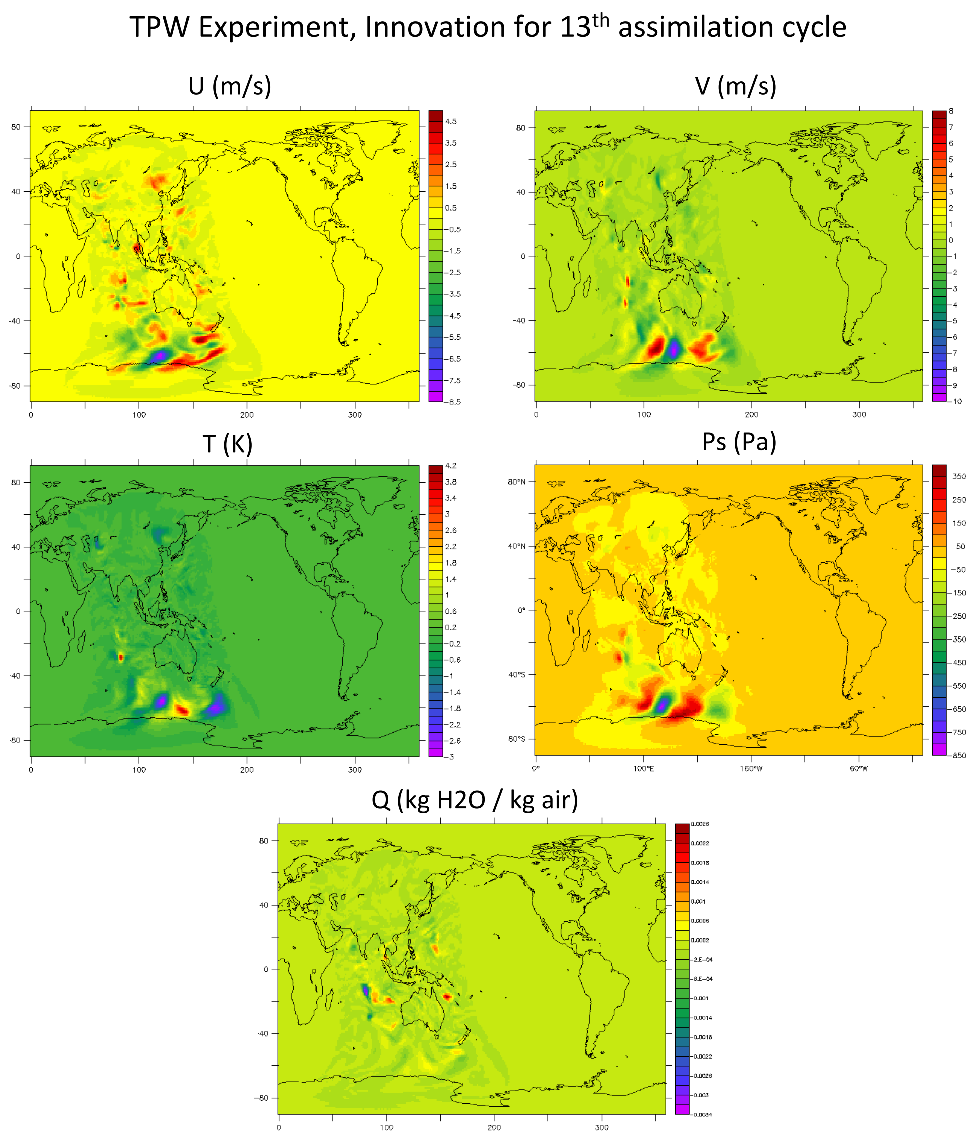

Figure 3.2: Innovation in the ensemble mean (Posterior Mean - Prior Mean) for the five state variables in the TPW experiment, resulting from the 13th assimilation cycle. All variables shown are at the 525 hPa level, except surface pressure.

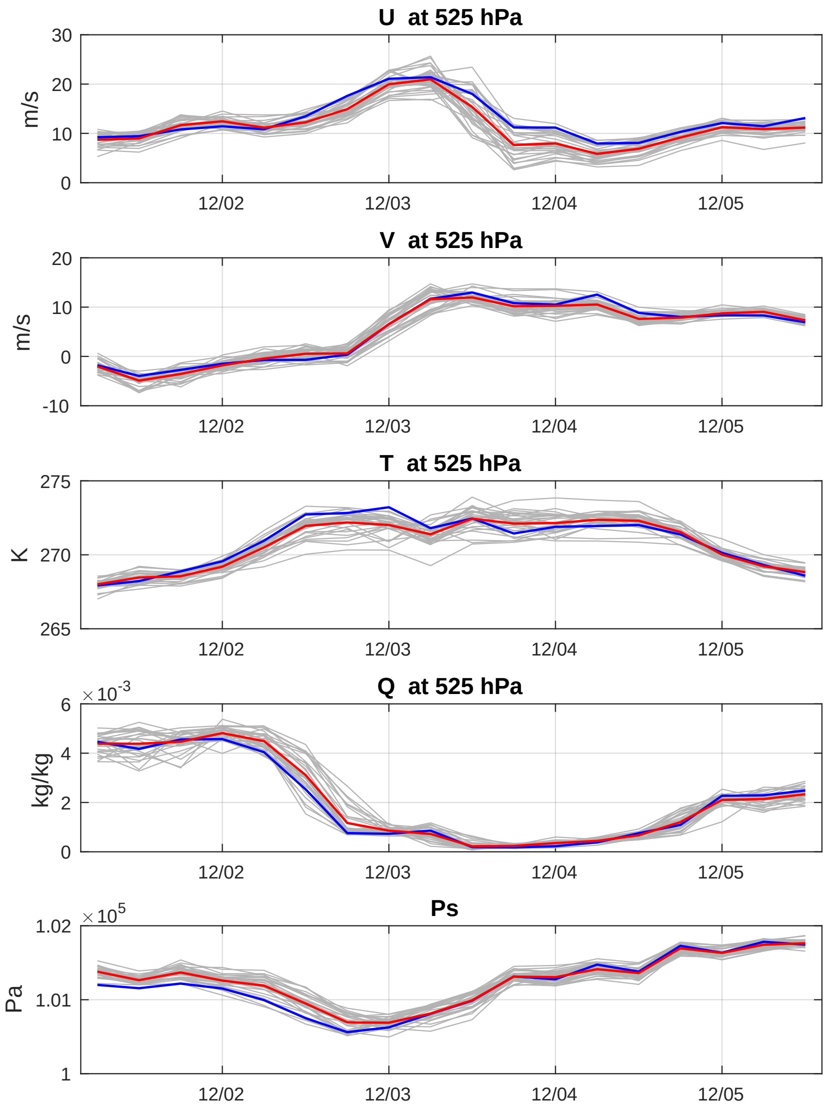

Figure 3.3: In the TPW experiment, the time evolution at a single point (70°W, 29.7°S, 525 hPa) for all state variable forecasts for all ensemble members (gray), the ensemble mean (red), and the true values (blue) taken from the "truth" free run of CAM.

3.3.2 Results from the XCO_2/Met Experiment

In this section we compare the forecast performance in the "XCO_2" and "Met" runs by examining the state-space root-mean-square error (RMSE) for the atmospheric state variables. Each variable $x(i, j, k, l)$ in the state vector ($\overrightarrow{x} = [u, v, T, Ps, Q, C_{fossil}, C_{total}]$) varies in three-dimensional space and in time, so the RMSE can be aggregated across a region, a portion of the atmospheric column, or a time period. Here i is the longitudinal index, j is the latitudinal index, k is the vertical index, and l is the time index.

To calculate the RMSE global map for a portion of the atmosphere ranging from pressure level k_{bottom} to k_{top} for a time period beginning at $l_{initial}$ and ending at l_{final}, we use:

$$RMSE(i, j) = \sqrt{\frac{\sum_{k=k_{bottom}}^{k_{top}} \sum_{l=l_{initial}}^{l_{final}} (\hat{x}(i, j, k, l) - x(i, j, k, l))^2}{(k_{top} - k_{bottom} + 1)(l_{final} - l_{initial} + 1)}} \tag{3.6}$$

Similarly, to calculate the RMSE time series for each pressure level, for a region spanning in latitude from i_{west} to i_{east} and from j_{south} to j_{north}, we use:

$$RMSE(k, l) = \sqrt{\frac{\sum_{i=i_{west}}^{i_{east}} \sum_{j=j_{south}}^{j_{north}} (\hat{x}(i, j, k, l) - x(i, j, k, l))^2}{(i_{east} - i_{west} + 1)(j_{north} - j_{south} + 1)}} \tag{3.7}$$

Finally, to calculate a single RMSE value for each level, for a given region and time period, we use:

$$RMSE(k) = \sqrt{\frac{\sum_{i=i_{west}}^{i_{east}} \sum_{j=j_{south}}^{j_{north}} \sum_{l=l_{initial}}^{l_{final}} (\hat{x}(i, j, k, l) - x(i, j, k, l))^2}{(i_{east} - i_{west} + 1)(j_{north} - j_{south} + 1)(l_{final} - l_{initial} + 1)}} \tag{3.8}$$

In the three equations above, $\hat{x}$ is a forecast of a particular state variable (i.e., the mean of the prior ensemble), and x is the true value of that variable, taken from the truth integration from which the pseudo-observations for the assimilation runs are harvested. $RMSE_{Met}$ and $RMSE_{XCO2}$ are calculated using the forecasts ($\hat{x}$) from the Met and XCO_2 runs, respectively. In this chapter, all RMS errors presented use forecasts (i.e., the prior state) rather than the analysis (i.e., the posterior state). This gives us a measure of error for a weather forecast at the 6-hour time horizon.

The time evolution of RMSE ($RMSE(k, l)$) for the southern extratropics (south of 20°S) is shown in Figure 3.4 for the full comparison period (October 22 through November 8), for each state variable and at several pressure levels. Here and in the rest of the figures in this chapter, we have chosen to show only the total CO_2 tracer (C_{total}) rather than both C_{total} and C_{fossil}, as the two tracers have similar error statistics. We focus on the Southern Hemisphere for two reasons. First, the experiment is performed in late boreal autumn, so there are more OCO-2 observations available in the Southern Hemisphere than the Northern Hemisphere. Second, the Northern Hemisphere CO_2 surface flux forcing has a large bias in its fossil fuel forcing (intentionally imposed as described in Chapter 2), which could cause the XCO_2 observations to be less effective in informing the weather state in that hemisphere.

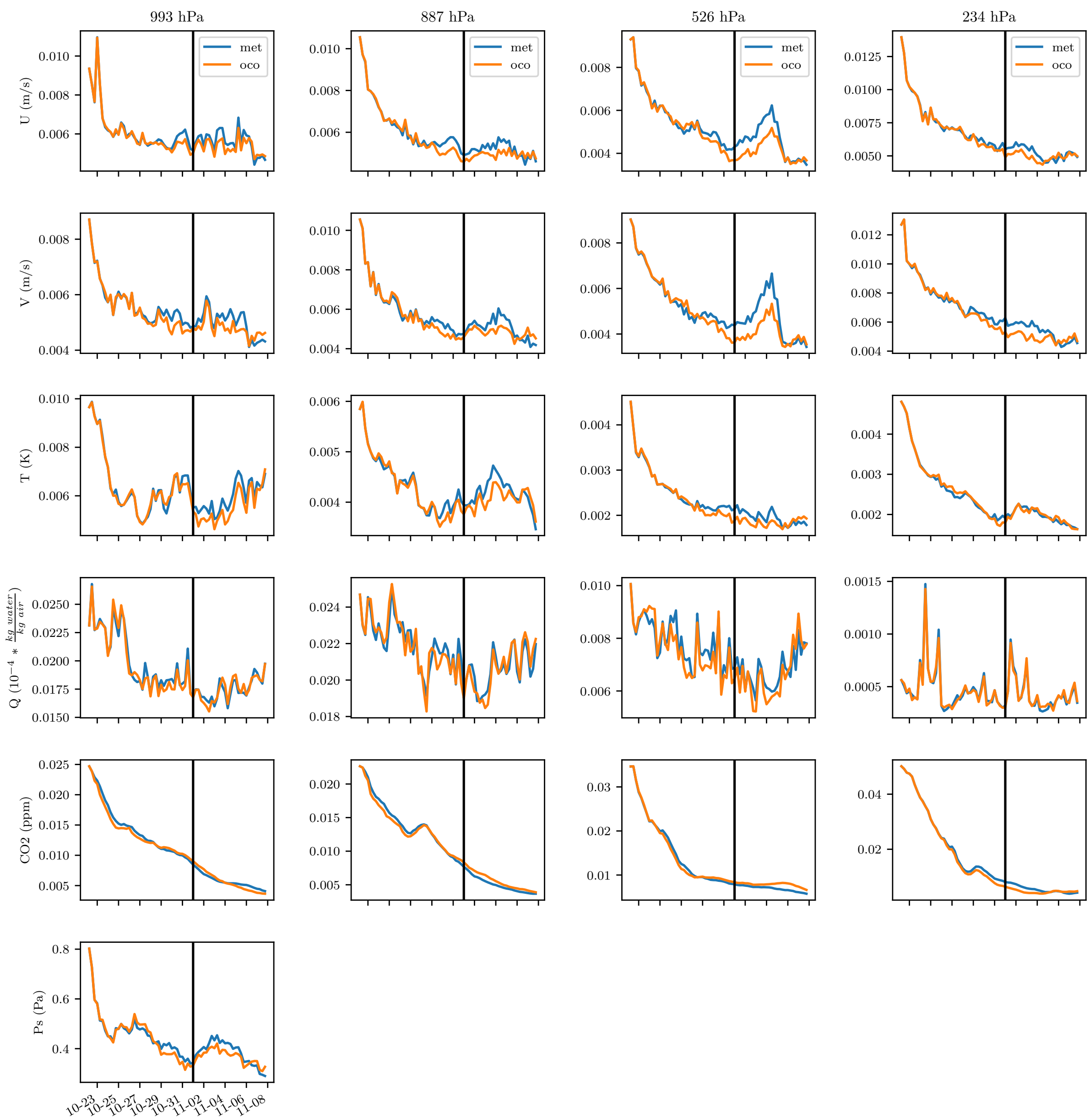

Figure 3.4: RMSE time series for state variable forecasts at 4 representative pressure levels for the XCO_2 run (orange) and the Met run (blue), for the southern extratropics (south of 20°S). Vertical black line indicates November 1, the period after which we determine that the RMSE has stabilized.

Since Southern Hemisphere CO_2 is decoupled from Northern Hemisphere sources at these time scales, this bias should not impact our analysis of the Southern Hemisphere.

It is evident in Figure 3.4 that the ensemble has not stabilized by October 22, as the RMSE for all state variables decreases steadily for the first week of the time period. RMSE has stopped decreasing steadily starting November 1 for all meteorological variables, so this is the time period used for the subsequent figures and discussions in this chapter. November 1 is indicated by the vertical bars in the various panels of Figure 3.4.

In Figure 3.4, we see lower RMSE for the XCO_2 run (orange line) compared to the Met run (blue line) for most time steps after November 1, for all meteorological state variables except humidity, whose XCO_2 RMSE time series follows a near-identical trajectory as the Met RMSE time series. When an analogous figure is produced that includes all global grid boxes, we see similar but muted error reduction for v wind at 526 hPa and 887 hPa, T at 887 hPa, and surface pressure. Additionally, in the global figure, we see significant improvement in CO_2 forecasts, especially at the surface level. This is expected when the Northern Hemisphere is included, since the CO_2 fields are not directly constrained by XCO_2 observations in the Met run, and thus the bias imposed in the Northern Hemisphere fossil fuel CO_2 forcing is largely uncorrected in the Met run.

We define the percent improvement in RMSE (PI_{RMSE}) as:

$$PI_{RMSE} = 100 \times \frac{RMSE_{Met} - RMSE_{XCO2}}{RMSE_{Met}} \tag{3.9}$$

PI_{RMSE} measures the percent reduction in RMS error when assimilating OCO-2 XCO_2 in addition to meteorological observations. PI_{RMSE} as a function of vertical level for each state variable is summarized in Figure 3.5. Time steps after the RMSE has stabilized (November 1 - November 8) are included in the calculations here, and we present results when we include (1) all latitude bands (global), (2) latitudes north of 20°N (the northern extratropics), (3) latitudes south of 20°S (the southern extratropics), and (4) latitudes between 55°S and 45°S (the Southern Ocean).

Globally, the most obviously improved state variable is CO_2, and we see that this is due to significant improvement in the northern extratropics. This is expected because the Met run includes the same bias in C_{fossil} forcing as does the XCO_2 run, but the Met run's CO_2 tracers are not directly constrained by XCO_2 measurements. In the Northern Hemisphere, especially in the upper levels, adding XCO_2 observations tends to increase RMS error (blue boxes). The exception is for v wind between 993 hPa and 800 hPa, for temperature at 860 hPa, and for the 6 lowest pressure levels for all state variables except humidity. Some of the Northern Hemisphere error increases could have been influenced by the biased C_{fossil} forcing. In spite of this bias, we do see improvement in lower-level v wind. The strong meridional CO_2 gradient may have aided in improving meridional wind.

A fairer test of the impact of OCO-2 XCO_2 observations on weather forecasts is to look at the Southern Hemisphere extratropics, whose CO_2 state variables are not yet (after 2 weeks) affected by the false emissions over China. The bottom left panel of Figure 3.5 shows the percent improvement in this region. Here we see that for most levels, forecasts of all meteorological state variables except humidity are improved when OCO-2 XCO_2 is assimilated. The magnitude of error increases for Q are small in comparison to the improvements in u, v, T, and Ps. When confining our scope to the region corresponding to the Southern Ocean storm tracks (lower right panel in Figure 3.5), forecast improvement largely disappears, and even reverses.

In Figure 3.6, we show maps of time-averaged absolute RMSE improvement ($RMSE_{Met} - RMSE_{XCO2}$) for each state variable. For all variables except surface pressure, the bottom 12 levels (up to 525 hPa) are included in the RMSE calculation, since globally, that is where the largest improvements are located. Overlain are contours indicating the number of OCO-2 XCO_2 observations available in the region. We see that there is some overlap between forecast improvement and XCO_2 observation density: for example, in the American Southwest, a high density of OCO-2 soundings coincides with forecast improvement (red) in all meteorological state variables. Another well-observed region in northern Africa shows forecast improvement in most fields.

To serve as a measure of the significance of forecast improvement, we show in Table 3.3.2 the probability of improvement for each meteorological variable in the full globe (all latitudes) and in the Southern Hemisphere extratropics (south of 20°S). This probability is calculated as the number of improved grid boxes (where $RMSE_{XCO2} < RMSE_{Met}$) divided by the number of total grid boxes in the region. Similarly to in Figure 3.6, for all variables but surface pressure we average RMSE over all atmospheric levels below 525 hPa. Other than the global surface pressure field, all probabilities shown are significantly (at the 99.999 percent confidence level) greater than 0.5, which is the expectation for a random chance of improvement/worsening of the forecast. Taken together with the results for the average percent improvement for the same regions (Figure 3.5), we have strong confidence that addition of XCO_2 observations significantly improved forecasts globally and in particular in the southern extratropics for both wind and temperature fields. The case for forecast improvement in surface pressure and humidity fields is not as strong.

3.4 Discussion and Conclusions

The two experiments presented in this chapter both provide evidence that OCO-2 could provide some useful observations to be added to the suite of observations ingested by national weather centers. In the TPW experiment, where OCO-2 TPW is the only observation type assimilated, the TPW observations impact all meteorological state vector fields, and the ensemble of forecasts bracket the true atmospheric state in most places throughout the globe. This experiment gives more weight to the claim by Nelson et al. (2016) that OCO-2 TPW observations could improve NWP performance.

Our TPW result could be further explored using a twin experiment similar to the XCO_2/Met experiment, in which a suite of satellite, radiosonde, and aircraft observations of temperature, humidity, and winds typically used for NWP are assimilated in addition to OCO-2 TPW. A control run would include the typical weather observations, but it would

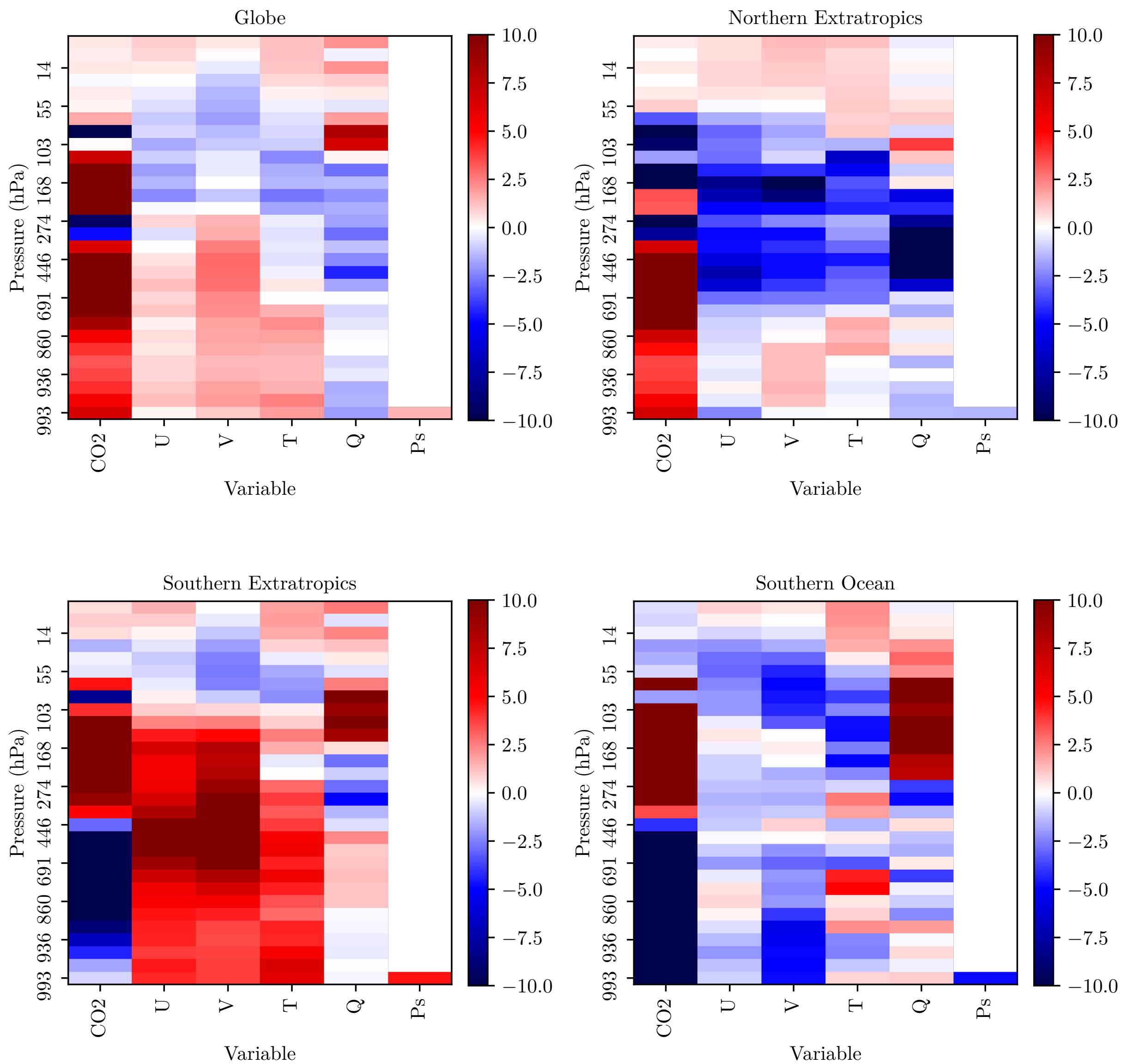

Figure 3.5: Arrays summarizing forecast error reduction for each state variable, at each pressure level, upon addition of XCO_2 observations, expressed as percent improvement : $PI_{RMSE} = 100\% \times [RMSE_{Met} - RMSE_{XCO2}]/RMSE_{Met}$. Regions shown are the full globe (upper left panel), north of 20°N (upper right panel), south of 20°S (lower left panel), and 45°S - 55°S (lower right panel). Positive (red) values indicate that adding XCO_2 improved the forecast, while negative (blue) values indicate that adding XCO_2 observations worsened the forecast for that state variable. Only 11/01 - 11/08 time steps are included to avoid the spin-up period seen in Figure 3.4.

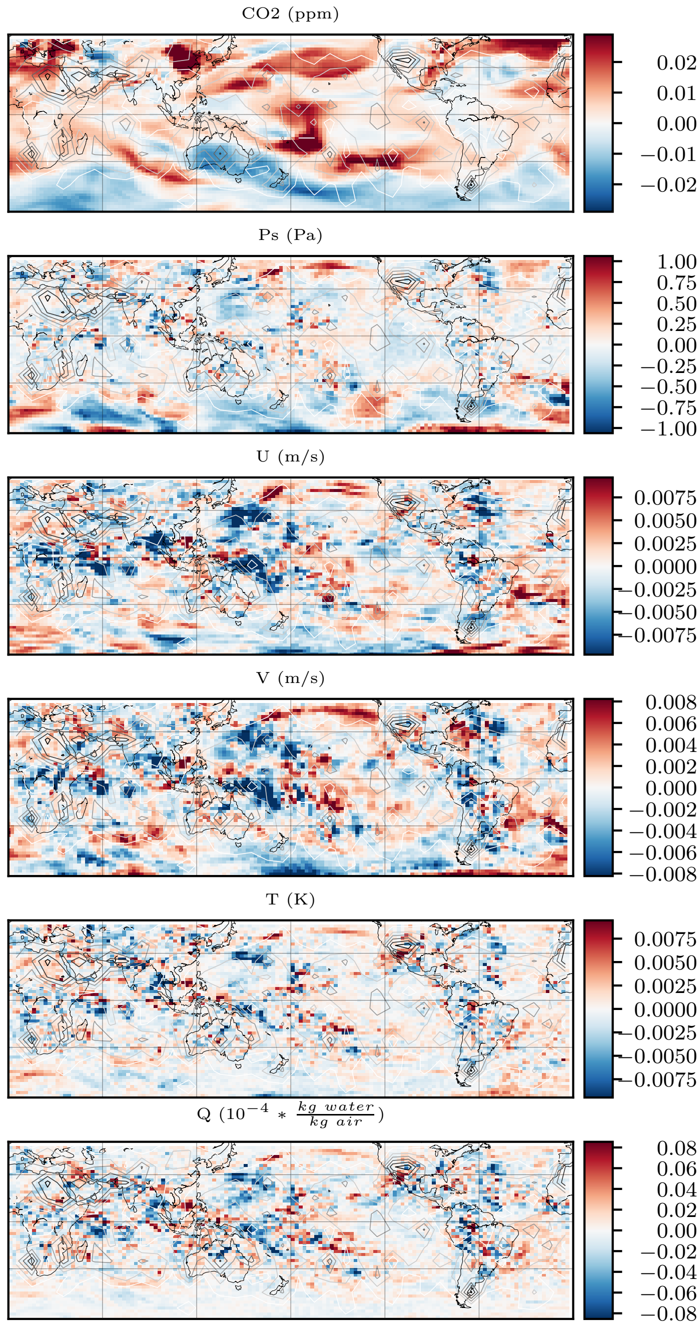

Figure 3.6: Forecast improvement, i.e. $[RMSE_{Met} - RMSE_{XCO2}]$ (color), for all state variables. For all variables except Ps, the improvement is vertically averaged up to 525hPa. Contours show XCO_2 observation counts ingested during the same period as the RMSE maps (Nov 1-8). Counts are aggregated to 10° x 10° grid boxes. Contour levels are $[8, 16, 24, 32, 48]$ observations per box (the maximum count per box is 53). The map's latitude range is set to the latitudinal extent of OCO-2 observations for this period. Positive (red) color indicates adding XCO_2 improves the forecast.

Table 3.2: Probability that the given state variable is improved when XCO_2 is assimilated.

Variable	$P(improvement)$ Globe $N = 13{,}824$; $E = 0.0188$	$P(improvement)$ Southern extratropics $N = 5{,}184$; $E = 0.0307$
U	0.5259	0.6032
V	0.5283	0.5847
T	0.5418	0.6009
Q	0.5250	0.5945
Ps	0.4921	0.5451

Note. — The probability is calculated as the number of improved grid boxes (e.g., the number of red boxes in Figure 3.6) divided by the total number of grid boxes (N) in the region. E is the error corresponding to the 99.999 percent level of confidence (Z value = 4.4172). Probabilities greater than 0.5 ± E are interpreted as being significant. The southern extratropics includes all areas south of 20°S whereas the globe includes all model grid boxes.

exclude the OCO-2 TPW experiments. Of particular interest in such an experiment would be typically poorly-observed regions such as the Southern Ocean. The experiment would differ from the XCO_2/Met experiment presented in that we would need to include other satellite-based moisture observations which are typically used in NWP, to test whether OCO-2 TPW provides unique information in addition to the complete set of available humidity observations.

We note that the OCO-2 retrieval algorithm also estimates the surface pressure of each sounding by exploiting information in the O_2 A band. O'Brien et al. (1998) found that surface pressure derived from high-resolution A-band spectra yielded accuracies on the cusp of the accuracy requirement for NWP surface pressure retrievals (an accuracy of ∼1 hPa or 0.1%). A systematic evaluation of the accuracy of OCO-2 surface pressure retrievals similar to the TPW analysis performed by Nelson et al. (2016) should be a first step in determining the utility of OCO-2 surface pressure retrievals for NWP. Following that, a simplified OSSE such as the TPW experiment presented here, or a twin experiment such as the XCO_2/Met experiment, would give further insight into the usefulness of these measurements.

Results from the XCO_2/Met experiment show that OCO-2 XCO_2 has the potential to improve weather forecasting abilities, especially in the v wind field and in otherwise observation-poor areas. In the northern extratropics, in spite of a non-ideal fossil fuel boundary condition for the C_{fossil} state, we see improvement in lower-level v wind. It is likely that the strong meridional gradient in CO_2 provided the v wind with useful informational constraints.

In the southern extratropics, we see marked forecast improvements (as measured by percent improvement in RMSE, averaged over the region) for all meteorological fields, except humidity, when XCO_2 is assimilated. Skill in Southern Hemispheric weather forecasting has improved significantly since forecast centers began assimilating satellite radiances (Simmons and Hollingsworth (2002)), and in 2013, forecast skill for the Southern Hemisphere extra-

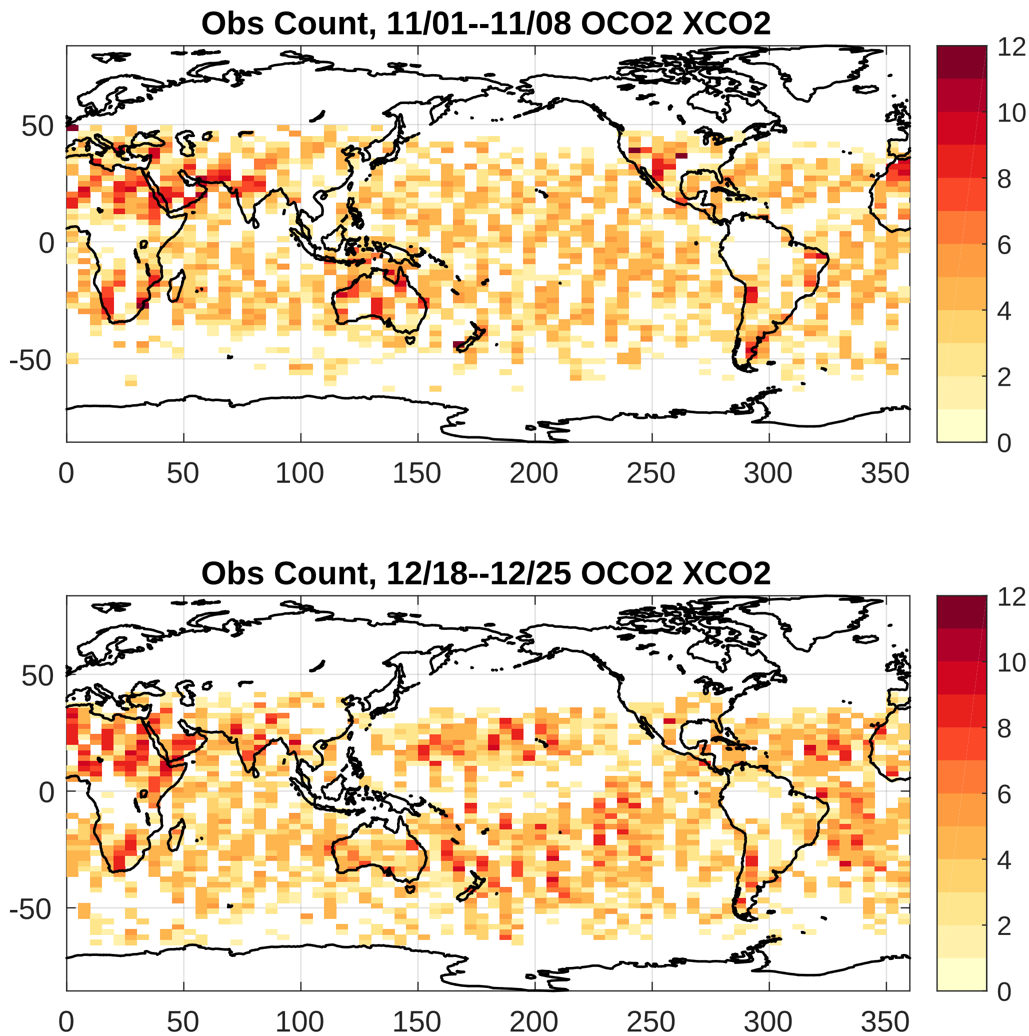

Figure 3.7: Upper panel: Counts of OCO-2 XCO_2 high-quality super-obs available during the period included in the RMSE maps (November 1 through November 8). Lower panel: The same as the upper panel, but for the period when Southern Hemisphere observations reach the highest latitudes, December 18-25. The count varies with insolation, cloud cover and OCO-2 operations.

tropics nearly matched that of the Northern Hemisphere extratropics (Bauer et al. 2015). Nonetheless, the fact remains that the Southern Hemisphere is more poorly-observed than the Northern Hemisphere, in particular in its wind fields because satellites do not provide direct wind observations.

This study indicates that adding OCO-2 measurements to an NWP framework might be a worthwhile endeavor, especially in austral summer when the instrument provides its highest density of observations to the Southern Hemisphere. We do not see as strong of a case if we look only at the Southern Ocean storm track region (45°S-55°S, as per Brahmananda Rao et al. (2003)). This is likely because, while some OCO-2 super-observations are present in this experiment in this region of the Southern Hemisphere, the coverage is limited at these high latitudes. In the upper panel of Figure 3.7 we see that south of 45°S there are very few observations for the November 1-8 time period. We note that the improvement could be larger in this region during the period encompassing winter solstice, when more high-quality OCO-2 observations are available in high southern latitudes. As depicted in the lower panel of Figure 3.7, more observations are available south of 45°S in a 7-day period centered on winter solstice (December 18-25). The total number of good OCO-2 XCO_2 super-observations south of 45°S in the winter solstice week is 594, compared to just 266 in the November period for which we have presented RMSE improvement results.

Interestingly, the only meteorological variable that was not improved (as measured by the average percent improvement in RMSE, Figure 3.5) on the globally-aggregated scale in the XCO_2/Met experiment was humidity (Q). One reason this may be the case is that humidity is well-constrained in our experiments by abundant GPS radio occultation observations. As seen in Figure 3.1, GPS RO observations blanket the entire globe, including the Southern Hemisphere oceans, and as mentioned in Section 3.2.2, GPS RO measures refractivity, which is a function of water vapor pressure. Refractivity is also a function of pressure and temperature, so a lack of improvement in these fields would give weight to this hypothesis. While surface pressure's percent improvement was positive, the chance of improvement in surface pressure for a grid box failed to exceed random chance (Table 3.3.2), indicating that surface pressure, in addition to humidity, is not significantly improved on the global scale. However, temperature forecasts were improved, and significantly more so than random chance, which leads us to suspect that the abundance of GPS RO observations is not the primary reason for lack of improvement in Q forecasts.

The lack of improvement in Q forecasts could also be due to the incongruity between characteristic length scales of dynamics governing Q and CO_2. In the XCO_2/Met experiment, we set the GC half-width (which governs the radius at which observations have impact on the state) for all state variables to $\sim$1200 km, but a shorter half-width could be more optimal for the Q field, since processes like precipitation occur over smaller areas. To test this theory in the future, a series of assimilation runs analogous to the XCO_2/Met runs would be carried out, but in each pair, the GC half-width for Q would be varied, and the optimal half-width would be determined. It could also be interesting to test different variable localization schemes (for example, zeroing out the impact of XCO_2 on Q).

Overall, this chapter demonstrates some promising results for satellite-based trace gas instruments such as OCO-2 to be used not just to understand atmospheric trace gas composition, but to potentially improve weather forecasting, providing even more value to the public. Similar experiments could be performed using observations from the multitude of other space-borne instruments which measure trace gases. Carbon monoxide retrievals from IASI and MOPITT have been successfully assimilated alongside weather observations using DART and global climate and atmospheric chemistry model CAM-chem (Arellano et al. 2007; Barré et al. 2015; Gaubert et al. 2016). However, in all of these studies a variable localization scheme was chosen such that CO observations would not influence the meteorological state, so the potential impact of CO observations on weather forecasts was not analyzed or discussed. Liu et al. (2017b) assimilated pseudo-observations of NO_2 from a planned geostationary instrument using DART and high-resolution regional weather-chemistry model WRF-Chem. As in the CO studies, in this study NO_2 observations were not able to impact the meteorological state, but the authors noted that in future experiments they would allow NO_2 to statistically influence meteorological state variables, to test whether NO_2 observations improve the meteorological analyses. NO_2, which has a short atmospheric lifetime of several hours, might be better-suited than CO_2 to provide information on synoptic time-scale processes.

Chapter 4

Estimating net CO_2 surface flux using a vertically-integrated mass budget method with a focus on the Amazon carbon sink

Abstract. Here we calculate global CO_2 surface fluxes in a novel way for the year 2003 using time-varying 3D-CO_2 and meteorology reanalysis fields generated by Liu et al. (2012). This data product was created by assimilating raw meteorological observations and Atmospheric Infrared Sounder column-averaged dry-air CO_2 mole fraction (AIRS-XCO_2) observations using a Local Ensemble Transform Kalman Filter (LETKF) coupled with the Community Atmospheric Model version 3.5 (CAM 3.5). We calculate surface fluxes as a residual of the vertically-integrated CO_2 tracer transport equation. We find that assimilating AIRS-XCO_2 has the most significant impact on the surface flux calculation in the tropics, especially over the Amazon and in the tropical Pacific. We compare our posterior flux estimates to those made by CarbonTracker (CT2017) and find general sign agreement except in the Amazon region. Here we estimate a net annual sink of -0.26 PgC whereas CarbonTracker estimates a net annual Amazonian source of about the same magnitude.

4.1 Introduction

Only about half of CO_2 emissions from fossil fuels contribute to the concentration of CO_2 in the atmosphere (Le Quéré et al. 2009). The remainder is sequestered by carbon sinks in the oceans and in the terrestrial biosphere. The spatial distribution of these sources and sinks (CO_2 surface fluxes) can be inferred using tracer-transport inversion, in which observations of the concentration of CO_2 in the atmosphere can be used to update the surface flux forcing to best fit the observations. These inversion estimates are highly uncertain due the confounding factors of sparse observation availability and imperfect representation of atmospheric transport. Thus, the relative sizes of carbon sinks and how they will respond to a changing climate are unsettled issues. For example, the relative partitioning of northern hemispheric carbon uptake between Eurasia and North America has historically been highly uncertain (Bousquet et al. 2000). Estimates of tropical carbon uptake are especially difficult due to scant observation coverage and strong convective mixing which dilutes the surface flux signal throughout the troposphere.

We have developed a carbon-weather data assimilation system that produces 4D-CO_2 reanalysis fields (Liu et al. 2012). In this system, Atmospheric Infrared Sounder (AIRS) column-averaged dry-air CO_2 mole fraction (XCO_2) and raw meteorological observations have been assimilated into a coupled carbon-climate model. A comparison of the resultant 4D-CO_2 fields (1) when only meteorological observations were assimilated (the Met-run) and (2) when both meteorology and AIRS-XCO_2 were assimilated (the AIRS-run) shows that the AIRS-run CO_2 field is closer to unassimilated observations of vertical CO_2 profiles from aircraft than the Met-run CO_2 field (Liu et al. 2012). Here we present an estimation of CO_2 surface fluxes calculated from these CO_2 and wind fields. We focus our analysis on the Amazon Basin region, where the idea of a dry season "green-up" has been discussed in Huete et al. (2006) and Saleska et al. (2003).

4.2 Methods

4.2.1 Assimilation Experiments

The assimilation experiments are described in detail in Liu et al. (2012) and are summarized here. AIRS-XCO_2 and meteorological observations were assimilated using a 4-D Local Ensemble Transform Kalman Filter (4D-LETKF, Hunt et al. (2004), Hunt et al. (2007)) coupled with the Community Atmospheric Model version 3.5 (CAM 3.5) for the year 2003, using sea surface temperature forcing from 2003 and observations from 2003. In this study we compare the case where only meteorological observations are assimilated (the Met-run) with the case where both meteorology and AIRS-XCO_2 are assimilated (the AIRS-run). Meteorological observations included the same raw observations used for NCEP-DOE reanalysis 2 product (Kanamitsu et al. 2002). Over 2000 AIRS-XCO_2 and 10^6 meteorological observations were assimilated every six hours. During each assimilation cycle, the LETKF would adjust the model forecasts of the "state vector" (which includes winds, surface pressure, temperature, humidity, and CO_2 mixing ratio) such that they were closer to contemporaneous observations, taking into account the observation uncertainty and the uncertainty of the model forecasts (represented by the "spread" in the 64 ensemble forecasts). The adjusted forecasts are called the "analysis."

To prevent the ensemble spread from becoming too small in observation-dense regions, Liu et al. (2012) employed multiplicative inflation (following Anderson and Anderson (1999), Li et al. (2009), and Miyoshi and Yamane (2007)) to the observation-space CO_2 and weather forecasts in both the AIRS-run and Met-run. For meteorological observations, they also applied additive inflation in an attempt to account for model error, as described in the supplemental material of Liu et al. (2011). Both meteorological and AIRS XCO_2 observations were localized in the vertical and horizontal such that observations farther in distance from an analysis grid box had less impact on the analysis (with observations 1500 km away having zero impact on the analysis). Liu et al. (2012) also employed variable localization, meaning that the meteorological components of the state vector were not updated by CO_2 observations, and CO_2 mixing ratios were not updated by meteorological observations.

For these experiments, CAM 3.5 was modified to allow the CO_2 mass fraction to be transported as a passive tracer. CO_2 surface flux was prescribed at the onset of each assimilation period and combined fluxes from fossil fuel, terrestrial biosphere, and ocean. No forcing from fires was included. The terrestrial biosphere surface flux changed every 6 hours, with zero annual mean everywhere. Monthly mean values of terrestrial CO_2 flux were from a climatological run of Carnegie-Ames-Stanford Approach (CASA) biosphere model, while 6-hourly fluxes were generated by scaling annually-balanced monthly mean flux with 6-hourly 2-meter temperature from CAM 3.5. Fossil fuel surface flux was constant for each grid box, scaled according to an emission map for 2003 with total global emission of 6.93 GtC/yr. Ocean forcing was from Takahashi et al. (2002), a climatology based on ship-board observations over multiple decades. As the land forcing for the AIRS- and Met-runs was annually-balanced, a goal of the analysis presented here is to assess if the 2003 land flux anomalies can be estimated when the model's atmospheric CO_2 abundance is informed by AIRS XCO_2.

4.2.2 Surface Flux Calculation

Although CO_2 surface flux was not included in the state vector in the data assimilation experiments described above, it can be estimated from the analysis CO_2 and meteorological fields (from the AIRS and Met runs) in an offline manner. These analysis fields are Liu et al. (2012)'s best estimate of the state of the atmosphere at the time resolution of the assimilation window (every 6 hours).

The key to our surface flux estimation is the tracer conservation equation:

$$\frac{\partial \rho C}{\partial t} + \nabla \cdot (\overrightarrow{u_3} \rho C) = \Phi + \gamma(\rho C) \tag{4.1}$$

Here ρ is air density, C is CO_2 mass fraction, u_3 is the three-dimensional velocity vector, Φ is the CO_2 surface flux, and γ represents subgrid scale turbulent mixing associated with dry and moist convection.

Integrating Equation 4.1 in the vertical yields:

$$\Phi = \frac{\partial \langle \rho C \rangle}{\partial t} + \nabla \cdot \langle \overrightarrow{u_2} \rho C \rangle \tag{4.2}$$

where u_2 is the two-dimensional horizontal velocity vector. The CO_2 surface flux can, in principle, be estimated directly from equation 4.2, i.e. as the sum of the time change in column CO_2 mass and vertically-summed flux divergence.

Monthly mean surface fluxes are calculated for each of the 64 ensemble members for each month of the 2003 runs. The spread (σ_Φ) among the surface fluxes is estimated as the standard deviation of the 64-member ensemble according to 4.3.

$$\sigma_\Phi = \{\frac{1}{K-1}\sum_{k=1}^{K}[\Phi_k - \overline{\Phi}]^2\}^{\frac{1}{2}} \tag{4.3}$$

Here K is the number of ensemble members (64), and $\overline{\Phi}$ is the mean surface flux among the ensemble members:

$$\overline{\Phi} = \frac{1}{K}\sum_{k=1}^{K}\Phi_k \tag{4.4}$$

$\overline{\Phi}$ and σ_Φ can be calculated in this way from the 3-D CO_2 posterior (i.e., analysis) tracer and meteorological fields for either experiment from Liu et al. (2012). We denote the monthly-mean surface flux estimated from AIRS-run fields as $\overline{\Phi}_{AIRS}$, and surface flux estimated from the Met-run as $\overline{\Phi}_{Met}$. Correspondingly, we denote the spread in monthly surface fluxes for the AIRS run with $\sigma_{\Phi,AIRS}$ and the spread in monthly surface fluxes for the Met run with $\sigma_{\Phi,Met}$.

The spread (σ_Φ) encompasses the distribution of possible wind and CO_2 trajectories, so can be thought of as a model or transport uncertainty. There are other errors in the surface flux that arise from, for example, using 6-hourly fields (u_3, ρ, and C) to compute flux divergence rather than using their product calculated at the frequency of CAM's physical time step (every 30 minutes). We represent these methodological errors with ϵ_{AIRS} and ϵ_{Met}. If our methodology were perfect, $\overline{\Phi}_{Met}$ would be identical to our surface flux forcing (Φ_{Prior}), since no CO_2 observations were assimilated in the Met run, nor were CO_2 tracers part of the state vector. Differences between $\overline{\Phi}_{Met}$ and Φ_{Prior} are thus related to the methodological error ϵ_{Met}, hence:

$$\overline{\Phi_{Met}} = \Phi_{Prior} + \epsilon_{Met} \tag{4.5}$$

In the absence of ϵ_{AIRS}, $\overline{\Phi_{AIRS}}$ represents CO_2 surface fluxes for the year 2003, which should equal the sum of the prior forcing (Φ_{Prior}) and 2003 flux anomalies Φ'_{2003}. As Φ_{Prior} includes 2003 fossil fuel emissions, but climatological ocean fluxes and annually balanced net terrestrial fluxes, Φ'_{2003} should capture mostly 2003 land and ocean flux anomalies. Φ'_{2003} could also pick up on some fossil fuel signals that are misrepresented in Φ_{Prior} (for example, if fossil fuel emission differs greatly from month to month), however these signals will likely be smaller than the flux anomalies in the ocean and terrestrial biosphere. Including the methodological error term, $\overline{\Phi_{AIRS}}$ can be decomposed into these components:

$$\overline{\Phi_{AIRS}} = \Phi_{Prior} + \Phi'_{2003} + \epsilon_{AIRS} \tag{4.6}$$

Since ensemble-mean meteorological fields in the AIRS and Met runs are nearly identical, we can assume that $\epsilon_{AIRS} \sim \epsilon_{Met}$, thus:

$$\overline{\Phi_{AIRS}} \approx \overline{\Phi_{Met}} + \Phi'_{2003} \tag{4.7}$$

Rearranging equation 4.7, we see that the 2003 flux anomaly (Φ'_{2003}) can be estimated by subtracting $\overline{\Phi_{Met}}$ from $\overline{\Phi_{AIRS}}$.

We also estimate the 2003 flux anomalies using an alternative estimate of global carbon fluxes for 2003, that from CarbonTracker. CarbonTracker, an inversion system which is constrained by the GLOBALVIEW network of surface flask observations of CO_2, provides posterior global carbon fluxes at the monthly resolution (Peters et al. (2005, 2007), with updates documented at http://carbontracker.noaa.gov). By including the estimate from CarbonTracker, we have two estimates for the 2003 global fluxes, one that is informed by surface CO_2 observations and one that is informed by AIRS mid-tropospheric CO_2 observations. These two estimates for Φ'_{2003} are:

$$\Phi'^{AIRS}_{2003} \approx \overline{\Phi_{AIRS}} - \overline{\Phi_{Met}} \tag{4.8}$$

$$\Phi'^{CT}_{2003} \approx \Phi_{CT} - \Phi_{Prior} \tag{4.9}$$

Here Φ_{CT} is the 2003 CO_2 surface flux fields from the 2017 version of CarbonTracker (CT2017), regridded from their native 1° x 1° grid to the same grid as Φ_{Prior}, $\overline{\Phi}_{Met}$, and $\overline{\Phi}_{AIRS}$ (1.9° x 2.5°). Φ_{CT} is the sum of Φ_{CTbio}, $\Phi_{CTocean}$, $\Phi_{CTfossil}$, and Φ_{CTfire}, where Φ_{CTbio} and $\Phi_{CTocean}$ are CarbonTracker's posterior estimate of 2003 fluxes from the terrestrial biosphere and the oceans, respectively, and $\Phi_{CTfossil}$ and Φ_{CTfire} are their prescribed fossil fuel flux and prescribed fire flux, respectively. Commonalities between the community estimate (Φ'^{CT}_{2003}) and our estimate (Φ'^{AIRS}_{2003}) provide confidence in the correctness of both estimates, whereas discrepancies between the two indicate either misattributions of carbon fluxes by CT or by us.

We can also define a "posterior" monthly mean flux using the AIRS run fields and our approach as:

$$\overline{\Phi}_{Posterior} = \Phi_{Prior} + \Phi'^{AIRS}_{2003} \tag{4.10}$$

$\overline{\Phi}_{Posterior}$ can then be compared directly to Φ_{CT}. It follows that the posterior spread, $\sigma_{Posterior}$, for each month is achieved by summing $\sigma_{\Phi,AIRS}$ and $\sigma_{\Phi,Met}$ in quadrature:

$$\sigma_{Posterior} = \sqrt{\sigma^2_{\Phi,Met} + \sigma^2_{\Phi,AIRS}} \tag{4.11}$$

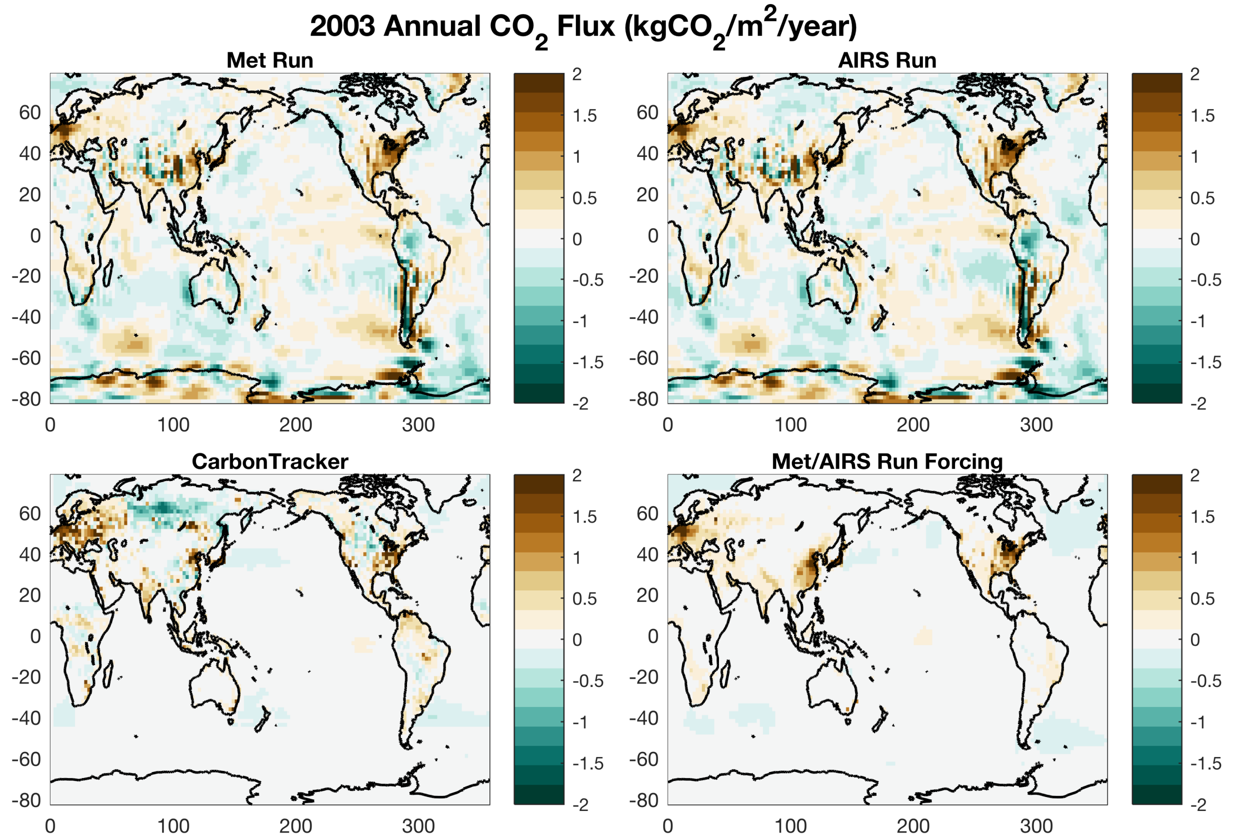

Figure 4.1: Annual CO_2 surface fluxes for the year 2003, in kg CO_2/m^2/year. The upper left panel shows the flux calculated using equation 4.2 from Met-run fields ($\overline{\Phi_{Met}}$). The upper right panel shows the same using AIRS-run fields ($\overline{\Phi_{AIRS}}$). The lower left panel is the annual total flux from CarbonTracker (Φ_{CT}), and the lower right panel is the annual flux used as forcing in both the Met- and AIRS-runs (Φ_{Prior}).

4.3 Results

4.3.1 Global fluxes

In Figure 4.1, we see the annual sum of mean fluxes ($\overline{\Phi}_{Met}$ and $\overline{\Phi}_{AIRS}$) calculated with Equation 4.2. For comparison, we show the annual fluxes for the same year from CarbonTracker (Φ_{CT}) and the annual surface flux forcing used as a surface boundary condition in the Met and AIRS runs (Φ_{Prior}).

The surface flux forcing (Φ_{Prior}, lower right of Figure 4.1) has an annually-balanced terrestrial carbon cycle, so in this annually-summed representation, we do not see the imprint of natural terrestrial land processes, but rather just the anthropogenic signal (e.g. the sources over the Eastern United States, Europe, and Asia), and climatological ocean fluxes.

CarbonTracker's terrestrial carbon cycle is not annually-balanced, and for the year 2003, Φ_{CT} (lower left of Figure 4.1) shows a sink in the boreal forests, and a source in the Amazon.

Ocean fluxes are generally too small to be resolved in the figure's lower two panels (Φ_{CT} and Φ_{Prior}). One exception is the sink in the Arctic Ocean north of Scandinavia, which is present in varying strength in both Φ_{CT} and Φ_{Prior}. There are some annual ocean source and sink regions present in Φ_{CT} but not the climatological Φ_{Prior} and vice-versa. For example, CarbonTracker has a sink southeast of Australia that is not resolved in Φ_{Prior}, and Φ_{Prior} has a sink south of Iceland that is not resolved by the CarbonTracker ocean fluxes.

The calculated surface fluxes for both the Met- and AIRS-runs ($\overline{\Phi}_{Met}$ and $\overline{\Phi}_{AIRS}$, upper row of Figure 4.1) show similar spatial patterns to the prescribed prior flux and to CarbonTracker. The fossil fuel sources and Scandinavian Arctic Ocean sink are both present in annual $\overline{\Phi}_{Met}$ and $\overline{\Phi}_{AIRS}$. $\overline{\Phi}_{Met}$ and $\overline{\Phi}_{AIRS}$ also differ from the lower two panels in a number of ways. They show much more activity over the oceans, and wavelike features near large mountain ranges (South America, the American Rockies, and the Tibetan plateau). These oscillatory features are likely model artifacts associated with steep gradients, so they would be part of the methodological error terms, ϵ_{Met} and ϵ_{AIRS}. As expressed in equation 4.5, differences between $\overline{\Phi}_{Met}$ and Φ_{Prior} (which should be identical) are attributed to the methodological error terms ϵ_{Met}. These errors are related to shortcomings of the methodology such as the use of 6-hourly fields as discussed in section 4.4. The imprint of these errors is visible in the Φ_{AIRS} map as well. To separate the signal from the noise, we thus look at the difference between $\overline{\Phi}_{AIRS}$ and $\overline{\Phi}_{Met}$, assuming $\epsilon_{Met} \sim \epsilon_{AIRS}$. In doing so, we subtract most most methodological errors (common to both Φ_{AIRS} and Φ_{Met}) from Φ_{AIRS}, and focus on the signal related to assimilating AIRS CO_2. This difference, ${\Phi'}^{AIRS}_{2003}$, is an estimate of the 2003 carbon flux anomaly, as described in section 4.2.2.

We reiterate here that our prior forcing includes a climatological view of the ocean carbon cycle, and an annually-balanced terrestrial carbon cycle. Thus, ${\Phi'}^{AIRS}_{2003}$ should include in the ocean any sources or sinks which are not part of the climatology, and over land, should include any net land sources or sinks (for example, net sinks in forested regions). The CO_2 annual flux from CarbonTracker (Φ_{CT}) also estimates the carbon sources and sinks which are specific to 2003, so $[\Phi_{CT} - \Phi_{Prior}]$ (i.e., ${\Phi'}^{CT}_{2003}$) should share some gross features with ${\Phi'}^{AIRS}_{2003}$.

${\Phi'}^{AIRS}_{2003}$ and ${\Phi'}^{CT}_{2003}$ are shown in the top row of Figure 4.2. Our estimate (left panel), shares some features with the CarbonTracker estimate (right panel). Both show regions of more carbon outgassing (or less uptake) in the Southern Ocean in 2003 relative to the climatology. They both have negative anomalies corresponding to the boreal forest land sink, and positive anomalies in the Atlantic Ocean, extending from the east coast of North America and into the Arctic.

They also differ in several regions. While ${\Phi'}^{CT}_{2003}$ and ${\Phi'}^{AIRS}_{2003}$ match signs in the region east of the Amazon Basin (negative anomalies) and in the southern tip of South America (positive anomalies), the ${\Phi'}^{AIRS}_{2003}$ map shows large negative anomalies in the central and western Amazon Basin and in the Pacific Ocean to the west of the Amazon, whereas the same part of the Amazon in the ${\Phi'}^{CT}_{2003}$ map is a positive anomaly, and the Pacific Ocean to its west is more neutral. This region is explored in more detail in section 4.3.2.

In Figure 4.2 we also show the annual spreads in Φ_{Met} and Φ_{AIRS}. We see in both cases that the spread is minimized in the tropics, especially in the tropical oceans. This will gives us more confidence in tropical signals (e.g., the Amazon signal) as compared to mid- and high-latitude signals. The spread in Φ_{AIRS} is spatially correlated with the number of available AIRS XCO_2 soundings, which are given in the form of monthly maps of observation counts in Figure 4.3. In these observation count maps, we see that AIRS does not cover the high latitudes of the Southern Hemisphere, which leads to a large spread in Φ_{AIRS} south of 55°S. Additionally, in all months, we see the densest AIRS observation coverage in the tropical oceans. These regions correspond to minimized spread in Φ_{AIRS} in Figure 4.2.

Generally, we regard Φ'^{CT}_{2003} as the true anomaly that we hope to retrieve with our methodology. In the boreal forests, our methodology (Φ'^{AIRS}_{2003}) does not retrieve the full 2003 net carbon sink that is seen in Φ'^{CT}_{2003}. This is due to poorer AIRS XCO_2 availability in those regions and due to the vertical sensitivity of the AIRS instrument to CO_2. This sensitivity peaks in the mid- to upper-troposphere, as expressed by the averaging kernel curves in Figure 4.4. In the mid- and high-latitude regions, CO_2 at these pressure levels is advected rapidly by westerlies, so signals that we detect are likely representative of flux anomalies in a particular latitude band rather than flux anomalies of regions directly underlying the AIRS XCO_2 signals. Conversely, in the tropics, strong convective mixing allows surface flux information to propagate into the free troposphere, where AIRS has strong sensitivity to changes in CO_2 abundance. The tropics are also a region where CarbonTracker's observation network suffers from observation paucity. The combination of CT observational sparseness, strong convective mixing, and AIRS observation density leads us to believe that discrepancies between Φ'^{CT}_{2003} and Φ'^{AIRS}_{2003} in the tropics could be due to real signals that CarbonTracker does not detect.

These signals are further explored at the monthly time scale in Figure 4.5. In this case, for Φ'^{AIRS}_{2003} anomalies, we display only the significant differences, where significance is determined using a Z-test with a null hypothesis that $\overline{\Phi_{AIRS}}$ is within 1.96 x $\sigma_{\Phi,Met}$ of $\overline{\Phi_{Met}}$. As in Figure 4.2, we show the corresponding Φ'^{CT}_{2003} for each month and look for commonalities between the two. In general, we consider the right column (Φ'^{CT}_{2003}) as the target flux anomaly signal that we hope to detect, and the actual signal detected is shown in the left column (Φ'^{AIRS}_{2003}). In the tropics, however, we suspect that Φ'^{AIRS}_{2003} signals could offer some new information that Φ'^{CT}_{2003} has missed. In several months, the anomaly maps agree qualitatively on the ocean carbon cycle. For example, in August, both maps show negative anomalies in the ocean from 20°S to the equator, and mostly positive anomalies south of the negative anomalies. On land, commonalities include a positive anomaly in South Africa in February and negative anomalies in the high latitudes of the Asian continent in February and April.

Similarly to the annual map, we find the largest standout differences in the Amazon region, and in the Pacific Ocean west of it. Negative anomalies in the Φ'^{AIRS}_{2003} maps over the Amazon region are prominent from June through October. In August, the Φ'^{CT}_{2003} map shows large negative anomalies near the Amazon, but they are located east and south of the Φ'^{AIRS}_{2003}

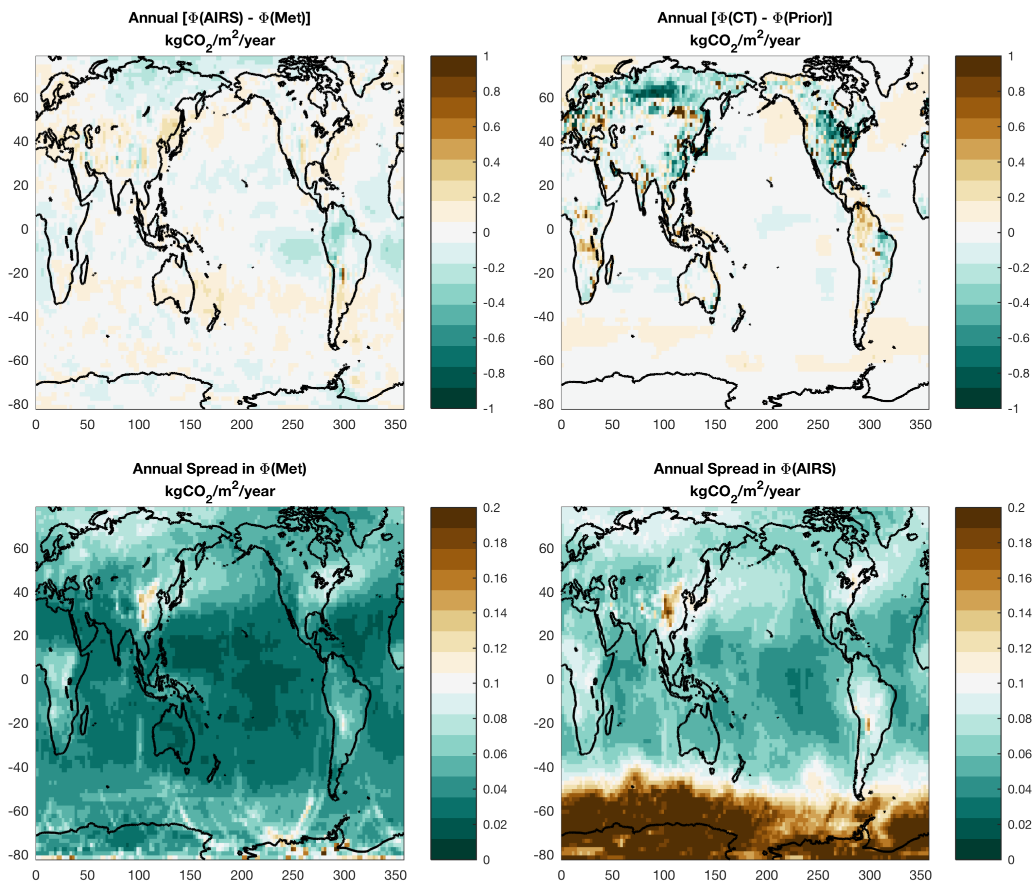

Figure 4.2: Difference in the annual CO_2 surface flux calculated using the AIRS run fields relative to the surface flux calculated using the Met run fields, $[\Phi'^{AIRS}_{2003} = \Phi_{AIRS} - \Phi_{Met}]$ (upper left panel). Difference in the annual CO_2 surface flux from CarbonTracker relative to the surface flux used as forcing in the Met and AIRS runs, $[\Phi'^{CT}_{2003} = \Phi_{CT} - \Phi_{Prior}]$ (upper right panel). Spread in annual Φ_{Met} (lower left panel) and in Φ_{AIRS} (lower right panel).

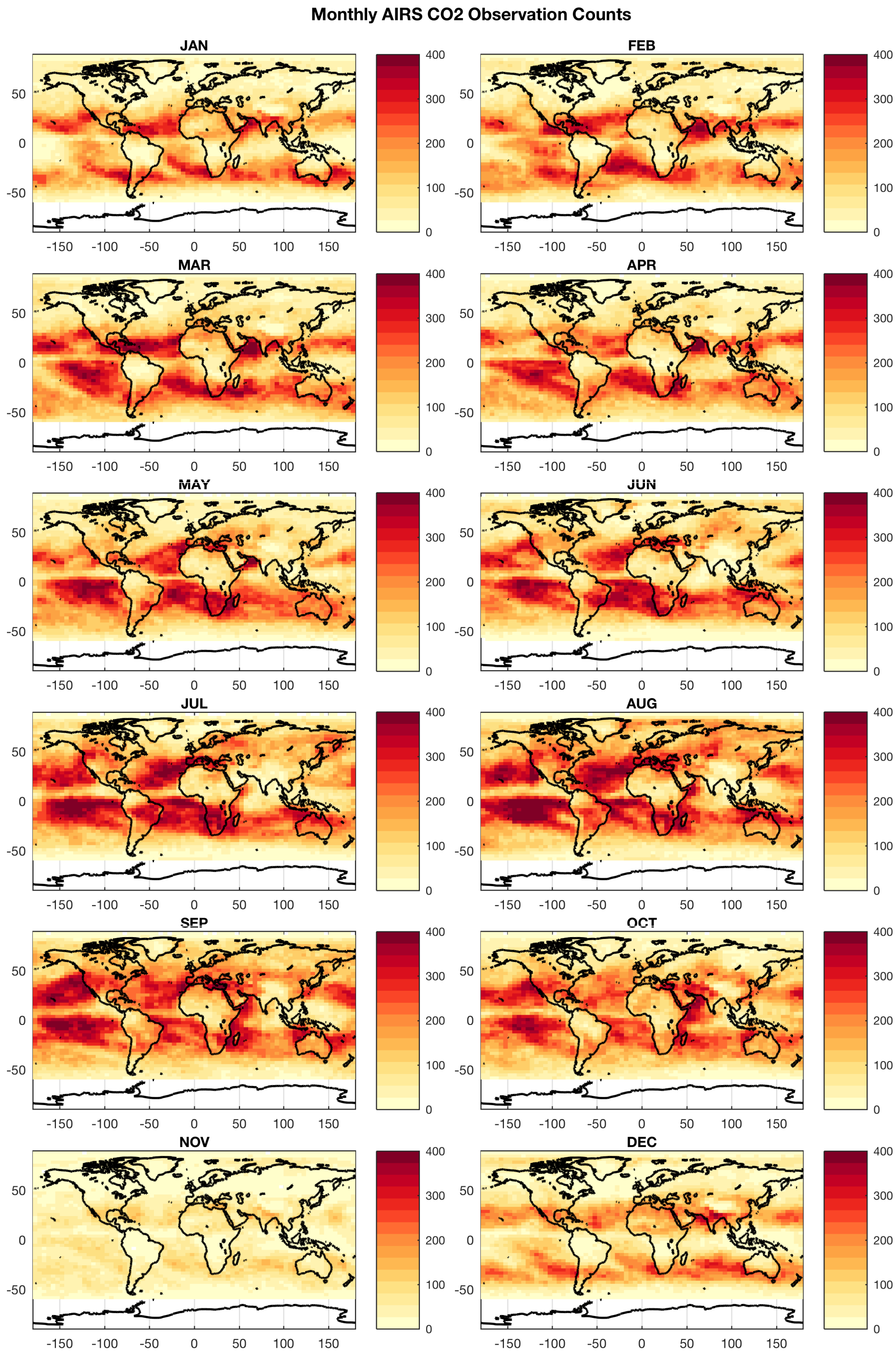

Figure 4.3: Monthly observation counts of available AIRS XCO_2 soundings falling within grid boxes of size 5° longitude x 3.75° latitude, for the year 2003.

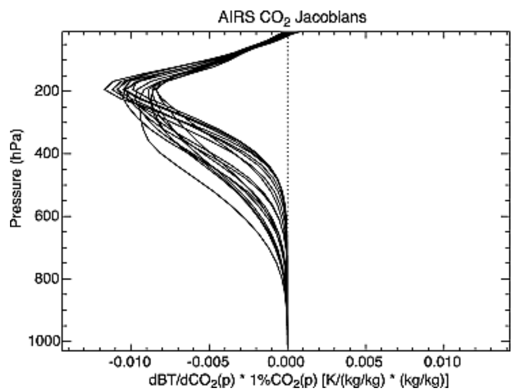

Figure 4.4: The sensitivity of AIRS to CO_2 changes as a function of atmospheric pressure, taken from Engelen and McNally (2005). The sensitivity is the change in brightness temperature (dBT) for a 1% change in CO_2 mass mixing ratio. Each curve represents the sensitivity of one of the 18 spectral channels used to determine XCO_2 from AIRS radiance observations.

anomalies, in the cerrado and agricultural region outside of the central Amazon Basin. In February and August, Φ'^{AIRS}_{2003} does not detect a signal directly where CarbonTracker finds its large negative anomaly. The Amazon flux results are further elaborated upon in section 4.3.2.

The large negative anomaly in Φ'^{AIRS}_{2003} over the ocean, downwind of the Amazon, persists from April to August, but it is only present in Φ'^{CT}_{2003} in April. This signal is one typically seen at the early stages of a large El Niño event (e.g., the 2015 El Niño, Chatterjee et al. (2017)). During an El Niño, anomalously warm water off the west coast of South America leads to suppressed upwelling and CO_2-depleted surface water, hence a negative signal (increased carbon sink, or decreased source) is expected. However, in summer 2003, conditions were normal in this region. The April signal which is present in both Φ'^{AIRS}_{2003} and Φ'^{CT}_{2003} could be related to the slight El Niño conditions of late 2002 and early 2003. Nearly neutral conditions were reached by April 2003 (Levinson and Waple 2004), so any signal after this month is likely unrelated to the El Niño. Most likely, the large negative Φ'^{AIRS}_{2003} in June and August is related to an increased sink somewhere upwind of the signal, such as the Amazon. We note here that this part of the Pacific is also a region of persistently high counts of AIRS XCO_2 soundings (as seen in Figure 4.3), so the AIRS run's CO_2 fields are expected to differ significantly from the Met run's in this region.

4.3.2 Amazon fluxes

Figure 4.6 shows our posterior CO_2 surface flux ($\Phi_{Posterior}$, from Equation 4.10) for all months for the Amazon region. It includes the prior flux forcing (Φ_{Prior}) and CarbonTracker's flux (Φ_{CT}) for comparison. We see that for the most part all three products agree on the sign of the fluxes throughout the months. In the early (wet season) months, the northern Amazon is a source of carbon to the atmosphere, and the region south and east of the basin is neutral or a sink. In the dry season months of July through September, the three agree

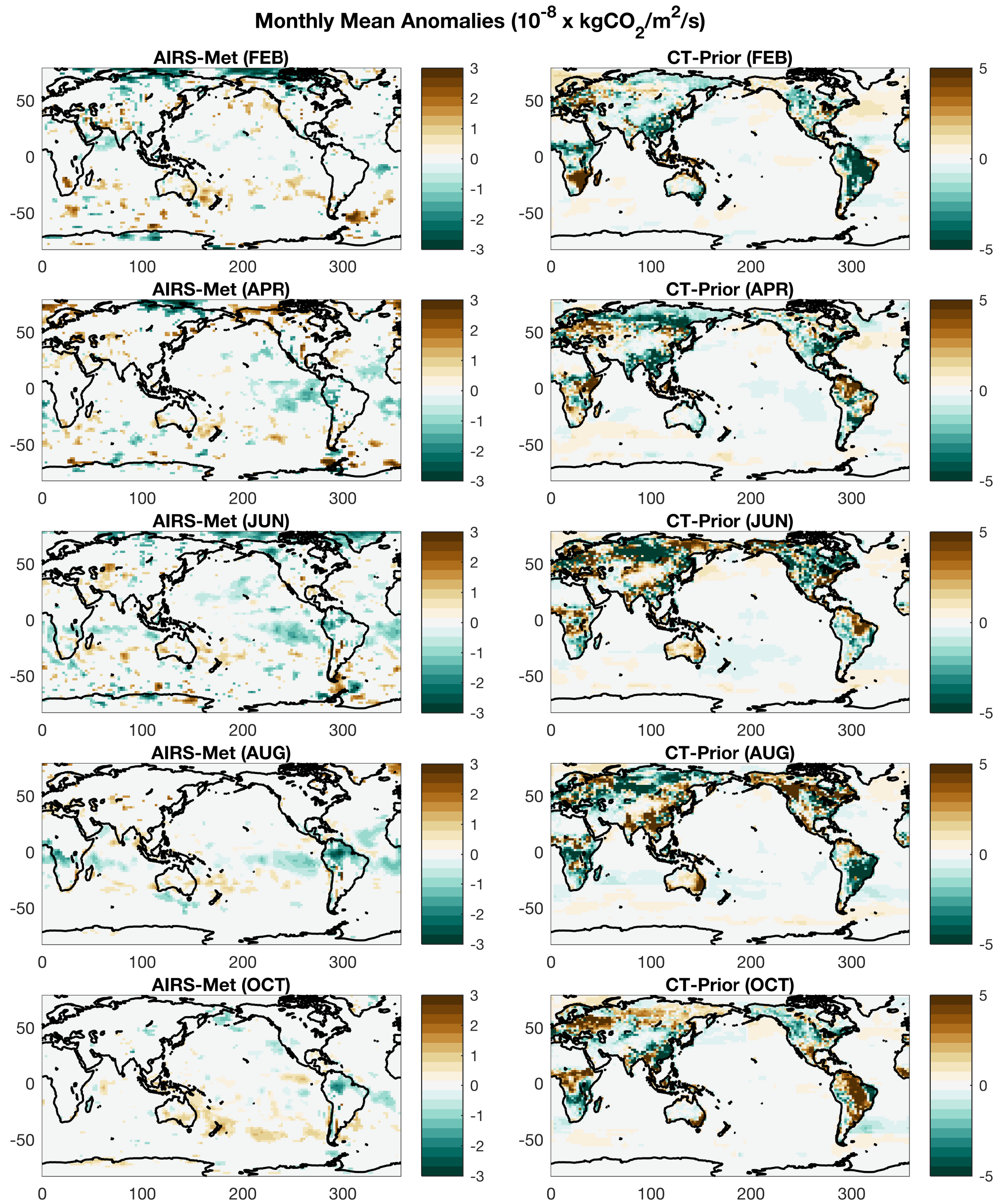

Figure 4.5: Difference in the monthly CO_2 surface flux calculated using the AIRS run fields relative to the surface flux calculated using the Met run fields, [$\Phi'^{AIRS}_{2003} = \Phi_{AIRS} - \Phi_{Met}$, our detected 2003 flux anomaly] (left column), for months February, April, June, August, and October. Difference in the monthly CO_2 surface flux from CarbonTracker relative to the surface flux used as forcing in the Met and AIRS runs, [$\Phi'^{CT}_{2003} = \Phi_{CT} - \Phi_{Prior}$, the target 2003 flux anomaly] (right column), for the same months. Left column anomaly maps only show significant differences (at the 95% confidence level).

that the north is now a sink and the shoulder region to the south and east is a source. Φ_{CT} and $\Phi_{Posterior}$ disagree in several months in terms of source/sink magnitudes, however. Our estimate has the central Amazon Basin region as a stronger sink than CarbonTracker's estimate.

The annual sum of these fluxes is shown in Figure 4.7, with a blue line marking the borders of the Amazon Basin. In addition to the annually-summed Φ_{CT}, we include the three non-ocean carbon fluxes that contribute to Φ_{CT}: the flux from the terrestrial biosphere (Φ_{CTbio}), the flux from fires (Φ_{CTfire}) and the flux from fossil fuel combustion ($\Phi_{CTfossil}$). We see that annually, much of the basin is a carbon source in Φ_{CT} but it is almost exclusively a sink in our $\Phi_{Posterior}$ estimate. Φ_{Prior} has an annually-balanced terrestrial carbon cycle, so its map is not shown. The region outside of the basin, to its south and east, has similar annual flux in both our estimate and in CarbonTracker's estimate. Most of the brown, source regions in either map fall within the "grass/shrub" ecoregion in CarbonTracker's methodology. The sink just outside of the basin (around 310°E, 5°S) is a tropical forest, the same ecoregion as the central Amazon Basin.

Grid boxes that touch the border in Figure 4.7 are summed to produce Figure 4.8, which shows the total annual carbon flux for the Amazon Basin for $\Phi_{Posterior}$, Φ_{Prior}, Φ_{CT} and Φ_{CT} components. We see that assimilating AIRS XCO_2, and calculating $\Phi_{Posterior}$ in using our mass budget method, brings the prior estimate for the region from a net source (from fossil fuel burning) to a net sink of about 0.26 PgC/year.

4.4 Discussion and Conclusions

Our results show that our carbon data assimilation system yields 4D-CO_2 and wind fields that allow for a realistic CO_2 surface flux calculation when compared with CarbonTracker fluxes. In most regions of the globe, our posterior flux estimates are closer to CarbonTracker estimates than the prior forcing was, indicating that our methodology, and assimilating AIRS XCO_2, provides useful information which can be used to inform carbon budget estimates. The most significant impact of AIRS XCO_2 on the surface flux calculation is seen in the tropics (especially the tropical oceans). Here, CO_2 surface flux signals are diluted throughout the troposphere by convective mixing, allowing AIRS to detect them with its mid-tropospheric sensitivity. These regions are also where AIRS offers its densest CO_2 soundings and where the surface flask network used by CarbonTracker has few observations.

Our estimate differs from CarbonTracker in the Amazon Basin, indicating that in 2003 there could have been a stronger carbon sink here than the CarbonTracker machinery derives. Here we estimate an annual sink of 0.26 ± 0.02 PgC/year (1-σ), while CarbonTracker estimates that this region is a source region of about the same magnitude (0.25 PgC/year). About a third of CT's annual source here is from the terrestrial biosphere (0.08 PgC/year). The data presented in Brienen et al. (2015) show that in 2003 the Amazon Basin's biomass change (carbon accumulation minus tree mortality) was a net sink, which is more aligned with our results than with CarbonTracker's.

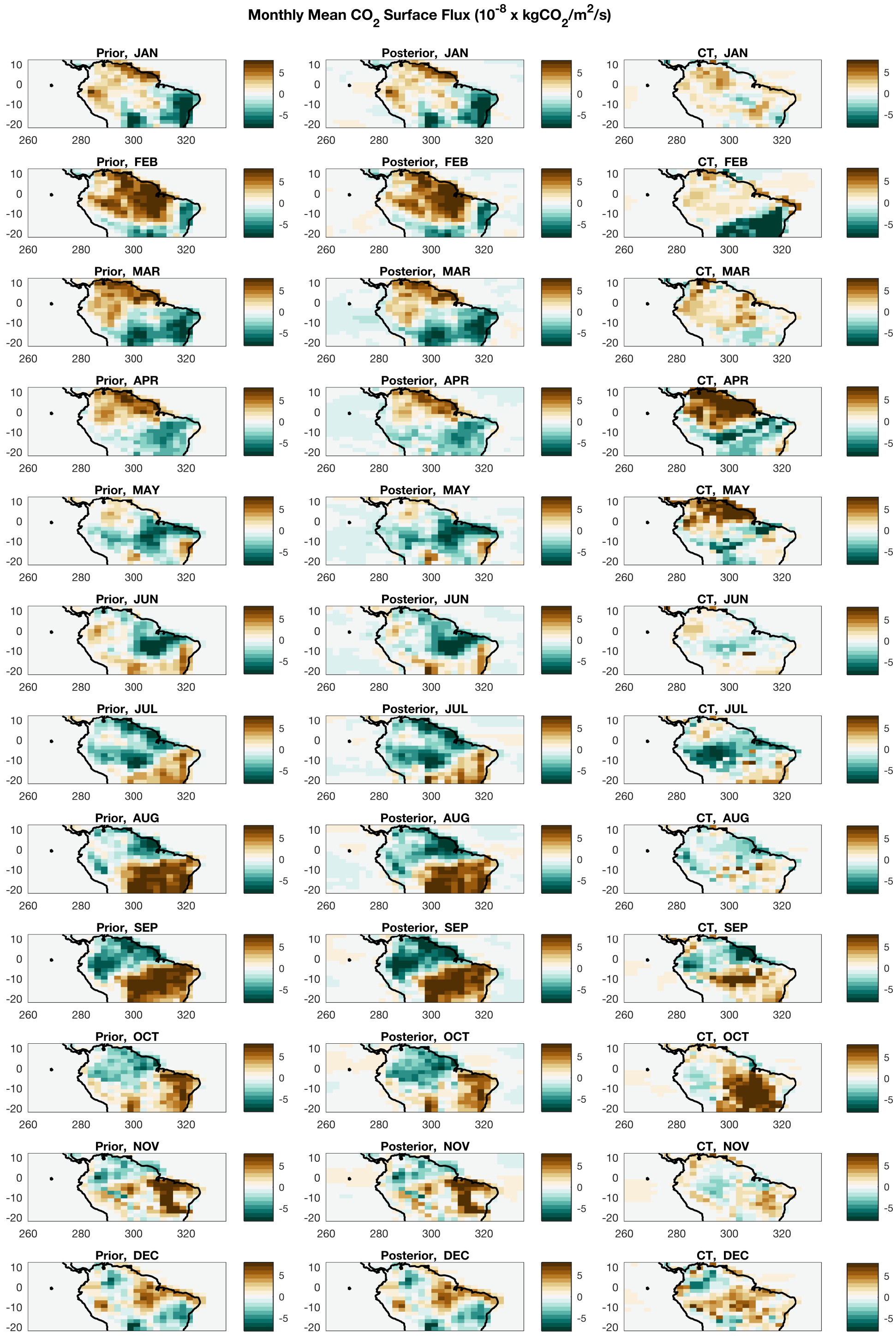

Figure 4.6: Monthly mean CO_2 surface fluxes for the year 2003 for the region containing the Amazon Basin. Left column shows Φ_{Prior}, middle column shows $\Phi_{Posterior}$, and right column shows Φ_{CT}. Flux units are 10^{-8} x kg $CO_2/m^2/s$.

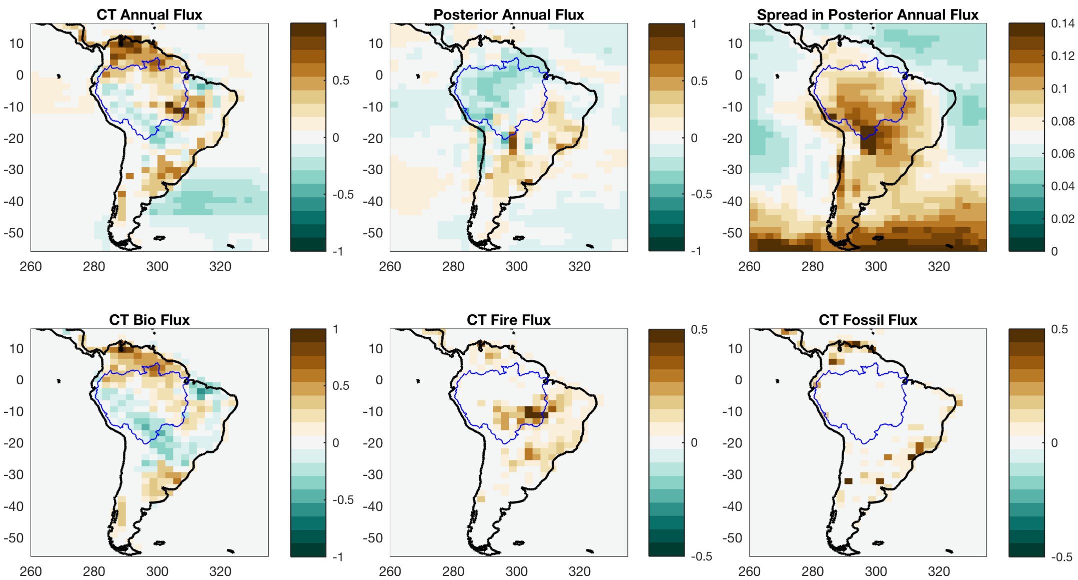

Figure 4.7: Annual sum, in $kgCO_2/m^2/year$, of monthly fluxes from CarbonTracker (upper left), and $\Phi_{Posterior}$ (upper middle). Spread in annual $\Phi_{Posterior}$ (upper right). The bottom row breaks the CT flux down into its three contributing sectors: the terrestrial biosphere (left), fires (middle), and fossil fuel (right).

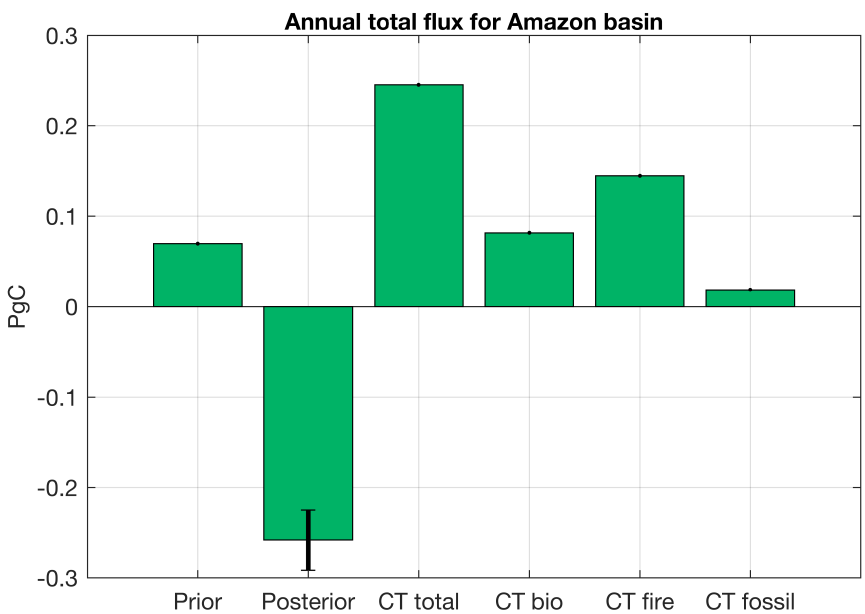

Figure 4.8: Annual carbon fluxes, in petagrams carbon, for the year 2003 for the Amazon Basin region marked in Figure 4.7. Prior is Φ_{Prior}, Posterior is $\Phi_{Posterior}$, CT total is Φ_{CT}. Also shown are the contributions from individual sectors in the CarbonTracker product: the terrestrial biosphere (CT bio), fires (CT fire), and fossil fuel combustion (CT fossil). Error bars on Posterior correspond to the ensemble spread ($\sigma_{Posterior}$).

Our posterior flux in the Amazon shows the strongest carbon uptake during dry season months of July-October. In 2003, these dry-season months correspond to the period when satellite-derived leaf area index (LAI) also peaked (Myneni et al. 2007). LAI is a proxy for gross primary productivity (GPP), so only represents one component of carbon exchange in the Amazon. Our results are aligned with either strong productivity, weak respiration, or a combination of the two, for the Amazon during dry season months, and are thus consistent with Myneni et al. (2007). They are also consistent with the idea of a "green-up" in the Amazon during the dry season, as discussed in several previous studies (Saleska et al. 2003; Huete et al. 2006).

The methodology used here is imperfect for a few reasons. First, AIRS is not sensitive to near-surface CO_2 except in the tropics, so most of our significant signals are in the tropics, and we miss information about the midlatitudes and boreal forests. This could be improved if we were to use observations from a satellite which is sensitive to surface CO_2, for example the Orbiting Carbon Observatory 2 (OCO-2) or the Greenhouse Gases Observing Satellite (GOSAT).

Additionally, there are some issues related to the data assimilation framework itself. Because we are using a finite-volume dynamical core, mass conservation is assured (Lin and Rood 1996). However, data assimilation causes air mass to be created and destroyed. On the global scale in our experiments, this is not an issue, since in our assimilation experiments, global dry air mass averaged over two weeks is conserved, with a variability of 2 x 10^{13} kg around a mean of 5.1 x 10^{18} kg air, i.e. 0.0004 %. On the scale of individual grid boxes, however, deviations from mass conservation could lead to artifacts in our calculated surface fluxes.

As mentioned previously, there are issues with using 6-hourly meteorological fields to estimate grid-box-level fluxes using equation 4.2. The nonlinear product in our calculations ($\nabla \cdot \langle \overrightarrow{u_2} \rho C \rangle$) uses the analysis smoothed to the 6-hour time window, but the meteorological fields in CAM are updated at every internal physical time step, which is of order minutes. The use of these fields smoothed or filtered over a 3- or 6-hour assimilation window appears to work well in stratospheric assimilation (Pawson et al. 2007), but is less effective when the state vector fields have diurnal variations. The use of instantaneous analysis output every 3 or 6 hours to calculate the products introduces aliasing problems (Waugh et al. 1997), even when the assimilation window is reduced to 1 hour: the product of the mean does not equal the mean of the product. This causes errors to propagate to our fluxes.

To remedy this last issue, in future experiments we can modify the CAM code to keep track of the cumulative $\nabla \cdot (\overrightarrow{u_3} \rho C)$ throughout the 6-hour assimilation window. This cumulative sum can then be integrated in the vertical (using equation 4.2) to yield a more accurate Φ for that time step. CO_2 and wind fields in each 6-hourly assimilation window would be initialized with updated states (i.e., states that were adjusted by the LETKF at the end of the previous window), then at the end of the window, a surface flux (Φ) would be calculated which is consistent with those wind and CO_2 fields. This methodology should yield similar results to the innovation approach outlined in Chapter 2 of this dissertation. In future work, these two approaches (the vertically-integrated mass budget approach and the innovation approach) should be compared using the same observations, model, and data assimilation methodology.

Bibliography

J. Anderson, T. Hoar, K. Raeder, H. Liu, N. Collins, R. Torn, and A. Avellano. The Data Assimilation Research Testbed: A community facility. *Bulletin of the American Meteorological Society*, 90(9):1283–1296, 2009. doi: 10.1175/2009BAMS2618.1. URL https://doi.org/10.1175/2009BAMS2618.1.

J. Anderson, H. Kershaw, and N. Collins. Parallel implementations of ensemble data assimilation for atmospheric prediction. In *Proceedings of the 3rd Workshop on Irregular Applications: Architectures and Algorithms*, IA3 '13, pages 12:1–12:4, New York, NY, USA, 2013. ACM. ISBN 978-1-4503-2503-5. doi: 10.1145/2535753.2535760. URL http://doi.acm.org/10.1145/2535753.2535760.

J. L. Anderson. An Ensemble Adjustment Kalman Filter for data assimilation. *Monthly Weather Review*, 129(12):2884–2903, 2001. doi: 10.1175/1520-0493(2001)129<2884:AEAKFF>2.0.CO;2. URL https://doi.org/10.1175/1520-0493(2001)129<2884:AEAKFF>2.0.CO;2.

J. L. Anderson. A local least squares framework for ensemble filtering. *Monthly Weather Review*, 131(4):634–642, 2003. doi: 10.1175/1520-0493(2003)131<0634:ALLSFF>2.0.CO;2. URL https://doi.org/10.1175/1520-0493(2003)131<0634:ALLSFF>2.0.CO;2.

J. L. Anderson. Spatially and temporally varying adaptive covariance inflation for ensemble filters. *Tellus A*, 61(1):72–83, 2009. doi: 10.1111/j.1600-0870.2008.00361.x. URL https://onlinelibrary.wiley.com/doi/abs/10.1111/j.1600-0870.2008.00361.x.

J. L. Anderson and S. L. Anderson. A Monte Carlo implementation of the nonlinear filtering problem to produce ensemble assimilations and forecasts. *Monthly Weather Review*, 127(12):2741–2758, 1999. doi: 10.1175/1520-0493(1999)127<2741:AMCIOT>2.0.CO;2. URL https://doi.org/10.1175/1520-0493(1999)127<2741:AMCIOT>2.0.CO;2.

R. J. Andres, T. A. Boden, and D. Higdon. A new evaluation of the uncertainty associated with CDIAC estimates of fossil fuel carbon dioxide emission. *Tellus B: Chemical and Physical Meteorology*, 66(1):23616, 2014. doi: 10.3402/tellusb.v66.23616. URL https://doi.org/10.3402/tellusb.v66.23616.

R. A. Anthes, P. A. Bernhardt, Y. Chen, L. Cucurull, K. F. Dymond, D. Ector, S. B. Healy, S.-P. Ho, D. C. Hunt, Y.-H. Kuo, H. Liu, K. Manning, C. McCormick, T. K. Meehan, W. J. Randel, C. Rocken, W. S. Schreiner, S. V. Sokolovskiy, S. Syndergaard, D. C. Thompson, K. E. Trenberth, T.-K. Wee, N. L. Yen, and Z. Zeng. The COSMIC/FORMOSAT-3 mission: Early results. *Bulletin of the American Meteorological Society*, 89(3):313–334,

2008. doi: 10.1175/BAMS-89-3-313. URL https://doi.org/10.1175/BAMS-89-3-313.

A. F. J. Arellano, K. Raeder, J. L. Anderson, P. G. Hess, L. K. Emmons, D. P. Edwards, G. G. Pfister, T. L. Campos, and G. W. Sachse. Evaluating model performance of an ensemble-based chemical data assimilation system during INTEX-B field mission. *Atmospheric Chemistry and Physics*, 7(21):5695–5710, 2007. doi: 10.5194/acp-7-5695-2007. URL https://www.atmos-chem-phys.net/7/5695/2007/.

S. Asefi-Najafabady, P. J. Rayner, K. R. Gurney, A. McRobert, Y. Song, K. Coltin, J. Huang, C. Elvidge, and K. Baugh. A multiyear, global gridded fossil fuel CO_2 emission data product: Evaluation and analysis of results. *Journal of Geophysical Research: Atmospheres*, 119(17):10,213–10,231, 2014. ISSN 2169-8996. doi: 10.1002/2013JD021296. URL http://dx.doi.org/10.1002/2013JD021296. 2013JD021296.

D. F. Baker, R. M. Law, K. R. Gurney, P. Rayner, P. Peylin, A. S. Denning, P. Bousquet, L. Bruhwiler, Y.-H. Chen, P. Ciais, I. Y. Fung, M. Heimann, J. John, T. Maki, S. Maksyutov, K. Masarie, M. Prather, B. Pak, S. Taguchi, and Z. Zhu. Transcom 3 inversion intercomparison: Impact of transport model errors on the interannual variability of regional CO_2 fluxes, 1988 - 2003. *Global Biogeochemical Cycles*, 20(1), 2004. doi: 10.1029/2004GB002439. URL https://agupubs.onlinelibrary.wiley.com/doi/abs/10.1029/2004GB002439.

P. S. Bakwin, P. S. Tans, C. Zhao, W. U. III, and E. Quesnell. Measurements of carbon dioxide on a very tall tower. *Tellus B: Chemical and Physical Meteorology*, 47(5):535–549, 1995. doi: 10.3402/tellusb.v47i5.16070. URL https://doi.org/10.3402/tellusb.v47i5.16070.

J. Barré, B. Gaubert, A. F. J. Arellano, H. M. Worden, D. P. Edwards, M. N. Deeter, J. L. Anderson, K. Raeder, N. Collins, S. Tilmes, G. Francis, C. Clerbaux, L. K. Emmons, G. G. Pfister, P.-F. Coheur, and D. Hurtmans. Assessing the impacts of assimilating IASI and MOPITT CO retrievals using CESM-CAM-chem and DART. *Journal of Geophysical Research: Atmospheres*, 120(19):10,501–10,529, 2015. ISSN 2169-8996. doi: 10.1002/2015JD023467. URL http://dx.doi.org/10.1002/2015JD023467. 2015JD023467.

S. Basu, S. Guerlet, A. Butz, S. Houweling, O. Hasekamp, I. Aben, P. Krummel, P. Steele, R. Langenfelds, M. Torn, S. Biraud, B. Stephens, A. Andrews, and D. Worthy. Global CO_2 fluxes estimated from gosat retrievals of total column CO_2. *Atmospheric Chemistry and Physics*, 13(17):8695–8717, 2013. doi: 10.5194/acp-13-8695-2013. URL https://www.atmos-chem-phys.net/13/8695/2013/.

P. Bauer, A. Thorpe, and G. Brunet. The quiet revolution of numerical weather prediction. *Nature*, 525:47 EP –, 09 2015. URL https://doi.org/10.1038/nature14956.

T. Borsdorff, J. Aan de Brugh, H. Hu, I. Aben, O. Hasekamp, and J. Landgraf. Measuring carbon monoxide with TROPOMI: First results and a comparison with ECMWF-IFS analysis data. *Geophysical Research Letters*, 45(6):2826–2832, 2018. doi: 10.1002/2018GL077045. URL https://agupubs.onlinelibrary.wiley.com/doi/abs/10.1002/2018GL077045.

P. Bousquet, P. Peylin, P. Ciais, C. Le Quéré, P. Friedlingstein, and P. P. Tans. Regional changes in carbon dioxide fluxes of land and oceans since 1980. *Science*, 290(5495):1342–

1346, 2000. ISSN 0036-8075. doi: 10.1126/science.290.5495.1342. URL http://science.sciencemag.org/content/290/5495/1342.

V. Brahmananda Rao, A. M. C. do Carmo, and S. H. Franchito. Interannual variations of storm tracks in the Southern Hemisphere and their connections with the Antarctic oscillation. *International Journal of Climatology*, 23(12):1537–1545, 2003. doi: 10.1002/joc.948. URL https://rmets.onlinelibrary.wiley.com/doi/abs/10.1002/joc.948.

R. J. W. Brienen, O. L. Phillips, T. R. Feldpausch, E. Gloor, T. R. Baker, J. Lloyd, G. Lopez-Gonzalez, A. Monteagudo-Mendoza, Y. Malhi, S. L. Lewis, R. Vásquez Martinez, M. Alexiades, E. Álvarez Dávila, P. Alvarez-Loayza, A. Andrade, L. E. O. C. Aragão, A. Araujo-Murakami, E. J. M. M. Arets, L. Arroyo, G. A. Aymard C., O. S. Bánki, C. Baraloto, J. Barroso, D. Bonal, R. G. A. Boot, J. L. C. Camargo, C. V. Castilho, V. Chama, K. J. Chao, J. Chave, J. A. Comiskey, F. Cornejo Valverde, L. da Costa, E. A. de Oliveira, A. Di Fiore, T. L. Erwin, S. Fauset, M. Forsthofer, D. R. Galbraith, E. S. Grahame, N. Groot, B. Hérault, N. Higuchi, E. N. Honorio Coronado, H. Keeling, T. J. Killeen, W. F. Laurance, S. Laurance, J. Licona, W. E. Magnussen, B. S. Marimon, B. H. Marimon-Junior, C. Mendoza, D. A. Neill, E. M. Nogueira, P. Núñez, N. C. Pallqui Camacho, A. Parada, G. Pardo-Molina, J. Peacock, M. Peña-Claros, G. C. Pickavance, N. C. A. Pitman, L. Poorter, A. Prieto, C. A. Quesada, F. Ramírez, H. Ramírez-Angulo, Z. Restrepo, A. Roopsind, A. Rudas, R. P. Salomão, M. Schwarz, N. Silva, J. E. Silva-Espejo, M. Silveira, J. Stropp, J. Talbot, H. ter Steege, J. Teran-Aguilar, J. Terborgh, R. Thomas-Caesar, M. Toledo, M. Torello-Raventos, R. K. Umetsu, G. M. F. van der Heijden, P. van der Hout, I. C. Guimarães Vieira, S. A. Vieira, E. Vilanova, V. A. Vos, and R. J. Zagt. Long-term decline of the Amazon carbon sink. *Nature*, 519, 2015. doi: 10.1038/nature14283. URL https://www.nature.com/articles/nature14283.

M. Buchwitz, R. de Beek, J. P. Burrows, H. Bovensmann, T. Warneke, J. Notholt, J. F. Meirink, A. P. H. Goede, P. Bergamaschi, S. Körner, M. Heimann, and A. Schulz. Atmospheric methane and carbon dioxide from SCIAMACHY satellite data: initial comparison with chemistry and transport models. *Atmospheric Chemistry and Physics*, 5(4):941–962, 2005. doi: 10.5194/acp-5-941-2005. URL https://www.atmos-chem-phys.net/5/941/2005/.

M. Chahine, C. Barnet, E. T. Olsen, L. Chen, and E. Maddy. On the determination of atmospheric minor gases by the method of vanishing partial derivatives with application to CO_2. *Geophysical Research Letters*, 32(22):n/a–n/a, 2005. ISSN 1944-8007. doi: 10.1029/2005GL024165. URL http://dx.doi.org/10.1029/2005GL024165. L22803.

A. Chatterjee, M. M. Gierach, A. J. Sutton, R. A. Feely, D. Crisp, A. Eldering, M. R. Gunson, C. W. O'Dell, B. B. Stephens, and D. S. Schimel. Influence of El Niño on atmospheric CO_2 over the tropical Pacific Ocean: Findings from NASA's OCO-2 mission. *Science*, 358(6360), 2017. ISSN 0036-8075. doi: 10.1126/science.aam5776. URL http://science.sciencemag.org/content/358/6360/eaam5776.

F. Chevallier. On the statistical optimality of CO_2 atmospheric inversions assimilating CO_2 column retrievals. *Atmospheric Chemistry and Physics*, 15(19):11133–11145, 2015. doi: 10.5194/acp-15-11133-2015. URL https://www.atmos-chem-phys.net/15/11133/2015/.

F. Chevallier, L. Feng, H. Bösch, P. I. Palmer, and P. J. Rayner. On the impact of transport model errors for the estimation of CO_2 surface fluxes from GOSAT observations. *Geophysical Research Letters*, 37(21), 2010. doi: 10.1029/2010GL044652. URL https://agupubs.onlinelibrary.wiley.com/doi/abs/10.1029/2010GL044652.

F. Chevallier, N. M. Deutscher, T. J. Conway, P. Ciais, L. Ciattaglia, S. Dohe, M. Fröhlich, A. J. Gomez-Pelaez, D. Griffith, F. Hase, L. Haszpra, P. Krummel, E. Kyrö, C. Labuschagne, R. Langenfelds, T. Machida, F. Maignan, H. Matsueda, I. Morino, J. Notholt, M. Ramonet, Y. Sawa, M. Schmidt, V. Sherlock, P. Steele, K. Strong, R. Sussmann, P. Wennberg, S. Wofsy, D. Worthy, D. Wunch, and M. Zimnoch. Global CO_2 fluxes inferred from surface air-sample measurements and from TCCON retrievals of the CO_2 total column. *Geophysical Research Letters*, 38(24), 2011. doi: 10.1029/2011GL049899. URL https://agupubs.onlinelibrary.wiley.com/doi/abs/10.1029/2011GL049899.

O. Coopmann, V. Guidard, N. Fourrié, and M. Plu. Assimilation of IASI ozone-sensitive channels in preparation for an enhanced coupling between numerical weather prediction and chemistry transport models. *Journal of Geophysical Research: Atmospheres*, 123(21):12,452–12,473, 2018. doi: 10.1029/2017JD027901. URL https://agupubs.onlinelibrary.wiley.com/doi/abs/10.1029/2017JD027901.

P. Courtier, J.-N. Thépaut, and A. Hollingsworth. A strategy for operational implementation of 4D-var. In *Workshop on Variational Assimilation, with special emphasis on Three-dimensional Aspects, 9-12 November 1992*, pages 437–464, Shinfield Park, Reading, 1992. ECMWF, ECMWF. URL https://www.ecmwf.int/node/8796.

D. Crisp, R. Atlas, F.-M. Breon, L. Brown, J. Burrows, P. Ciais, B. Connor, S. Doney, I. Fung, D. Jacob, C. Miller, D. O'Brien, S. Pawson, J. Randerson, P. Rayner, R. Salawitch, S. Sander, B. Sen, G. Stephens, P. Tans, G. Toon, P. Wennberg, S. Wofsy, Y. Yung, Z. Kuang, B. Chudasama, G. Sprague, B. Weiss, R. Pollock, D. Kenyon, and S. Schroll. The Orbiting Carbon Observatory (OCO) mission. *Advances in Space Research*, 34(4):700 – 709, 2004. ISSN 0273-1177. doi: https://doi.org/10.1016/j.asr.2003.08.062. URL http://www.sciencedirect.com/science/article/pii/S0273117704003539. Trace Constituents in the Troposphere and Lower Stratosphere.

R. J. Dargaville and I. Simmonds. *Calculating CO_2 Fluxes by Data Assimilation Coupled to a Three Dimensional Mass Balance Inversion*, pages 255–264. American Geophysical Union, 2013. ISBN 9781118664452. doi: 10.1029/GM114p0255. URL http://dx.doi.org/10.1029/GM114p0255.

F. Deng, D. B. A. Jones, D. K. Henze, N. Bousserez, K. W. Bowman, J. B. Fisher, R. Nassar, C. O'Dell, D. Wunch, P. O. Wennberg, E. A. Kort, S. C. Wofsy, T. Blumenstock, N. M. Deutscher, D. W. T. Griffith, F. Hase, P. Heikkinen, V. Sherlock, K. Strong, R. Sussmann, and T. Warneke. Inferring regional sources and sinks of atmospheric CO_2 from GOSAT XCO_2 data. *Atmospheric Chemistry and Physics*, 14(7):3703–3727, 2014. doi: 10.5194/acp-14-3703-2014. URL https://www.atmos-chem-phys.net/14/3703/2014/.

A. S. Denning, M. Holzer, K. R. Gurney, M. Heimann, R. M. Law, P. J. Rayner, I. Y. Fung, S.-M. Fan, S. Taguchi, P. Friedlingstein, Y. Balkanski, J. Taylor, M. Maiss, and I. Levin. Three-dimensional transport and concentration of SF6: A model intercomparison study

(TransCom 2). *Tellus B: Chemical and Physical Meteorology*, 51(2):266–297, 1999. doi: 10.3402/tellusb.v51i2.16286. URL https://doi.org/10.3402/tellusb.v51i2.16286.

A. Eldering, C. W. O'Dell, P. O. Wennberg, D. Crisp, M. R. Gunson, C. Viatte, C. Avis, A. Braverman, R. Castano, A. Chang, L. Chapsky, C. Cheng, B. Connor, L. Dang, G. Doran, B. Fisher, C. Frankenberg, D. Fu, R. Granat, J. Hobbs, R. A. M. Lee, L. Mandrake, J. McDuffie, C. E. Miller, V. Myers, V. Natraj, D. O'Brien, G. B. Osterman, F. Oyafuso, V. H. Payne, H. R. Pollock, I. Polonsky, C. M. Roehl, R. Rosenberg, F. Schwandner, M. Smyth, V. Tang, T. E. Taylor, C. To, D. Wunch, and J. Yoshimizu. The Orbiting Carbon Observatory-2: First 18 months of science data products. *Atmospheric Measurement Techniques*, 10(2):549–563, 2017a. doi: 10.5194/amt-10-549-2017. URL https://www.atmos-meas-tech.net/10/549/2017/.

A. Eldering, P. O. Wennberg, D. Crisp, D. S. Schimel, M. R. Gunson, A. Chatterjee, J. Liu, F. M. Schwandner, Y. Sun, C. W. O'Dell, C. Frankenberg, T. Taylor, B. Fisher, G. B. Osterman, D. Wunch, J. Hakkarainen, J. Tamminen, and B. Weir. The Orbiting Carbon Observatory-2: Early science investigations of regional carbon dioxide fluxes. *Science*, 358 (6360), 2017b. ISSN 0036-8075. doi: 10.1126/science.aam5745. URL http://science.sciencemag.org/content/358/6360/eaam5745.

R. J. Engelen and A. P. McNally. Estimating atmospheric CO_2 from advanced infrared satellite radiances within an operational four-dimensional variational (4D-Var) data assimilation system: Results and validation. *Journal of Geophysical Research: Atmospheres*, 110(D18), 2005. doi: 10.1029/2005JD005982. URL https://agupubs.onlinelibrary.wiley.com/doi/abs/10.1029/2005JD005982.

G. Evensen. The Ensemble Kalman Filter: Theoretical formulation and practical implementation. *Ocean Dynamics*, 53(4):343–367, Nov 2003. ISSN 1616-7228. doi: 10.1007/s10236-003-0036-9. URL https://doi.org/10.1007/s10236-003-0036-9.

L. Feng, P. I. Palmer, H. Bösch, and S. Dance. Estimating surface CO_2 fluxes from space-borne CO_2 dry air mole fraction observations using an ensemble Kalman Filter. *Atmospheric Chemistry and Physics*, 9(8):2619–2633, 2009. doi: 10.5194/acp-9-2619-2009. URL https://www.atmos-chem-phys.net/9/2619/2009/.

G. Gaspari and S. E. Cohn. Construction of correlation functions in two and three dimensions. *Quarterly Journal of the Royal Meteorological Society*, 125(554):723–757, 1999. ISSN 1477-870X. doi: 10.1002/qj.49712555417. URL http://dx.doi.org/10.1002/qj.49712555417.

B. Gaubert, A. F. Arellano Jr., J. Barré, H. M. Worden, L. K. Emmons, S. Tilmes, R. R. Buchholz, F. Vitt, K. Raeder, N. Collins, J. L. Anderson, C. Wiedinmyer, S. Martinez Alonso, D. P. Edwards, M. O. Andreae, J. W. Hannigan, C. Petri, K. Strong, and N. Jones. Toward a chemical reanalysis in a coupled chemistry-climate model: An evaluation of MOPITT CO assimilation and its impact on tropospheric composition. *Journal of Geophysical Research: Atmospheres*, 121(12):7310–7343, 2016. doi: 10.1002/2016JD024863. URL https://agupubs.onlinelibrary.wiley.com/doi/abs/10.1002/2016JD024863.

D. Guan, Z. Liu, Y. Geng, S. Lindner, and K. Hubacek. The gigatonne gap in China's carbon dioxide inventories. *Nature Climate Change*, 2:672 EP –, 06 2012. doi: 10.1038/nclimate1560. URL http://dx.doi.org/10.1038/nclimate1560.

K. R. Gurney, R. M. Law, A. S. Denning, P. J. Rayner, D. Baker, P. Bousquet, L. Bruhwiler, Y.-H. Chen, P. Ciais, S. Fan, I. Y. Fung, M. Gloor, M. Heimann, K. Higuchi, J. John, E. Kowalczyk, T. Maki, S. Maksyutov, P. Peylin, M. Prather, B. C. Pak, J. Sarmiento, S. Taguchi, T. Takahashi, and C.-W. Yuen. TransCom 3 CO_2 inversion intercomparison: 1. Annual mean control results and sensitivity to transport and prior flux information. *Tellus B: Chemical and Physical Meteorology*, 55(2):555–579, 2003. doi: 10.3402/tellusb.v55i2.16728. URL https://doi.org/10.3402/tellusb.v55i2.16728.

J. Hakkarainen, I. Ialongo, and J. Tamminen. Direct space-based observations of anthropogenic CO_2 emission areas from OCO-2. *Geophysical Research Letters*, 43(21):11,400–11,406, 2016. ISSN 1944-8007. doi: 10.1002/2016GL070885. URL http://dx.doi.org/10.1002/2016GL070885. 2016GL070885.

S. Houweling, I. Aben, F.-M. Breon, F. Chevallier, N. Deutscher, R. Engelen, C. Gerbig, D. Griffith, K. Hungershoefer, R. Macatangay, J. Marshall, J. Notholt, W. Peters, and S. Serrar. The importance of transport model uncertainties for the estimation of CO_2 sources and sinks using satellite measurements. *Atmospheric Chemistry and Physics*, 10(20):9981–9992, 2010. doi: 10.5194/acp-10-9981-2010. URL https://www.atmos-chem-phys.net/10/9981/2010/.

S. Houweling, D. Baker, S. Basu, H. Boesch, A. Butz, F. Chevallier, F. Deng, E. J. Dlugokencky, L. Feng, A. Ganshin, O. Hasekamp, D. Jones, S. Maksyutov, J. Marshall, T. Oda, C. W. O'Dell, S. Oshchepkov, P. I. Palmer, P. Peylin, Z. Poussi, F. Reum, H. Takagi, Y. Yoshida, and R. Zhuravlev. An intercomparison of inverse models for estimating sources and sinks of CO_2 using GOSAT measurements. *Journal of Geophysical Research: Atmospheres*, 120(10):5253–5266, 2015. doi: 10.1002/2014JD022962. URL https://agupubs.onlinelibrary.wiley.com/doi/abs/10.1002/2014JD022962.

A. R. Huete, K. Didan, Y. E. Shimabukuro, P. Ratana, S. R. Saleska, L. R. Hutyra, W. Yang, R. R. Nemani, and R. Myneni. Amazon rainforests green-up with sunlight in dry season. *Geophysical Research Letters*, 33(6), 2006. doi: 10.1029/2005GL025583. URL https://agupubs.onlinelibrary.wiley.com/doi/abs/10.1029/2005GL025583.

B. Hunt, E. Kalnay, E. Kostelich, E. Ott, D. Patil, T. Sauer, I. Szunyogh, J. Yorke, and A. Zimin. Four-dimensional ensemble Kalman filtering. *Tellus A: Dynamic Meteorology and Oceanography*, 56(4):273–277, 2004. doi: 10.3402/tellusa.v56i4.14424. URL https://doi.org/10.3402/tellusa.v56i4.14424.

B. R. Hunt, E. J. Kostelich, and I. Szunyogh. Efficient data assimilation for spatiotemporal chaos: A local ensemble transform Kalman filter. *Physica D: Nonlinear Phenomena*, 230(1):112 – 126, 2007. ISSN 0167-2789. doi: https://doi.org/10.1016/j.physd.2006.11.008. URL http://www.sciencedirect.com/science/article/pii/S0167278906004647. Data Assimilation.

F. Joos and R. Spahni. Rates of change in natural and anthropogenic radiative forcing over the past 20,000 years. *Proceedings of the National Academy of Sciences*, 105(5):1425–1430, 2008. ISSN 0027-8424. doi: 10.1073/pnas.0707386105. URL https://www.pnas.

org/content/105/5/1425.

E. Kalnay. *Atmospheric modeling, data assimilation and predictability*. Cambridge University Press, New York, 2003. ISBN 978-0-521-79179-3.

M. Kanamitsu, W. Ebisuzaki, J. Woollen, S.-K. Yang, J. J. Hnilo, M. Fiorino, and G. L. Potter. NCEP-DOE AMIP-II Reanalysis (R-2). *Bulletin of the American Meteorological Society*, 83(11):1631–1644, 2002. doi: 10.1175/BAMS-83-11-1631. URL https://doi.org/10.1175/BAMS-83-11-1631.

J.-S. Kang, E. Kalnay, J. Liu, I. Fung, T. Miyoshi, and K. Ide. "Variable localization" in an ensemble Kalman filter: Application to the carbon cycle data assimilation. *Journal of Geophysical Research: Atmospheres*, 116(D9):n/a–n/a, 2011. ISSN 2156-2202. doi: 10.1029/2010JD014673. URL http://dx.doi.org/10.1029/2010JD014673. D09110.

J.-S. Kang, E. Kalnay, T. Miyoshi, J. Liu, and I. Fung. Estimation of surface carbon fluxes with an advanced data assimilation methodology. *Journal of Geophysical Research: Atmospheres*, 117(D24):n/a–n/a, 2012. ISSN 2156-2202. doi: 10.1029/2012JD018259. URL http://dx.doi.org/10.1029/2012JD018259. D24101.

S. R. Kawa, J. Mao, J. B. Abshire, G. J. Collatz, X. Sun, and C. J. Weaver. Simulation studies for a space-based CO_2 lidar mission. *Tellus B: Chemical and Physical Meteorology*, 62(5):759–769, 2010. doi: 10.1111/j.1600-0889.2010.00486.x. URL https://doi.org/10.1111/j.1600-0889.2010.00486.x.

C. D. Keeling, J. A. Adams Jr., C. A. Ekdahl Jr., and P. R. Guenther. Atmospheric carbon dioxide variations at the South Pole. *Tellus*, 28(6):552–564, 1976a. doi: 10.1111/j.2153-3490.1976.tb00702.x. URL https://onlinelibrary.wiley.com/doi/abs/10.1111/j.2153-3490.1976.tb00702.x.

C. D. Keeling, R. B. Bacastow, A. E. Bainbridge, C. A. E. Jr., P. R. Guenther, L. S. Waterman, and J. F. S. Chin. Atmospheric carbon dioxide variations at Mauna Loa Observatory, Hawaii. *Tellus*, 28(6):538–551, 1976b. doi: 10.3402/tellusa.v28i6.11322. URL https://doi.org/10.3402/tellusa.v28i6.11322.

J. I. Korsbakken, G. P. Peters, and R. M. Andrew. Uncertainties around reductions in China's coal use and CO_2 emissions. *Nature Climate Change*, 6:687 EP –, 03 2016. URL http://dx.doi.org/10.1038/nclimate2963.

S. S. Kulawik, D. B. A. Jones, R. Nassar, F. W. Irion, J. R. Worden, K. W. Bowman, T. Machida, H. Matsueda, Y. Sawa, S. C. Biraud, M. L. Fischer, and A. R. Jacobson. Characterization of Tropospheric Emission Spectrometer (TES) CO_2 for carbon cycle science. *Atmospheric Chemistry and Physics*, 10(12):5601–5623, 2010. doi: 10.5194/acp-10-5601-2010. URL https://www.atmos-chem-phys.net/10/5601/2010/.

A. Kuze, H. Suto, K. Shiomi, S. Kawakami, M. Tanaka, Y. Ueda, A. Deguchi, J. Yoshida, Y. Yamamoto, F. Kataoka, T. E. Taylor, and H. L. Buijs. Update on GOSAT TANSO-FTS performance, operations, and data products after more than 6 years in space. *Atmospheric Measurement Techniques*, 9(6):2445–2461, 2016. doi: 10.5194/amt-9-2445-2016. URL https://www.atmos-meas-tech.net/9/2445/2016/.

J. K. Lazo, R. E. Morss, and J. L. Demuth. 300 billion served: Sources, perceptions, uses, and values of weather forecasts. *Bulletin of the American Meteorological Society*, 90(6):785–798, 2009. doi: 10.1175/2008BAMS2604.1. URL https://doi.org/10.1175/2008BAMS2604.1.

C. Le Quéré, R. M. Andrew, J. G. Canadell, S. Sitch, J. I. Korsbakken, G. P. Peters, A. C. Manning, T. A. Boden, P. P. Tans, R. A. Houghton, R. F. Keeling, S. Alin, O. D. Andrews, P. Anthoni, L. Barbero, L. Bopp, F. Chevallier, L. P. Chini, P. Ciais, K. Currie, C. Delire, S. C. Doney, P. Friedlingstein, T. Gkritzalis, I. Harris, J. Hauck, V. Haverd, M. Hoppema, K. Klein Goldewijk, A. K. Jain, E. Kato, A. Körtzinger, P. Landschützer, N. Lefèvre, A. Lenton, S. Lienert, D. Lombardozzi, J. R. Melton, N. Metzl, F. Millero, P. M. S. Monteiro, D. R. Munro, J. E. M. S. Nabel, S.-I. Nakaoka, K. O'Brien, A. Olsen, A. M. Omar, T. Ono, D. Pierrot, B. Poulter, C. Rödenbeck, J. Salisbury, U. Schuster, J. Schwinger, R. Séférian, I. Skjelvan, B. D. Stocker, A. J. Sutton, T. Takahashi, H. Tian, B. Tilbrook, I. T. van der Laan-Luijkx, G. R. van der Werf, N. Viovy, A. P. Walker, A. J. Wiltshire, and S. Zaehle. Global carbon budget 2016. *Earth System Science Data*, 8(2):605–649, 2016. doi: 10.5194/essd-8-605-2016. URL https://www.earth-syst-sci-data.net/8/605/2016/.

C. Le Quéré, R. M. Andrew, P. Friedlingstein, S. Sitch, J. Hauck, J. Pongratz, P. A. Pickers, J. I. Korsbakken, G. P. Peters, J. G. Canadell, A. Arneth, V. K. Arora, L. Barbero, A. Bastos, L. Bopp, F. Chevallier, L. P. Chini, P. Ciais, S. C. Doney, T. Gkritzalis, D. S. Goll, I. Harris, V. Haverd, F. M. Hoffman, M. Hoppema, R. A. Houghton, G. Hurtt, T. Ilyina, A. K. Jain, T. Johannessen, C. D. Jones, E. Kato, R. F. Keeling, K. K. Goldewijk, P. Landschützer, N. Lefèvre, S. Lienert, Z. Liu, D. Lombardozzi, N. Metzl, D. R. Munro, J. E. M. S. Nabel, S.-I. Nakaoka, C. Neill, A. Olsen, T. Ono, P. Patra, A. Peregon, W. Peters, P. Peylin, B. Pfeil, D. Pierrot, B. Poulter, G. Rehder, L. Resplandy, E. Robertson, M. Rocher, C. Rödenbeck, U. Schuster, J. Schwinger, R. Séférian, I. Skjelvan, T. Steinhoff, A. Sutton, P. P. Tans, H. Tian, B. Tilbrook, F. N. Tubiello, I. T. van der Laan-Luijkx, G. R. van der Werf, N. Viovy, A. P. Walker, A. J. Wiltshire, R. Wright, S. Zaehle, and B. Zheng. Global carbon budget 2018. *Earth System Science Data*, 10(4):2141–2194, 2018. doi: 10.5194/essd-10-2141-2018. URL https://www.earth-syst-sci-data.net/10/2141/2018/.

C. Le Quéré, M. R. Raupach, J. G. Canadell, G. Marland, L. Bopp, P. Ciais, T. J. Conway, S. C. Doney, R. A. Feely, P. Foster, P. Friedlingstein, K. Gurney, R. A. Houghton, J. I. House, C. Huntingford, P. E. Levy, M. R. Lomas, J. Majkut, N. Metzl, J. P. Ometto, G. P. Peters, I. C. Prentice, J. T. Randerson, S. W. Running, J. L. Sarmiento, U. Schuster, S. Sitch, T. Takahashi, N. Viovy, G. R. van der Werf, and F. I. Woodward. Trends in the sources and sinks of carbon dioxide. *Nature Geoscience*, 2:831– 836, 2009. doi: 10.1038/ngeo689. URL https://doi.org/10.1038/ngeo689.

D. H. Levinson and A. M. Waple. State of the climate in 2003. *Bulletin of the American Meteorological Society*, 85(6s):S1–S72, 2004. doi: 10.1175/1520-0477-85.6s.S1. URL https://doi.org/10.1175/1520-0477-85.6s.S1.

H. Li, E. Kalnay, and T. Miyoshi. Simultaneous estimation of covariance inflation and observation errors within an ensemble Kalman filter. *Quarterly Journal of the Royal Meteorological Society*, 135(639):523–533, 2009. doi: 10.1002/qj.371. URL https://rmets.onlinelibrary.wiley.com/doi/abs/10.1002/qj.371.

S.-J. Lin and R. B. Rood. Multidimensional flux-form semi-Lagrangian transport schemes. *Monthly Weather Review*, 124(9):2046–2070, 1996. doi: 10.1175/1520-0493(1996)124<2046:MFFSLT>2.0.CO;2. URL https://doi.org/10.1175/1520-0493(1996)124<2046:MFFSLT>2.0.CO;2.

J. Liu, I. Fung, E. Kalnay, and J.-S. Kang. CO_2 transport uncertainties from the uncertainties in meteorological fields. *Geophysical Research Letters*, 38(12):n/a–n/a, 2011. ISSN 1944-8007. doi: 10.1029/2011GL047213. URL http://dx.doi.org/10.1029/2011GL047213. L12808.

J. Liu, I. Fung, E. Kalnay, J.-S. Kang, E. T. Olsen, and L. Chen. Simultaneous assimilation of AIRS XCO_2 and meteorological observations in a carbon climate model with an ensemble Kalman filter. *Journal of Geophysical Research: Atmospheres*, 117(D5):n/a–n/a, 2012. ISSN 2156-2202. doi: 10.1029/2011JD016642. URL http://dx.doi.org/10.1029/2011JD016642. D05309.

J. Liu, K. W. Bowman, and M. Lee. Comparison between the Local Ensemble Transform Kalman Filter (LETKF) and 4D-Var in atmospheric CO_2 flux inversion with the Goddard Earth Observing System-Chem model and the observation impact diagnostics from the LETKF. *Journal of Geophysical Research: Atmospheres*, 121(21):13,066–13,087, 2016. doi: 10.1002/2016JD025100. URL https://agupubs.onlinelibrary.wiley.com/doi/abs/10.1002/2016JD025100.

J. Liu, K. W. Bowman, D. S. Schimel, N. C. Parazoo, Z. Jiang, M. Lee, A. A. Bloom, D. Wunch, C. Frankenberg, Y. Sun, C. W. O'Dell, K. R. Gurney, D. Menemenlis, M. Gierach, D. Crisp, and A. Eldering. Contrasting carbon cycle responses of the tropical continents to the 2015–2016 El Niño. *Science*, 358(6360), 2017a. ISSN 0036-8075. doi: 10.1126/science.aam5690. URL http://science.sciencemag.org/content/358/6360/eaam5690.

X. Liu, A. P. Mizzi, J. L. Anderson, I. Y. Fung, and R. C. Cohen. Assimilation of satellite NO_2 observations at high spatial resolution using OSSEs. *Atmospheric Chemistry and Physics*, 17(11):7067–7081, 2017b. doi: 10.5194/acp-17-7067-2017. URL https://www.atmos-chem-phys.net/17/7067/2017/.

Y. Liu, E. Kalnay, N. Zeng, G. Asrar, Z. Chen, and B. Jia. Estimating surface carbon fluxes based on a Local Ensemble Transform Kalman Filter with a short assimilation window and a long observation window. *Geoscientific Model Development Discussions*, 2017:1–32, 2017c. doi: 10.5194/gmd-2017-269. URL https://www.geosci-model-dev-discuss.net/gmd-2017-269/.

Z. Liu, D. Guan, W. Wei, S. J. Davis, P. Ciais, J. Bai, S. Peng, Q. Zhang, K. Hubacek, G. Marland, R. J. Andres, D. Crawford-Brown, J. Lin, H. Zhao, C. Hong, T. A. Boden, K. Feng, G. P. Peters, F. Xi, J. Liu, Y. Li, Y. Zhao, N. Zeng, and K. He. Reduced carbon emission estimates from fossil fuel combustion and cement production in China. *Nature*, 524:335 EP –, 08 2015. URL http://dx.doi.org/10.1038/nature14677.

G. Liuzzi, G. Masiello, C. Serio, S. Venafra, and C. Camy-Peyret. Physical inversion of the full IASI spectra: Assessment of atmospheric parameters retrievals, consistency of spectroscopy and forward modelling. *Journal of Quantitative Spectroscopy* *and Radiative Transfer*, 182:128 – 157, 2016. ISSN 0022-4073. doi: https://doi.org/10.1016/j.jqsrt.2016.05.022. URL http://www.sciencedirect.com/science/article/pii/S0022407316301248.

T. Miyoshi and S. Yamane. Local Ensemble Transform Kalman Filtering with an AGCM at a T159/L48 resolution. *Monthly Weather Review*, 135(11):3841–3861, 2007. doi: 10.1175/2007MWR1873.1. URL https://doi.org/10.1175/2007MWR1873.1.

R. B. Myneni, W. Yang, R. R. Nemani, A. R. Huete, R. E. Dickinson, Y. Knyazikhin, K. Didan, R. Fu, R. I. Negrón Juárez, S. S. Saatchi, H. Hashimoto, K. Ichii, N. V. Shabanov, B. Tan, P. Ratana, J. L. Privette, J. T. Morisette, E. F. Vermote, D. P. Roy, R. E. Wolfe, M. A. Friedl, S. W. Running, P. Votava, N. El-Saleous, S. Devadiga, Y. Su, and V. V. Salomonson. Large seasonal swings in leaf area of Amazon rainforests. *Proceedings of the National Academy of Sciences*, 104(12):4820–4823, 2007. ISSN 0027-8424. doi: 10.1073/pnas.0611338104. URL http://www.pnas.org/content/104/12/4820.

R. Nassar, D. B. A. Jones, S. S. Kulawik, J. R. Worden, K. W. Bowman, R. J. Andres, P. Suntharalingam, J. M. Chen, C. A. M. Brenninkmeijer, T. J. Schuck, T. J. Conway, and D. E. Worthy. Inverse modeling of CO_2 sources and sinks using satellite observations of CO_2 from TES and surface flask measurements. *Atmospheric Chemistry and Physics*, 11(12):6029–6047, 2011. doi: 10.5194/acp-11-6029-2011. URL https://www.atmos-chem-phys.net/11/6029/2011/.

R. Nassar, T. G. Hill, C. A. McLinden, D. Wunch, D. B. A. Jones, and D. Crisp. Quantifying CO_2 emissions from individual power plants from space. *Geophysical Research Letters*, 44 (19):10,045–10,053, 2017. ISSN 1944-8007. doi: 10.1002/2017GL074702. URL http://dx.doi.org/10.1002/2017GL074702. 2017GL074702.

National Research Council. *Verifying Greenhouse Gas Emissions: Methods to Support International Climate Agreements*. The National Academies Press, Washington, DC, 2010. ISBN 978-0-309-15211-2. doi: 10.17226/12883. URL https://dx.doi.org/10.17226/12883.

R. B. Neale, C.-C. Chen, A. Gettelman, P. H. Lauritzen, S. Park, and D. L. Williamson. Description of the NCAR Community Atmosphere Model (CAM 5.0). Technical Report Rapport 771060002, National Center for Atmospheric Research (NCAR), Boulder, CO, November 2012. URL http://www.cesm.ucar.edu/models/cesm1.0/cam/docs/description/cam5_desc.pdf.

R. R. Nelson, D. Crisp, L. E. Ott, and C. W. O'Dell. High-accuracy measurements of total column water vapor from the Orbiting Carbon Observatory-2. *Geophysical Research Letters*, 43(23):12,261–12,269, 2016. doi: 10.1002/2016GL071200. URL https://agupubs.onlinelibrary.wiley.com/doi/abs/10.1002/2016GL071200.

D. M. O'Brien, R. M. Mitchell, S. A. English, and G. A. Da Costa. Airborne measurements of air mass from O2 A-Band absorption spectra. *Journal of Atmospheric and Oceanic Technology*, 15(6):1272–1286, 1998. doi: 10.1175/1520-0426(1998)015<1272:AMOAMF>2.0.CO;2. URL https://doi.org/10.1175/1520-0426(1998)015<1272:AMOAMF>2.0.CO;2.

T. Oda and S. Maksyutov. A very high-resolution (1 km x km) global fossil fuel CO_2 emission inventory derived using a point source database and satellite observations of nighttime lights. *Atmospheric Chemistry and Physics*, 11(2):543–556, 2011. doi: 10.5194/acp-11-543-2011. URL https://www.atmos-chem-phys.net/11/543/2011/.

C. W. O'Dell, B. Connor, H. Bösch, D. O'Brien, C. Frankenberg, R. Castano, M. Christi, D. Eldering, B. Fisher, M. Gunson, J. McDuffie, C. E. Miller, V. Natraj, F. Oyafuso, I. Polonsky, M. Smyth, T. Taylor, G. C. Toon, P. O. Wennberg, and D. Wunch. The ACOS CO_2 retrieval algorithm part 1: Description and validation against synthetic observations. *Atmospheric Measurement Techniques*, 5(1):99–121, 2012. doi: 10.5194/amt-5-99-2012. URL https://www.atmos-meas-tech.net/5/99/2012/.

J. Olivier, A. Bouwman, C. Maas, J. van der, Berdowski, C. Veldt, J. Bloos, A. Visschedijk, P. Z. PYJ, and J. Haverlag. Description of EDGAR Version 2.0: A set of global emission inventories of greenhouse gases and ozone-depleting substances for all anthropogenic and most natural sources on a per country basis and on 1 degree x 1 degree grid. Technical Report Rapport 771060002, National Institute of Public Health and the Environment (RIVM), Bilthoven, The Netherlands, December 1996. URL https://www.rivm.nl/dsresource?objectid=8de22f06-60db-491b-beb1-44a80e633013&type=org&disposition=inline.

J. G. J. Olivier, J. A. V. Aardenne, F. J. Dentener, V. Pagliari, L. N. Ganzeveld, and J. A. H. W. Peters. Recent trends in global greenhouse gas emissions: regional trends 1970–2000 and spatial distribution of key sources in 2000. *Environmental Sciences*, 2(2-3):81–99, 2005. doi: 10.1080/15693430500400345. URL https://doi.org/10.1080/15693430500400345.

Y. Pan, R. A. Birdsey, J. Fang, R. Houghton, P. E. Kauppi, W. A. Kurz, O. L. Phillips, A. Shvidenko, S. L. Lewis, J. G. Canadell, P. Ciais, R. B. Jackson, S. W. Pacala, A. D. McGuire, S. Piao, A. Rautiainen, S. Sitch, and D. Hayes. A large and persistent carbon sink in the world's forests. *Science*, 333(6045):988–993, 2011. ISSN 0036-8075. doi: 10.1126/science.1201609. URL http://science.sciencemag.org/content/333/6045/988.

S. Pawson, I. Stajner, S. R. Kawa, H. Hayashi, W.-W. Tan, J. E. Nielsen, Z. Zhu, L.-P. Chang, and N. J. Livesey. Stratospheric transport using 6-h-averaged winds from a data assimilation system. *Journal of Geophysical Research: Atmospheres*, 112(D23), 2007. doi: 10.1029/2006JD007673. URL https://agupubs.onlinelibrary.wiley.com/doi/abs/10.1029/2006JD007673.

W. Peters, J. B. Miller, J. Whitaker, A. S. Denning, A. Hirsch, M. C. Krol, D. Zupanski, L. Bruhwiler, and P. P. Tans. An ensemble data assimilation system to estimate CO_2 surface fluxes from atmospheric trace gas observations. *Journal of Geophysical Research: Atmospheres*, 110(D24), 2005. doi: 10.1029/2005JD006157. URL https://agupubs.onlinelibrary.wiley.com/doi/abs/10.1029/2005JD006157.

W. Peters, A. R. Jacobson, C. Sweeney, A. E. Andrews, T. J. Conway, K. Masarie, J. B. Miller, L. M. P. Bruhwiler, G. Pétron, A. I. Hirsch, D. E. J. Worthy, G. R. van der Werf, J. T. Randerson, P. O. Wennberg, M. C. Krol, and P. P. Tans. An atmospheric perspective on North American carbon dioxide exchange: CarbonTracker. *Proceedings of the National Academy of Sciences*, 104(48):18925–18930, 2007. ISSN 0027-8424. doi: 10.1073/pnas.0708986104. URL http://www.pnas.org/content/104/48/18925.

I. N. Polonsky, D. M. O'Brien, J. B. Kumer, C. W. O'Dell, and the geoCARB Team. Performance of a geostationary mission, geoCARB, to measure CO_2, CH_4 and CO column-averaged concentrations. *Atmospheric Measurement Techniques*, 7(4):959–981, 2014. doi: 10.5194/amt-7-959-2014. URL https://www.atmos-meas-tech.net/7/959/2014/.

K. Raeder, J. L. Anderson, N. Collins, T. J. Hoar, J. E. Kay, P. H. Lauritzen, and R. Pincus. DART/CAM: An ensemble data assimilation system for CESM atmospheric models. *Journal of Climate*, 25(18):6304–6317, 2012. doi: 10.1175/JCLI-D-11-00395.1. URL https://doi.org/10.1175/JCLI-D-11-00395.1.

S. R. Saleska, S. D. Miller, D. M. Matross, M. L. Goulden, S. C. Wofsy, H. R. da Rocha, P. B. de Camargo, P. Crill, B. C. Daube, H. C. de Freitas, L. Hutyra, M. Keller, V. Kirchhoff, M. Menton, J. W. Munger, E. H. Pyle, A. H. Rice, and H. Silva. Carbon in Amazon forests: Unexpected seasonal fluxes and disturbance-induced losses. *Science*, 302(5650): 1554–1557, 2003. ISSN 0036-8075. doi: 10.1126/science.1091165. URL http://science.sciencemag.org/content/302/5650/1554.

F. M. Schwandner, M. R. Gunson, C. E. Miller, S. A. Carn, A. Eldering, T. Krings, K. R. Verhulst, D. S. Schimel, H. M. Nguyen, D. Crisp, C. W. O'Dell, G. B. Osterman, L. T. Iraci, and J. R. Podolske. Spaceborne detection of localized carbon dioxide sources. *Science*, 358(6360), 2017. ISSN 0036-8075. doi: 10.1126/science.aam5782. URL http://science.sciencemag.org/content/358/6360/eaam5782.

N. Semane, V.-H. Peuch, S. Pradier, G. Desroziers, L. El Amraoui, P. Brousseau, S. Massart, B. Chapnik, and A. Peuch. On the extraction of wind information from the assimilation of ozone profiles in Météo–France 4-D-Var operational NWP suite. *Atmospheric Chemistry and Physics*, 9(14):4855–4867, 2009. doi: 10.5194/acp-9-4855-2009. URL https://www.atmos-chem-phys.net/9/4855/2009/.

A. J. Simmons and A. Hollingsworth. Some aspects of the improvement in skill of numerical weather prediction. *Quarterly Journal of the Royal Meteorological Society*, 128(580):647–677, 2002. doi: 10.1256/003590002321042135. URL https://rmets.onlinelibrary.wiley.com/doi/abs/10.1256/003590002321042135.

B. B. Stephens, K. R. Gurney, P. P. Tans, C. Sweeney, W. Peters, L. Bruhwiler, P. Ciais, M. Ramonet, P. Bousquet, T. Nakazawa, S. Aoki, T. Machida, G. Inoue, N. Vinnichenko, J. Lloyd, A. Jordan, M. Heimann, O. Shibistova, R. L. Langenfelds, L. P. Steele, R. J. Francey, and A. S. Denning. Weak northern and strong tropical land carbon uptake from vertical profiles of atmospheric CO_2. *Science*, 316(5832):1732–1735, 2007. ISSN 0036-8075. doi: 10.1126/science.1137004. URL http://science.sciencemag.org/content/316/5832/1732.

T. Stocker, D. Qin, G.-K. Plattner, L. Alexander, S. Allen, N. Bindoff, F.-M. BreÌĄon, J. Church, U. Cubasch, S. Emori, P. Forster, P. Friedlingstein, N. Gillett, J. Gregory, D. Hartmann, E. Jansen, B. Kirtman, R. Knutti, K. KrishnaÂăKumar, P. Lemke, J. Marotzke, V. Masson-Delmotte, G. Meehl, I. Mokhov, S. Piao, V. Ramaswamy, D. Randall, M. Rhein, M. Rojas, C. Sabine, D. Shindell, L. Talley, D. Vaughan, and S.-P. Xie. *Climate Change 2013: The Physical Science Basis. Contribution of Working Group I to the Fifth Assessment Report of the Intergovernmental Panel on Climate Change*, book section Technical Summary, pages 33–115. Cambridge University Press, Cambridge, United Kingdom and New York, NY, USA, 2013. ISBN ISBN 978-1-107-66182-0. doi: 10.1017/CBO9781107415324.005. URL www.climatechange2013.org.

T. Takahashi, R. A. Feely, R. F. Weiss, R. H. Wanninkhof, D. W. Chipman, S. C. Sutherland, and T. T. Takahashi. Global air-sea flux of CO_2: An estimate based on measurements of sea–air pCO_2 difference. *Proceedings of the National Academy of Sciences*, 94(16):8292–8299, 1997. ISSN 0027-8424. doi: 10.1073/pnas.94.16.8292. URL https://www.pnas.org/content/94/16/8292.

T. Takahashi, S. C. Sutherland, C. Sweeney, A. Poisson, N. Metzl, B. Tilbrook, N. Bates, R. Wanninkhof, R. A. Feely, C. Sabine, J. Olafsson, and Y. Nojiri. Global sea–air CO_2 flux based on climatological surface ocean pCO_2, and seasonal biological and temperature effects. *Deep Sea Research Part II: Topical Studies in Oceanography*, 49(9):1601 – 1622, 2002. ISSN 0967-0645. doi: https://doi.org/10.1016/S0967-0645(02)00003-6. URL http://www.sciencedirect.com/science/article/pii/S0967064502000036. The Southern Ocean I: Climatic Changes in the Cycle of Carbon in the Southern Ocean.

P. P. Tans and T. Conway. Monthly atmospheric CO_2 mixing ratios from the NOAA CMDL Carbon Cycle Cooperative Global Air Sampling Network, 1968-2002, in Trends: A Compendium of Data on Global Change. Technical report, Carbon Dioxide Information Analysis Center, Oak Ridge National Laboratory, U.S. Department of Energy, Oak Ridge, Tenn., U.S.A, 2005. URL https://cdiac.ess-dive.lbl.gov/trends/co2/cmdl-flask/cmdl-flask.

P. P. Tans, I. Y. Fung, and T. Takahashi. Observational constraints on the global atmospheric CO_2 budget. *Science*, 247(4949):1431–1438, 1990. ISSN 0036-8075. doi: 10.1126/science.247.4949.1431. URL http://science.sciencemag.org/content/247/4949/1431.

M. Tomassini, G. Kelly, and R. Saunders. Use and impact of satellite atmospheric motion winds on ECMWF analyses and forecasts. *Monthly Weather Review*, 127(6):971–986, 1999. doi: 10.1175/1520-0493(1999)127<0971:UAIOSA>2.0.CO;2. URL https://doi.org/10.1175/1520-0493(1999)127<0971:UAIOSA>2.0.CO;2.

K. E. Trenberth and J. T. Fasullo. Regional energy and water cycles: Transports from ocean to land. *Journal of Climate*, 26(20):7837–7851, 2013. doi: 10.1175/JCLI-D-13-00008.1. URL https://doi.org/10.1175/JCLI-D-13-00008.1.

I. R. van der Velde, J. B. Miller, M. K. van der Molen, P. P. Tans, B. H. Vaughn, J. W. C. White, K. Schaefer, and W. Peters. The CarbonTracker data assimilation system for CO_2 and δ^{13}c (CTDAS-C13 v1.0): retrieving information on land–atmosphere exchange processes. *Geoscientific Model Development*, 11(1):283–304, 2018. doi: 10.5194/gmd-11-283-2018. URL https://www.geosci-model-dev.net/11/283/2018/.

D. W. Waugh, T. M. Hall, W. J. Randel, P. J. Rasch, B. A. Boville, K. A. Boering, S. C. Wofsy, B. C. Daube, J. W. Elkins, D. W. Fahey, G. S. Dutton, C. M. Volk, and P. F. Vohralik. Three-dimensional simulations of long-lived tracers using winds from MACCM2. *Journal of Geophysical Research: Atmospheres*, 102(D17):21493–21513, 1997. doi: 10.1029/97JD00793. URL https://agupubs.onlinelibrary.wiley.com/doi/abs/10.1029/97JD00793.

S. C. Wofsy. HIAPER Pole-to-Pole Observations (HIPPO): fine-grained, global-scale measurements of climatically important atmospheric gases and aerosols. *Philosophical Transactions of the Royal Society of London A: Mathematical, Physical and Engineering Sciences*, 369(1943):2073–2086, 2011. ISSN 1364-503X. doi: 10.1098/rsta.2010.0313. URL http://rsta.royalsocietypublishing.org/content/369/1943/2073.

D. Wunch, G. C. Toon, J.-F. L. Blavier, R. A. Washenfelder, J. Notholt, B. J. Connor, D. W. T. Griffith, V. Sherlock, and P. O. Wennberg. The Total Carbon Column Observing Network. *Philosophical Transactions of the Royal Society of London A: Mathematical, Physical and Engineering Sciences*, 369(1943):2087–2112, 2011. ISSN 1364-503X. doi: 10.1098/rsta.2010.0240. URL http://rsta.royalsocietypublishing.org/content/369/1943/2087.